Sequence grammar and dynamics of subcellular translation revealed by APEX-Ribo-Seq

Kotaro Tomuro[1,2], Takanori Akaiwa[3], Akane Harada[4,5], Kenta Kobayashi[5,6], Nobuyuki Shiina[3,4,5], Kyogo Kawaguchi[7,8,9*], Yuichi Shichino[1*], and Shintaro Iwasaki[1,2,*]

[1]RNA Systems Biochemistry Laboratory, Pioneering Research Institute, RIKEN, Wako, Saitama 351-0198, Japan

[2]Department of Computational Biology and Medical Sciences, Graduate School of Frontier Sciences, The University of Tokyo, Kashiwa, Chiba 277-8561, Japan

[3]Exploratory Research Center on Life and Living Systems (ExCELLS), National Institutes of Natural Sciences, Okazaki, Aichi 444-8787, Japan

[4]Laboratory of Neuronal Cell Biology, National Institute for Basic Biology, Okazaki, Aichi 444-8787, Japan

[5]Basic Biology Program, The Graduate University for Advanced Studies (SOKENDAI), Okazaki, Aichi 444-8787, Japan

[6]Section of Viral Vector Development, National Institute for Physiological Sciences, Okazaki, 444-8585, Japan

[7]Nonequilibrium Physics of Living Matter Laboratory, Pioneering Research Institute, RIKEN, Kobe, Hyogo 650-0047, Japan

[8]Institute for Physics of Intelligence, Department of Physics, The University of Tokyo, Bunkyo-ku, Tokyo 113-0033, Japan

[9]Universal Biology Institute, The University of Tokyo, Bunkyo-ku, Tokyo 113-0033, Japan

[*]Correspondence: kyogo.kawaguchi@riken.jp (K. Kawaguchi), yuichi.shichino@riken.jp (Y.S.), and shintaro.iwasaki@riken.jp (S.I.)

Abstract

Local translation at specific subcellular regions is proposed to define appropriate protein destinations and functions. However, our understanding of local translation is still far from complete, due to a lack of versatile analysis tools. Here, we developed a new method, termed "APEX-Ribo-Seq", that integrates ribosome profiling (Ribo-Seq) with APEX2-based proximity labeling. We mapped local translation at 14 distinct organelles and identified over 3000 genes that are locally translated. Interpretable machine learning methods based on RNA language models systematically uncovered RNA-binding proteins with key roles in compartment-specific translation. In addition, we revealed slow translation kinetics associated with cotranslational membrane insertion of nascent chains. APEX-Ribo-Seq also captured cell cycle-regulated dynamics at the centrosome and stress-regulated programs at stress granules and autophagosomes. We also demonstrated the utility of APEX-Ribo-Seq in primary neurons, revealing compartment-specific translatomes in dendrites, axons, and presynapses. Our results provide a comprehensive view of the spatiotemporal translatome and its regulation.

Introduction

Spatiotemporal regulation of protein synthesis is a phenomenon that is broadly conserved from bacteria to humans, allowing fine-tuning of gene expression and cellular functions [1,2]. Local translation offers significant advantages for maintaining proteome integrity within cells that are densely packed with structurally distinct organelles. For example, spatially restricted protein synthesis supports protein maturation via cotranslational translocation into the endoplasmic reticulum (ER) [3,4] and *in situ* assembly of protein complexes, as observed for the nuclear pore complex [5]. Spatial restriction of protein synthesis also ensures high concentrations of specific proteins in discrete subcellular compartments, such as the local of synthesis actin at the leading edge of migrating cells [6] and axial patterning proteins during early embryonic development [7–10]. Moreover, local protein synthesis is highly advantageous in polarized cells such as neurons; these cells transport specific mRNAs to dendrites and axons and translate them locally, regulating activity-dependent synaptic plasticity, axon guidance, and memory formation [11,12].

Recent studies have suggested that local translation is more widespread than previously appreciated. In addition to the ER [3,4] and mitochondria [13], a variety of membranous organelles have been reported to exhibit local translation, such as endosomes/lysosomes [14–18], the Golgi apparatus [19], nuclear pore complexes [5,20], and peroxisomes [21]. Cytoskeleton-associated structures such as centrosomes [19,22–26], spindles [24,27,28], cilia [29–31], midbodies [32,33], and cell protrusions [34–37] also serve as sites of translation. Furthermore, increasing evidence suggests active translation within ribonucleoprotein (RNP) granules, which are biomolecular condensates composed of RNAs and proteins [10,38–44]. These findings imply that translation may occur in subcellular regions beyond

those currently characterized; however, the global landscape of local translation remains unclear.

Local translation has traditionally been inferred from the subcellular localization of mRNAs; however, the presence of mRNAs is not always coupled with active translation [34,35,45], highlighting the necessity for direct observations of translation. Imaging-based approaches such as nascent chain tracking in living cells [46–49] offer high spatial resolution but suffer from limited scalability and throughput. More recently, RIBOmap has enabled the visualization of thousands of ribosome-bound mRNAs via DNA amplicons and *in situ* sequencing [50]; however, this approach requires predefined target genes for probe design.

In contrast, deep sequencing-based approaches offer higher throughput and less biased analysis. Ribosome profiling (Ribo-Seq), a comprehensive method for measuring cellular translation through RNase footprinting of ribosome-protected mRNAs [51], can be used to investigate local translation if combined with microdissection [52–54] or biochemical fractionation [55,56]. However, purifying specific compartments without cross-contamination remains challenging. As an alternative, proximity-labeling of localized ribosomes using the biotin ligase BirA tethered to subcellular membranes and its biotin acceptor peptide (AviTag) fused to the ribosome protein has enabled more spatially restricted Ribo-Seq for the endoplasmic reticulum membrane (ERM) [57–59], outer mitochondrial membrane (OMM) [60], and peroxisomes [21]. However, this strategy requires laborious optimization, including biotin depletion from culture media and ribosomal protein tagging. While the use of light-controllable split-BirA [61] or the promiscuous biotin ligase TurboID [62] has addressed some of these limitations, these methods still detect only ribosome-bound mRNAs and thus cannot accurately differentiate translation activity

from RNA recruitment. Therefore, a more versatile and unbiased methodology for the genome-wide measurement of local translation has long been awaited.

Here, we present APEX-Ribo-Seq, a newly developed method that integrates APEX2-based proximity labeling, which targets both proteins and RNAs and is widely used in spatial proteomics and transcriptomics [63–70], with ultralow-input Ribo-Seq [71]. This setup enables robust, genome-wide measurement of local translation at high spatial resolution. Importantly, simultaneous APEX-RNA-Seq [63,64] allowed us to dissect the effect of RNA localization and onsite translational control. To demonstrate the versatility of APEX-Ribo-Seq, we applied our technique across 14 distinct subcellular compartments—the ERM, OMM, peroxisome, *cis*-Golgi, *trans*-Golgi, lysosome, endosome, early endosome, centrosome, plasma membrane, cell junction, intermediate filaments, nuclear pore, and clathrin-coated vesicles—and established a comprehensive subcellular translation atlas in human cells. Integration with machine learning and RNA language models revealed the sequence grammar underlying compartment-specific translation and identified key regulatory features mediated by RNA-binding proteins. Comparisons with calibrated Ribo-Seq [72] further revealed the spatial control of translation kinetics, highlighting distinct elongation and initiation profiles at the ERM and OMM. Not only the steady state, APEX-Ribo-Seq also captured the dynamic modulation by internal and external stimuli, during the cell cycle and at stress-induced organelles (stress granules and autophagosomes). Finally, beyond the regular human tissue culture, we extended our analysis to mouse primary neurons for compartment-specific translatomes in dendrites, axons, and presynapses. Importantly, this investigation revealed local protein synthesis at subcellular sites that had not previously been anticipated as sites of protein synthesis (*e.g.*, the plasma membrane, cell junction, intermediate filaments,

clathrin-coated vesicles, and autophagosomes). Together, these findings highlight APEX-Ribo-Seq as a powerful and versatile platform for investigating spatiotemporal translation regulation in diverse biological contexts.

Results and Discussion

APEX2-mediated proximity labeling of ribosome–mRNA complexes

To develop a versatile method to survey local translation, we sought to combine APEX2-based proximity labeling with ribosome profiling. In the presence of H_2O_2, the APEX2 protein—an engineered peroxidase [66]—generates short-lived radicals from phenol and covalently conjugates phenol to nearby RNAs and proteins [63,64,66,73,74]. Thus, the fusion of biotin to phenol provides a tag for subsequent purification using streptavidin beads. Given that APEX2 tagging of organelle markers allows a survey of the local proteome [65,68,73,75,76] and transcriptome [63,64,74], we reasoned that this technique could be used to label local ribosome–mRNA complexes for subsequent Ribo-Seq experiments (Figure 1A).

Here, we optimized the method, termed APEX-Ribo-Seq, as a versatile tool to survey local translation. Although the biotin–streptavidin interaction is strong, contaminating proteins and RNAs that remain after purification via streptavidin beads may hamper specificity. To overcome this issue, we substituted the conventional biotin-phenol with desthiobiotin-phenol, which can be utilized with APEX2 [77–79]. Desthiobiotin has weaker, reversible binding to streptavidin (K_a = 10^{12} M^{-1}), allowing competitive elution from the beads with the higher affinity biotin (K_a = 10^{15} M^{-1}) [80], reducing nonspecific contamination during purification (Figure 1A).

To evaluate the labeling and purification performance of this approach, we established HEK293 T-REx cells stably expressing a nuclear export signal (NES) tagged with APEX2 (APEX2-NES-EGFP) (Figure S1A); this protein should be uniformly diffused in the cytosol. As expected, colocalization of the protein (detected via enhanced green fluorescent protein [EGFP]) and desthiobiotinylated molecules was observed throughout the cytosol (Figure S1B). Desthiobiotinylated RNAs and proteins blotted on

membranes were monitored in a desthiobiotin phenol- and H_2O_2-dependent manner, with detection via fluorophore-conjugated streptavidin (Figure S1C). The cosedimentation of desthiobiotinylated RNAs and proteins with polysomes in a sucrose density gradient suggested the successful labeling of ribosomal complexes by the APEX2 system (Figure S1D-E). These ribosome–mRNA complexes were tethered to streptavidin beads, washed, and competitively eluted with free biotin (Figure 1A). However, this purification approach exhibited the drawback of low material recovery. To overcome this issue, we harnessed a Ribo-Seq derivative tailored for low input, termed T7 High-resolution Original RNA (Thor)-Ribo-Seq [71].

One of the general concerns associated with the APEX2-based method is the use of H_2O_2, which induces oxidative stress. Therefore, here, we used a short treatment (1 min) with subsequent quick quenching; critically, stress-response induction at the translational level was not detected under these experimental conditions (Figure S1F).

We subsequently conducted cytosolic APEX-Ribo-Seq with APEX2-NES-EGFP for further optimization. Earlier APEX2-based techniques employed a high salt wash (1 M NaCl) to reduce contamination [63,64]. However, under our conditions, a high salt concentration (Figure S1G) did not improve the data quality; rather, we found that the yield of ribosome footprints mapped to open reading frames (ORFs) (Figure S1H) was reduced relative to that obtained using the standard medium salt concentration for regular Ribo-Seq (150 mM NaCl) [81,82]. Additionally, the mild salt condition resulted in a typical footprint length distribution (Figure S1I), marked 3-nt periodicity (Figure S1J-K), high reproducibility (Figure S1L), and high correspondence to the input standard Ribo-Seq (Figure 1B), indicating uniform recovery of cytosolic ribosomes. Thus, we used the medium salt concentration wash for the pulldown.

Given that mitochondrial ribosomes (mitoribosomes) in the matrix constitute a separate translation system, distinct from cytosolic ribosomes, the NES-fused APEX2 enzyme in the cytosol should not have access to mitoribosomes. Consistent with this expectation, mitoribosome footprints corresponding to all 13 ORFs encoded in the mitochondrial genome [83,84] were depleted in cytosol APEX-Ribo-Seq (Figure 1B).

We subsequently conducted reciprocal experiments to capture mitochondrial translation in the matrix by using APEX2 fused to the mitochondrial targeting signal (MTS) (Figure S1A). As expected, the localization of MTS-APEX2 and the desthiobiotinylation reaction were restricted to the mitochondria (Figure S1M). Moreover, matrix APEX-Ribo-Seq exploiting MTS-APEX2 was enriched in mitoribosome footprints (Figure 1C). The 3-nt periodicity confirmed the recovery of mitoribosome footprints [85–87] (Figure S1N), indicating explicit targeting of mitochondrial translation by the APEX-Ribo-Seq matrix.

Thus, we employed these refined procedures for the downstream analyses.

Benchmarking APEX-Ribo-Seq

To evaluate the performance of our approach for on-organelle translation, we focused on the ER membrane (ERM), which is a well-characterized site of local translation [3,57,63,65,88,89]. We used APEX2 as a C-terminal tag for CYP2C1 TM domain, which faces the cytosolic side of the ER [63–65,90] (Figure S1A); as expected, the tagged protein expression and desthiobiotinylation were localized to the ER (Figure S2A). ERM APEX-Ribo-Seq maintained the hallmarks of ribosome footprints, including read length distribution and strong 3-nt periodicity (Figure S2B-D).

Relative to the membrane-enclosed ER lumen or mitochondrial matrix, the cytosolic surfaces of organelles present intrinsic challenges for proximity labeling; the highly open and dynamic configuration may hinder efficient tagging by limited biotin/desthiobiotin diffusion within a short timeframe (1 min in our conditions), resulting in a relatively high background [63,65]. Thus, we calculated "fold enrichment" for these sites carefully, considering 1) the input and 2) the cytosolic translation indicated by the same APEX approach (Figure S2E). For the significantly enriched subgroups (Figure 1D), we further considered BirA–Avi tag-mediated proximity-specific ribosome profiling data [57] as a reference and defined another fold enrichment threshold through receiver operating characteristic (ROC) analysis [91] (Figure S2F). Ultimately, we designated 979 genes that were locally translated on the ERM (Figure 1D and Table S1). This set of genes showed high correspondence with the secretome (see Methods for details), as well as with the set of genes identified by ERM-targeted Frac-Seq [89], APEX-RIP [65], and APEX-RNA-Seq [63] (Figure S2G). Among the mRNAs identified as translated on the ERM (Table S1), *XRP1* and *CAST* were confirmed via single-molecule inexpensive fluorescent *in situ* hybridization (smiFISH) to localize to the ERM [92] (Figure S2H-I).

We subsequently focused on the translation on the outer mitochondrial membrane (OMM), another organelle associated with cotranslational membrane insertion. For this purpose, we fused APEX2 to the mitochondrial antiviral signaling (MAVS) C-terminal transmembrane (TM) domain, which anchors to the OMM [93,94] (Figure S1A); the N-terminal tag (APEX2-MAVS TM) faces the cytosolic side [63]. The protein localization and desthiobiotinylation of the OMM were confirmed by immunostaining (Figure S2J). OMM APEX-Ribo-Seq recovered 3-nt periodic ribosome footprints (Figure S2K-L). Through enrichment analysis (Figure S2E) and threshold determination by ROC in ERM

(Figure S2F), we identified 992 genes as OMM locally translated mRNAs (Figure 1E and Table S1); this set of genes aligned with the gene list produced by earlier APEX-RNA-Seq experiments [63] (Figure S2M). We observed that approximately 40% of the mitochondria-targeted proteins annotated in MitoCarta 3.0 [95] were synthesized on the OMM (Figure 1F), which is consistent with the results of studies using Transit-ID [96] and APEX-RNA-Seq [63]. We also noted that the local translation on the OMM was biased toward mRNAs with short ORFs (Figure 1G). The most notable examples of mRNAs locally translated on the OMM were those encoding mitoribosome subunits (Figure 1E), as was also reported in the Transit-ID study [96].

A comparison of the translation survey in the matrix and on the OMM further ensured the specificity of APEX-Ribo-Seq. OMM APEX-Ribo-Seq did not capture 13 ORFs encoded in the mitochondrial genome; conversely, matrix APEX-Ribo-Seq did not capture mRNAs locally translated on the OMM (Figure S2N). These data confirmed the exclusive detection of protein synthesis inside and outside mitochondria via the APEX-Ribo-Seq technique.

Overall, these benchmark analyses demonstrate the versatility and robustness of APEX-Ribo-Seq for probing subcellular translation across cellular compartments.

Local translation atlas across 14 distinct subcellular compartments

The superior performance of APEX-Ribo-Seq led us to expand our survey to a wider variety of subcellular loci. We fused the APEX2 tag to well-defined bait proteins [97] (Figure S1A) to conduct proximity labeling at 12 loci—the peroxisome, *trans*-Golgi, *cis*-Golgi, lysosome, endosome, early endosome, clathrin-coated vesicle, plasma membrane, cell junction, nuclear pore, intermediate filament, and centrosome (Figures S1A and S3A).

We carefully selected the bait protein species and their expression levels. In particular, we generated cells with genomic knock-in of the centrosome marker CEP192 (Figure S1A), since the additional copies of other markers in stable integrants caused abnormal centrosome duplication or aggregation (Figure S3B). Again, we detected a typical footprint length with a 3-nt phase in APEX-Ribo-Seq, targeting specific loci with high reproducibility (Figure S3C-D). Overall, considering these sites along with the NES, matrix, ERM, and OMM, APEX-Ribo-Seq showed high reproducibility (Figure S3E). As for the ERM and OMM, we defined the locally translated mRNAs for each organelle; the numbers of such mRNAs ranged from 174 to 1159 at different sites (Figure S3F). Among the 14 loci (12 loci above, ERM, and OMM), mRNAs from 3,227 genes were locally translated at at least one site (Figure S3G).

Our data closely corresponded with the known localizations of mRNAs identified via smFISH; for example, the nuclear pore localization of *CLIP1*, *DDX11*, and *ADAM10* mRNAs and the *cis*-Golgi localization of *AKAP9* mRNA [19] were validated in our local translation profiles (Figure S3F).

To provide further confidence in our datasets, we performed smiFISH [92] for mRNAs found via APEX-Ribo-Seq at the peroxisome, *trans*-Golgi, *cis*-Golgi, plasma membrane, and intermediate filament (Figure S3H-Q). In addition, local translation on the centrosome was validated by treatment with centrinone, a Polo-like kinase 4 (Plk4) inhibitor [98] that eliminates the centrosome as Plk4 is required for the initiation of centriole assembly. The translation efficiency of mRNAs locally translated on the centrosome, as measured by standard Ribo-Seq and RNA-Seq, decreased upon centrinone treatment (Figure S3R).

To obtain an overview of the local translation on organelles, we conducted dimension reduction by t-distributed stochastic neighbor embedding (t-SNE) clustering [99] (Figure 2A). While the patterns of local translation at each subcellular compartment were separated overall, some of them were closer to each other than others (Figure 2A). These clusters included ERM and OMM, which have close physical contacts [100]; the plasma membrane, endosome, and lysosome, which are connected to each other through membrane trafficking [101,102]; early endosomes and clathrin-coated vesicles, which likewise are connected via trafficking [103]; the *trans*-Golgi network (TGN) and clathrin-coated vesicles that bud from the TGN [104]; and the *cis*-Golgi and centrosome, which are in close spatial proximity in cells [105] (Figure 2A). Despite the similarities among some organelles, 64% of the listed transcripts were locally translated at only one or two loci (Figure 2B), suggesting the specificity of local translation. We found that 1105 mRNAs (34%) were uniquely translated at a single locus (Figure 2C).

Local translation of the local proteome

Our local translation atlas showed a close connection between the site of translation and the localization of the synthesized proteins. We employed the protein subcellular localization datasets generated by BioID-based proximity labeling [97] (Figure 2D) and immunostaining (The Human Protein Atlas) [106] (Figure S4A). The correspondence between local translation and protein localization was found in the ERM (Figures 2D and S4A), OMM (Figures 2D and S4A), endosomes (Figure 2D), lysosomes (Figure 2D), plasma membrane (Figures 2D and S4A), cell junctions (Figures 2D and S4A), *trans*-Golgi (Figure 2D), *cis*-Golgi (Figure S4A), peroxisomes (Figure S4A), intermediate filaments (Figure S4A), and centrosomes (Figure S4A).

Detailed inspection of locally translated mRNAs revealed that key factors for organelle function were supplied locally. Functional enrichment analysis based on complex formation via Search Tool for the Retrieval of Interacting Genes/Proteins (STRING) [107] revealed that this trend was global (Figure S4B). Some membrane-embedded assemblies included the Sec61 complex [108], translocon-associated protein (TRAP) complex [109], signal peptidase complex [110,111], and oligosaccharyltransferase (OST) complex [112,113] for the ERM and the translocase of the outer membrane (TOM) complex [114] for the OMM (Figure 2E), reflecting the cotranslational membrane insertion of nascent peptides in these organelles.

In addition, APEX-Ribo-Seq revealed the onsite assembly of complexes peripherally associated with organelles. While the ERM and OMM are linked to the translation of mRNAs encoding membrane-inserted or translocated proteins, few examples of this phenomenon have previously been reported for other organelles. Indeed, the detection of mRNAs encoding membrane was limited for peroxisomes, endosomes, and cell junctions, and for the centrosome, which is membraneless (Figure 2F). These findings suggested that remaining proteins locally synthesized consist of auxiliary organelle-associated factors. Indeed, we found the following examples: the nuclear pore, outer ring Nup107-160 subcomplex [115] and SEPTIN complex, which is a diffusion barrier of the nuclear pore [116]; the clathrin-coated vesicle, COPI coat complex [117], HOPS tethering complex [118], and AP2 adaptor complex [119]; the lysosome, retromer [120] and V_1 domain of vacuolar-type (v)-ATPase [121]; the plasma membrane, G protein [122] and Spectrin [123]; and the *trans*-Golgi, GARP complex [124] and TRAPP complex [125] (Figure 2G). We also found that cytosolic complexes including prefoldin (PFDN) [126] and signal recognition particle (SRP) [127] were locally synthesized on the ERM (Figure S4C).

Given that protein complexes can be formed through the interaction of two nascent chains emerging from two ribosomes (so-called co-co–assembly) [128,129], we reasoned that on-organelle translation may serve as a unified platform that simultaneously facilitates both cotranslational complex assembly and localization. We examined the candidate co-co–assembly pairs in a structure-based cotranslational assembly prediction dataset [129] and cross-referenced them with our local translation atlas (Figure S4D). This analysis identified 204 protein pairs that co-co–assembled locally, among which 103 pairs were cotranslated at only a single locus (Figure S4D). Consistent with our observation of local supply on clathrin-coated vesicles (Figure 2G), the HOPS complex subunits VSP16 and VPS33A were co-co–assembled at this site (Figure S4D). At the OMM, we also found potential co-co–assembly of the alpha and beta subunits of several nascent polypeptide-associated complex (NAC) chaperones (NACA–BTF3, NACA–BTF3L4, NACA2–BTF3, and NACA2–BTF3L4), which are required for the targeting of polytopic proteins to the OMM [130] (Figure S4D).

Localization of mRNAs and onsite translational regulation

Then, we investigated the general rules that allow efficient local translation. The mechanisms could include the following: 1) nascent chain-mediated recruitment (such as signal peptide recognition by the SRP for on-ERM translation), 2) mRNA recruitment, 3) the onsite control of translation efficiency, or 4) a combination of these mechanisms (Figure S5A). Mechanisms 1) and 2) must align with mRNA localization on the organelles. To quantify the role of RNA localization in local translation, we conducted APEX-RNA-Seq in parallel using the same samples used for APEX-Ribo-Seq (Figures 1A and S5B) and calculated the enrichment using the same method that was applied for

APEX-Ribo-Seq (Figure S2E). We observed a diverse range of correlations between the APEX-Ribo-Seq and APEX-RNA-Seq results across subcellular compartments (Figure 3A-B). We detected high correspondence at the centrosome, ERM, and OMM. The centrosome is known to recruit mRNA–ribosome complexes through emerging nascent chains [19,22,25], whereas the ERM and OMM feature the cotranslational membrane insertion of nascent chains [57,60,96,131–133]. In contrast, translation efficiency control was observed to make a greater contribution at intermediate filaments, endosomes, lysosomes, the plasma membrane, and early endosomes (Figure 3A-B).

We note that ribosome occupancy (APEX-Ribo-Seq enrichment over APEX-RNA-Seq enrichment, Figure S5C) is low in the mitochondrial matrix (or mitoribosome-mediated translation), which is consistent with the previously observed extremely slow translation kinetics [87,134].

RNA-binding proteins and local translation

Given the substantial contribution of onsite translation control, we reasoned that RNA-binding proteins (RBPs) might affect subcellular mRNA translation (Figure S5A). Indeed, recent studies highlighted the importance of RBPs in local traslation even for the loci where nascent chains have been thought to play a key role [135]. To explore RBP binding profiles across the transcriptome, we harnessed the collection of enhanced crosslinking and immunoprecipitation followed by sequencing (eCLIP-Seq) datasets covering 250 conditions for 168 RBPs in two cell lines (K562 and HepG2) [136]. eCLIP-Seq reads on 5′ untranslated regions (UTRs), ORFs, and 3′ UTRs were evaluated separately. We found that some RBPs exhibited high loading on mRNAs locally translated on specific organelles (Figure 3C). Our findings aligned with those of prior studies, such as

TIA1/TIA1L binding to the 3′ UTRs of mRNAs translated on the ERM [137] and LARP4 localization to the OMM (see below for further analysis) [138–140]. Additionally, PUM1 binding to mRNAs locally translated on the peroxisome aligns well with reports that Puf5, a PUM1 homolog, recruits mRNAs that encode peroxisome proteins to the peroxisome [141].

Prediction of local translation via language models

A straightforward mechanism of localized translation is that mRNAs carry short RNA motifs that can be recognized by RBPs already present at specific sites. We analyzed mRNA sequences for such motifs using HOMER (see Methods for details; Figure 4A and Table S2) and found many motifs that were indeed enriched in the sequences with high organelle enrichment. However, the short motifs occurring in the mRNAs were diverse across the subcellular compartments; for example, many motif hits were found for mRNAs translated on the intermediate filaments, nuclear pore, centrosome, *cis*-Golgi, clathrin-coated vesicle, and *trans*-Golgi, whereas the mRNAs translated at the other organelles possessed few or no enriched motifs (Figure 4A). To assess whether RNA sequence features beyond short motifs determine organelle-specific protein synthesis, we developed models to predict local translation levels from sequence information. First, we tested the predictive power of RNA length alone, since we observed clear differences in 5′ UTR, ORF, and 3′ UTR lengths across locally translated mRNAs (Figure S6A). Simple linear regression and random forest models using only sequence length effectively predicted the $\log_2$ organelle enrichment in APEX-Ribo-Seq (Figures 4B and S6B). Notably, these length-based models achieved high predictive accuracy on test sets for ERM and OMM, where distinct short sequence motifs were not detected in

the above analysis (Figure 4A). This finding indicates that shorter RNA length, and particularly shorter ORF length (Figure S6A), is a predictor of localization to the ERM and OMM.

We next employed machine learning approaches using the full nucleotide sequence to explore more complex sequence determinants. For this purpose, a key advantage of nucleotide language models [142] is their ability to embed sequences of different lengths into a fixed-size numerical vector that can capture the most salient information on the basis of the context learned during extensive pre-training on large-scale sequence data. We first attempted translation location prediction from embeddings generated by the largest available RNA language models, AIDO.RNA [143] and RiNALMo [144], as well as the DNA model Evo 2 [145]. We found that in all three cases (Figure S6C), even simple mean pooling of embeddings derived from the full sequences, coupled with a standard feedforward network, yielded superior predictive performance than a baseline convolutional neural network (Figure 4B). Interestingly, mean-pooled embeddings derived solely from the ORFs consistently outperformed mean-pooled embeddings of the full sequence (Figure 4B), suggesting that information from a partial sequence is not trivially subsumed by whole-sequence embedding. Local translation not associated with short motifs (at the ERM and OMM), RNA length (at intermediate filaments), or both (at lysosomes, cell junctions, the plasma membrane, endosomes, and early endosomes) could still be predicted reasonably well through this approach (Figure 4B), indicating that the language-model embeddings capture information beyond simple motif count and sequence length.

To pinpoint the contributions of RNA regions more specifically, we developed a regression model incorporating an interpretable attention mechanism (termed

TransLocAttn; see Methods for details). This model was trained using concatenated RiNALMo embeddings from the 5′ UTR, ORF, and 3′ UTR sequences (Figure S6D). The model achieved strong predictive accuracy for local translation across the 14 compartments on a held-out test set (Figure 4B). Critically, analysis of the learned attention weights, which reflect the nucleotide-level importance for local translation prediction, revealed distinct, nonuniform patterns along the sequence (Figures 4C-E and S6E-F, top). These attention profiles were highly dependent on the mRNAs and the target compartment, indicating that the model identifies different sequence regions as critical for localization depending on the destination (Figure 4C-E and S6E-F, top).

The presence of attention profile signals in ORF regions of the RNA could be explained either by nascent chain-mediated recruitment or by RBP binding. To test the latter possibility, we investigated whether the regions highlighted by the attention mechanism corresponded to known protein–RNA interactions. We systematically compared the attention profiles against RBP binding profiles experimentally determined by eCLIP-Seq [136]. We aligned the smoothed attention tracks and eCLIP read distributions and assessed their correspondence using the tail dependence score, which quantifies the co-occurrence of high-signal peaks (see Methods for details), as well as Spearman's correlation (Figure S6G-I). These analyses revealed that the RBP binding profiles were significantly correlated with attention weights (Figures 4C-E and S6E-I, bottom and Table S2), indicating that RBP binding may be the mechanism of local translation. Examples include IGF2BP1 binding to *RNF2* mRNA, locally translated on the ERM (Figure 4C) and RBM15 and TRA2A binding to *JARID2* mRNA, locally translated at the centrosome (Figure S6E). Interestingly, multiple RBPs seem to target the same regions with high attention (Figures 4D-E and S6E-F). These findings indicate that the attention

weights, guided solely by the localization prediction task, can pinpoint sequence regions coinciding with established RBP interaction sites, suggesting that the model implicitly learns biologically meaningful regulatory features.

To test the effects of RNA-binding proteins on local translation, we focused on LARP4, since this protein was suggested to function in OMM translation in multiple independent analyses; namely, eCLIP-Seq showed a global high correlation between LARP4 and mRNAs translated on the OMM (Figure 3C), and the sequence of *MRPL52* mRNA, which encodes a subunit of the mitochondrial ribosome and provides a notable example of OMM translation (Figure 1E), showed attention weights associated with the LARP4 eCLIP-Seq profile (Figure 4E). We also tested the involvement of AKAP1 in OMM translation since this protein also presented eCLIP-Seq reads on mRNAs translated on the OMM (Figure S6J). Moreover, earlier studies have also suggested that LARP4 and AKAP1 may mediate OMM translation [138,140]. Indeed, standard Ribo-Seq revealed reduced translation of mRNAs encoding mitoribosome subunits upon the knockdown of *LARP4* and *AKAP1* (Figure 4F-G).

As further validation, we tested IGF2BP1 for a role in ERM translation, as this RBP showed high loading across mRNAs locally translated on the ERM (Figure 3C) and a correspondence between the attention profile and the eCLIP-Seq read distribution on *RNF2* mRNA (Figure 4C). We detected decreased protein synthesis from ERM-translated mRNAs upon *IGF2BP1* knockdown (Figure 4H).

These results indicate that RBP-guided mechanisms can explain the specificity of local translation.

Kinetics of local translation associated with membrane insertion of the nascent chain

Recent reporter-based single molecule analysis in cells [146] suggested that translation kinetics and ribosome stoicheomtery may differ at subcellular loci. This led us to characterize local protein synthesis by examining ribosome stoichiometry on mRNAs and translational kinetics. Calibrated ribosome numbers on ORFs measured by a Ribo-Calibration technique [72] revealed differential numbers of ribosomes among ORFs (Figure S6A). Considering the variations in ORF length among mRNAs in each local translation category (Figure S6A), the ribosome density per 100 codons was calculated (Figure 5A). We found that mRNAs locally translated on the ERM and OMM presented particularly high ribosome density (Figure 5A).

The high degree of ribosome presence on ORFs could be explained by either 1) a slow elongation rate or 2) a fast initiation rate. Therefore, to assess the translation elongation rate, we reanalyzed published data from a ribosome run-off assay with harringtonine chase that had been performed in the same cell line [72]. The regression line with chase time and extended ribosome-free region downstream of the start codon reflected the elongation rates [147]. Compared with the global elongation rate (3.32 codon/s for the genes detected in this study), ribosomes on mRNAs located at the ERM and OMM traversed at a 1.5-fold slower rate (2.87 codon/s on the ERM and 2.37 codon/s on the OMM) (Figure 5B-C). This difference in kinetics may be associated with the cotranslational membrane insertion in these organelles [57,60,96,131–133].

Leveraging the calibrated ribosome numbers on ORFs (Figure 5A) and elongation rates (Figure 5B-C), we estimated translation initiation rates for ERM- and OMM-translated mRNAs as described in our previous report [72]. We found slower initiation rates for on-ERM and on-OMM translation (28 s/event for ERM and 33 s/event for OMM vs. 24 s/event for global mRNAs, on average) (Figure 5D). Recent studies suggest that

translation initiation is limited by feedback from slow elongation [148,149], raising the possibility that similar regulatory mechanisms coordinate these two rates on the organelles associated with cotranslational membrane insertion of nascent chains. Suboptimal codon use in these ORFs may also facilitate such an adjustment mechanism (Figure 5E).

The subunits of the OXPHOS complex in mitochondria are served by both cytosolic and mitochondrial translation systems [84] in a coordinated manner [86,150]. Considering the slow kinetics of mitochondrial translation [87,134], a balanced rate of protein synthesis from the OMM may be beneficial for OXPHOS complex formation.

Cell cycle phase-specific translation at centrosomes

The advantage of APEX-Ribo-Seq is short labeling time (1 min) to trap local translation staus. Given that, we reasoned that our approach could track the temporal change of localized protein synthesis on organelles. As a showcase, we focused on local translation on centrosomes during the cell cycle. The recruitment and local translation of specific mRNAs on centrosomes have been documented in association with the maturation and duplication of centrosomes throughout the cell cycle [22,151]. Encouraged by these studies, we synchronized the cell cycle phase with the CDK1 inhibitor RO3306 [152] to obtain G1-, G2-, and M-phase cells (Figure S7A-C) and then conducted centrosome APEX-Ribo-Seq (Figure S7D-F and Table S3). To calculate the cell cycle phase-dependent enrichment of specific factors at the centrosomes, we considered Ribo-Seq data from asynchronous cells as the baseline (Figure S7G). We identified 1074 genes with phase-dependent translation profiles (Figures 6A and S7H). Even though these genes were selected according to their overrepresentation relative to the asynchronous state, phase-dependently translated

mRNAs were enriched in the asynchronous centrosome APEX-Ribo-Seq (Figure S7I). Importantly, the majority of these genes underwent local translation at the centrosome at one specific phase (Figure 6B). Our data aligned well with phase-dependent recruitment of centrosomal mRNAs previously studied by smFISH [22]; early metaphase mRNAs such as *NIN*, *PCNT*, *CEP350*, and *BICD2* mRNAs were translated during the G2 and M phases, whereas the interphase mRNA *CCDC88C* was translated during the G1 phase (Figure 6C). In addition to known mRNAs, we also found mRNAs encoding tubulin subunits as highly enriched throughout the cell cycle phases, as the centrosome served as a microtubule organizing center (Figure S7J). Simultaneous APEX-RNA-Seq (Figure S7K) revealed a moderate correlation with APEX-Ribo-Seq (Figure 6D), suggesting that nascent peptide-mediated mRNA localization contributed significantly to the local translation profile, as found in the asynchronous cells (Figure 3A).

To characterize the cell cycle phase specificity of local translation, we again performed comparative analysis with eCLIP-Seq datasets. Among the RBPs with significant interactions, FMR1 and FMR2, whose paralog in flies (Fmr1) is known to play a key role in mRNA localization and onsite translation at the centrosome [153], bound to G2-phase and M-phase mRNAs (Figure 6E). The eCLIP-Seq profiles of FMR1 and FMR2 with *JARID2* mRNA, which was detected by centrosome APEX-Ribo-Seq in asynchronous cells, were similar to the attention weights from TransLocAttn (Figure 4D). *Drosophila* Fmr1 is suggested to suppress the translation of centrosomal mRNAs in the cytosol, preventing unwanted protein expression at nontarget sites [153]. A similar mechanism may occur for subsets of centrosomal mRNAs in humans, enabling phase-dependent local translation at this organelle.

In asynchronous cells, we found that EIF4G2 may bind to mRNAs translated on the centrosome (Figure 3C). We thus investigated whether EIF4G2 might facilitate on-centrosome translation in a phase-dependent manner. Leveraging previously generated standard Ribo-Seq and RNA-Seq data from *EIF4G2* KO cells [154], we found that the translation of M phase-specific mRNAs was especially facilitated by EIF4G2 (Figure 6F). These data suggest the presence of a cell cycle phase-dependent regulator of local protein synthesis at the centrosome.

Local translation at stress granules

In addition to the internal cues, we investigated the local translation dynamics upon external cues, especially stresses. Here, we focused on the stress granule, an RNA–protein condensate [155]. Historically, mRNAs within stress granules were considered translationally repressed [155]. However, recent studies using single-molecule imaging with nascent chain tracking reporters have challenged this idea [38–40]. Here, we surveyed the endogenous mRNAs that may be translated in/on stress granules in a more unbiased manner using G3BP1, a well-established marker of stress granules [64,76,156–161], as the bait for APEX2 (Figure S8A). We induced stress granule formation by thapsigargin (Tg) (Figure S8B), which leads to Ca^{2+} ion leakage from the ER triggering an integrated stress response, and subsequently performed APEX-Ribo-Seq (Figure S8C-E and and Table S3). The read enrichment was calculated in comparison with the data obtained from solvent-treated cells (Figure S8F). The effect of ER stress was confirmed by the increased translation of uORF-containing genes [162] (Figure S8G). Our survey revealed 14 translationally active mRNAs proximal to stress granules (Figure 6G). Strikingly, this list

included *ATF4*, an mRNA whose active translation in stress granules has been observed by nascent chain tracking [38].

Given that stress granules may recruit a variety of mRNAs [64,163], active translation activation inside or peripheral to stress granules may be mRNA-selective. To investigate this point, we conducted parallel APEX-RNA-Seq (Figure S8H). This analysis revealed 131 mRNAs enriched in the stress granules (Figure 6H). Consistent with earlier reports [38,40,64,164,165], these stress granule-enriched mRNAs possessed 5′ terminal oligopyrimidine (TOP) motifs [166] (Figure S8I). A comparative analysis using eCLIP-Seq revealed a strong interaction between the 5′ UTRs of the accumulated mRNAs and TIA1, as suggested in a previous study [164] (Figure S8J).

Generally, the enrichment profiles from APEX-Ribo-Seq and APEX-RNA-Seq were distinct (Figure 6I), indicating the specificity of active translation in/on the stress granules. Notably, actively translated *GPX4* mRNA has been observed to localize to stress granules in smFISH experiments [167] (Figure 6I).

mRNA–ribosome complexes on the autophagosome

To further extend our investigation of local translation at stress-induced loci, we focused on the autophagosome, a membranous organelle [168,169]. We used LC3B, which is an adaptor protein that bridges the autophagosome membrane and cargo receptor proteins [168,169], as the bait for APEX-Ribo-Seq (Figure S9A). After inducing autophagy by amino acid depletion for 1 h (Figure S9B), we performed APEX-Ribo-Seq and input Ribo-Seq (Figure S9C-E and Table S3). Consistent with an earlier report [170], amino acid starvation resulted in a translational signature of 1) mTORC1 inhibition, represented by the repression of 5′ TOP mRNA (Figure S9F) and 2) the integrated stress response (ISR),

represented by the activation of uORF-containing mRNAs [162] (Figure S9G). Analysis of the stress-dependent read enrichment in LC3B APEX-Ribo-Seq data (Figure S8F) revealed 755 mRNAs complexed with ribosomes on autophagosomes (Figure 6J). A weak correlation of autophagosome APEX-Ribo-Seq with parallel APEX-RNA-Seq (Figure S9H-J) was observed, suggesting a substantial role for onsite translational control.

Our characterization of complex formation revealed that BORC complexes [171], which have been proposed to regulate autophagic flux, such as membrane fusion with autophagosomes and lysosomes [172], were supplied locally (Figure 6J-K). STRING analysis also revealed significant enrichment of histone and ribosomal proteins (Figure 6K). Indeed, the localization of those proteins to the autophagosome was observed in proteomic analysis; histone protein enrichment was specific to the LC3 secretome [173], whereas ribosomal proteins were detected in the LC3 interactome [174] (Figure S9K). Given that these nucleic acid-binding proteins are positively charged, nascent chains emerging from the ribosome, similar to the mature proteins, may be recruited to negatively charged autophagosomes [175]. Consistent with this hypothesis, the 100 N-terminal amino acids of proteins locally translated on autophagosomes presented a high positive charge (Figure 6L). This property may partially explain the selective mRNA degradation mediated by high ribosome load that has been reported in yeast [176].

APEX-Ribo-Seq in primary neuron culture

Finally, we extended our investigation to mouse primary neurons and local translation at dendrites, axons, and presynapses [11] (Figure S10A). APEX2 tagging of Map2 [177], Nefl [178], and Snca [179] enabled labeling at dendrites, axons, and presynapses (Figure S10B). Using this setup, we conducted APEX-Ribo-Seq in the corresponding neuronal

compartment (Figure S10C-E and Table S4) and calculated the read enrichment relative to the input (Figure S10F). We identified 1023 genes locally that were translated in neuronal subcellular compartments (Figure 7A-B). Gene Ontology (GO) analysis confirmed the enrichment of mRNAs encoding proteins associated with corresponding CCs (Figure S10G). Comparison of our APEX-Ribo-Seq dataset with previously reported datasets, including RNA-Seq [180], Ribo-Seq [52], and translating ribosome affinity purification (TRAP)-Seq [181] from microdissected neuropil data, revealed moderate concordance (Figure S10H), which is at least partially due to the mixture of diverse neuronal compartments in neuropils. Recent data from TurboID-based proximity ligation (PL)-Ribo-Seq of dendrites [62] were most congruent with the APEX-Ribo-Seq profiles, especially for dendrite translation surveys (Figure S10H-I). The majority of surveyed mRNAs were translated at only one of the studied neuronal compartments (Figure 7C-D), indicating that these compartments possess distinct translation programs.

The assessment of RNA localization with simultaneous APEX-RNA-Seq at each locus (Figure S10J) revealed a low correlation with local translation (Figure 7E). As in APEX-Ribo-Seq (Figure S10F), we identified more than 2000 mRNAs localized to each compartment (Figure S10K). In contrast to the local translation profiles (Figure 7C-D), the RNA localization profiles could not be used to distinguish the neuronal compartments (Figure 7F-G); a wider array of mRNAs localized to two or three neuronal compartments. Indeed, our findings were consistent with those of previous studies suggesting highly mRNA-selective translational activation [182] and simultaneous maintenance of other mRNAs at low translation efficiency before stimuli [45,53,183]. This may be related to the formation of neuronal RNP granules [184], which could maintain mRNAs inaccessible to translational machinery.

The 5′ UTRs, ORFs, and 3′ UTRs of neuropil-localized/translated mRNAs are longer than those of somatic mRNAs [62,181]. The characteristics of the mRNAs present at the three neuronal compartments were consistent with these features (Figure S10L). However, locally translated mRNAs showed a differential contribution of those RNA elements, suggesting that 3′ UTR length may not be detrimental for onsite translation at dendrites and presynapses (Figure 7H).

We also explored the enrichment of complex subunits supplied in neuronal compartments by STRING. The local synthesis of chaperonin-containing t-complexes (CCT complexes, also known as T-complex protein Ring Complexes, or TRiCs) and/or chaperone complexes (including Hsp90, Hsp70, and Hsp40) in the neuronal compartments (Figure 7I) suggested the importance of local protein folding. We also identified the tubulin complex, which functions as a key determinant of neuronal polarity beyond a mere structural element [185], as a complex supplied specifically in dendrites, and complexes for glycolysis and the citrate cycle, which may facilitate the maintenance of local ATP [186], supplied specifically in axons (Figure 7I).

Conclusion

In this study, we introduced APEX-Ribo-Seq as a robust and versatile platform for profiling local translation at subcellular compartment resolution. After optimizing APEX2-mediated proximity labeling for ribosome and RNA purification, we surveyed translation across 14 distinct subcellular regions, as well as at 3 cell cycle phases for centrosomes, 2 stress-induced organelles under stress conditions, and 3 neuronal compartments, revealing strong and dynamic connections between organelle/locus/compartment functions and their locally supplied proteins. This comprehensive survey demonstrates the substantial advantages of APEX-Ribo-Seq over preexisting methods. First, this technique does not require the purification of organelles/loci/compartment *per se,* avoiding cell fixation or crosslinking, and uses a simple and common protocol for labeled complex purification that can be applied to any subcellular region. Second, our labeling and purification approach is compatible with RNA-Seq, allowing dissection of the contribution of translation control beyond RNA localization. This point is typically difficult to address through BirA–Avi-tagged ribosome-based methods [21,57,60,61]. Third, our technique has fine temporal resolution, with a labeling time of only 1 min (shorter than the 30 min of biotin exposure in TurboID-based PL-Ribo-Seq [62]), enabling the capture of translation profiles before the diffusion of the mRNA–ribosome complex to other subcellular regions.

The perspective provided by our transcriptome-wide, unbiased APEX-Ribo-Seq method complements recent single-molecule imaging approaches, such as ribosome-bound mRNA detection using proximity ligation and *in situ* sequencing (RIBOmap) [50], high-throughput mRNA detection (multiplexed error-robust FISH [MERFISH] [187] and bacterial artificial chromosome [BAC]-based screening [19]), and the puromycin labeling

with a proximity ligation assay (puro-PLA) [188]. The subcellular heterogeneity of ribosome distribution revealed by ribosome expansion microscopy (RiboExM) [61] and density-based localization monitoring for RNAs and proteins [189] could be integrated with our dataset for a deeper understanding of the molecular mechanism involved in local translation.

Limitations of the study

Although APEX2 has provided successful results for local proteome [65,66,73,75,190–194] and transcriptome [63,64,74] identification, the reaction specificity in cells and the purity of the biotin-labeled complex *in vitro* require further optimization. Here, we carefully conducted enrichment analysis, considering both total input and cytosolic controls (Figure S2E). To achieve this normalization, 4 conditions (and their replicates) of Ribo-Seq/RNA-Seq are needed to calculate localization enrichment for one target.

Another drawback involves the estimation of the fraction of mRNA that is locally translated, because deep sequencing-based approaches need to rely on relative enrichment analysis. The actual fraction of the mRNA localized/locally translated must be validated by smFISH or analogous microscopic analysis.

Because it is based on short reads, Ribo-Seq lacks the resolution to distinguish transcript isoforms, which may have distinct 5′ UTR and 3′ UTR sequences and possess different patterns of mRNA localization and translation control [195,196].

While our language model-based approach demonstrates that high-dimensional embeddings capture information beyond traditional features such as motif enrichment or region length, a current limitation is the incomplete understanding of the specific sequence determinants learned by the model. Although TransLocAttn identifies transcript

regions influential for localization prediction that correlate with RBP interactions, precisely decoding the specific sequence features within these regions that drive the model's attention will be an interesting next step. One strategy will be to enhance model interpretability based on methods adopted from natural language models, as has been recently applied in DNA models [145].

We determined the differential translation elongation rates associated with local translation on the ERM and OMM (Figure 4). This measurement requires a "metagene" plot to estimate the ribosome-free region downstream of start codons [72,147]. Therefore, significant mRNA species are needed for reliable analysis. Kinetic measurements were restricted to loci that have many locally translated mRNAs.

Finally, the application of APEX-Ribo-Seq is currently limited to cultured cells; further technical development is needed for *in vivo* testing.

Acknowledgments

We are grateful to all the members of the Iwasaki laboratory, Dr. Kosuke Dodo, Dr. Yutaka Ogawa, Dr. Fubito Nakatsu, Dr. Franz Meitinger, Dr. Midori Ota, Dr. Akihiko Nakano, Dr. Tomoko Kawamata, Dr. Hotaka Kobayashi, and Dr. Kenji Ohtawa, for their constructive discussions and technical help. A portion of the deep sequencing was performed at the Advanced Genomics Center, National Institute of Genetics, Mishima, Shizuoka, Japan, and supported by JSPS KAKENHI Grant Number JP22H04925 (PAGS). Computation was supported by the HOKUSAI SailingShip supercomputer facility at RIKEN. We are grateful to the Support Unit for Bio-Material Analysis, RIKEN CBS Research Resources Division, for Sanger sequencing and flow cytometry analysis. This work was supported by the Ministry of Education, Culture, Sports, Science and Technology (MEXT) (JP24H02307 to S.I.; JP21H05734, JP23H04268, and JP25H01440 to Y.S.), the Japan Agency for Medical Research and Development (AMED) (JP20gm1410001 to S.I.; JP23gm6910005 to Y.S.), the Japan Society for the Promotion of Science (JSPS) (JP23H02415 and JP23H00095 to S.I.; JP21K15023 and JP23K05648 to Y.S.; JP23H00095 to K. Kawaguchi), the Japan Science and Technology Agency (JST) (JPMJBS2418 to K.T.), the Japan Science Society (the Sasakawa Scientific Research Grant to K.T.), the Nakajima Foundation (to Y.S.), the Exploratory Research Center on Life and Living Systems (ExCELLS) (23EXC601-2 and 25EXC602-4 to Y.S.; 23EXC601 and 25EXC602 to N.S.), and RIKEN (Pioneering Projects to S.I. and Y.S.; RIKEN TRIP initiative “TRIP-AGIS” to S.I.). K.T. was supported by a Junior Research Associate Program (JRA) from RIKEN, the World-leading Innovative Graduate Study Program in Proactive Environmental Studies (WINGS-PES) from The University of

Tokyo, and Broadening Opportunities for Outstanding young researchers and doctoral students in STrategic areas (BOOST) from JST.

Author contributions

Conceptualization, K.T., Y.S., and S.I.;

Methodology, K.T., K. Kawaguchi, and Y.S.;

Formal analysis, K.T., K. Kawaguchi, and Y.S.;

Investigation, K.T., T.A., A.H., K. Kobayashi, K. Kawaguchi, and Y.S.;

Writing – Original Draft, K.T., Y.S., and S.I.;

Writing – Review & Editing, K.T., T.A., A.H., K. Kobayashi, N.S., K. Kawaguchi, Y.S., and S.I.;

Visualization, K.T.;

Supervision, N.S., K. Kawaguchi, Y.S., and S.I.;

Project administration, K. Kawaguchi, Y.S., and S.I.;

Funding Acquisition, K.T., K. Kawaguchi, N.S., Y.S., and S.I.

Competing Interests

S.I. is a member of the editorial board of *Scientific Reports*. The remaining authors declare that they have no competing interests.

Methods

Ethics statement

All animal procedures were approved by the Animal Experiment Committee of the National Institutes of Natural Sciences (Approval No. 24A024) and conducted in accordance with institutional guidelines and the recommendations of the Science Council of Japan.

Cell culture

HEK293 Flp-In T-REx cells (or HEK293 T-REx; Thermo Fisher Scientific, R78007) with and without stable integration of APEX2-bait (Figures S1A, S8A, and S9A) were maintained in DMEM, high glucose, GlutaMAX Supplement (Thermo Fisher Scientific, 10566024) supplemented with 10% fetal bovine serum (FBS, Sigma–Aldrich) at 37°C and 5% CO_2.

DNA construction

pcDNA5/FRT/TO-APEX2 plasmids

The APEX2 gene with organelle-targeting signals or organelle markers was cloned and inserted into the pcDNA5/FRT/TO vector (Thermo Fisher Scientific, V652020) (Figure S1A, S8A, and S9A). PCR amplification and assembly of the DNA fragments were performed with PrimeSTAR MAX (TaKaRa, R045A) and In-Fusion HD (TaKaRa, 639649), respectively. For the constructs designed to target the cytosol (NES), mitochondrial matrix, endoplasmic reticulum membrane (ERM), and outer mitochondrial membrane (OMM), we followed the procedures used in previous APEX-Seq studies [63,64,66]. For peroxisomes, *cis*-Golgi, *trans*-Golgi, lysosomes, endosomes, early endosomes,

cell junctions, intermediate filaments, and clathrin-coated vesicles, we selected marker proteins on the basis of proximity proteomics data [97]. We used the transmembrane domain of GAP43 for the plasma membrane [197,198], SYNE3 for nuclear pore complexes [199], G3BP1 for stress granules [76], and LC3B (or MAP1LC3B) for autophagosomes [173,174,200].

pSEPT-CEP192-APEX plasmid

The pSEPT-CEP192-APEX2 construct was generated from the pSEPT-CEP192-NeonGreen plasmid [201], replacing NeonGreen with APEX2 and V5 tag.

pAAV[Exp]-CBh>bait-APEX-GFP:WPRE3 plasmids

Neuronal compartment markers tagged with APEX2-GFP at the C-terminus were cloned and inserted into a single-stranded adeno-associated virus (ssAAV) mammalian gene expression vector containing a CBh promoter and a WPRE3 regulatory element (Figure S10A). We used mouse Map2 for dendrites [177], mouse Nefl for axons [178], and mouse Snca for presynapses [179]. All pAAV[Exp] vectors were constructed by Vector Builder.

Generation of cell lines

The pcDNA5/FRT/TO vectors were stably integrated into the HEK293 T-REx genome via cotransfection with pOG44 (Thermo Fisher Scientific, V600520) using X-tremeGENE9 (Roche, 6365809001) and selected with blasticidin S (InvivoGen, ant-bl-1) and hygromycin B (InvivoGen, ant-hg-1). In the subsequent experiments, cells were incubated with tetracycline for 3 d to induce APEX2 protein expression.

For the CEP192-APEX2-V5 cell line, we performed a C-terminal knock-in to the endogenous locus using the CRISPR-Cas9 system as previously described [201] with

modifications. The vector expressing Cas9 and guide RNA targeting the C-terminal region of the *CEP192* gene was cotransfected with the repair construct pSEPT-CEP192-APEX using Lipofectamine 3000 (Thermo Fisher Scientific, L3000015). After incubation for 14 d with G418 (InvivoGen, ant-gn-1), integrants were seeded in 96-well plates at 0.1 cells per well to isolate single-cell clones. Integration was confirmed by immunostaining.

Drug treatment

CEP192-APEX2-V5 cells were treated with 500 nM centrinone-B (Tocris Bioscience, 5690) for 4 d to deplete centrosomes.

To induce stress granules, V5-APEX2-G3BP1 cells were treated with 500 nM thapsigargin (nacalai tesque, 33637-31) for 30 min.

Cell cycle phase synchronization by RO-3306 treatment

For cell cycle phase synchronization, we modified the original protocol for RPE-1 cells [152]. The cells were treated with 10 μM RO-3306 (Merck Millipore, 217699) for 18 h and either harvested for use as G2-phase samples or washed 3 times with fresh medium and incubated for a further 1.5 h to serve as M-phase samples (or mitotic shake off) or for an additional 7.5 h to serve as G1-phase samples.

The cell cycle phase composition of each sample was validated by flow cytometry. For this purpose, the cells were trypsinized and fixed with methanol for 1 h at 4°C. After washing with PBS, the cells were incubated with 10 μg/ml propidium iodide (nacalai tesque, 19174-31) and 100 μg/ml RNase A (nacalai tesque, 30100-31) for 30 min at 37°C. All centrifugation steps were performed at 800 × g for 3 min. Cell cycle phase profiles

were acquired on a FACSAria II Special Order system (BD) using FACSDiva software (BD, ver. 6.1.3).

Amino acid starvation

HEK293 T-REx cells expressing V5-APEX2-LC3B were seeded and cultured in amino acid-containing DMEM (Fujifilm Wako, 040-30095) supplemented with 2 mM GlutaMAX-I (Thermo Fisher Scientific, 35050-061), 1 mM sodium pyruvate (nacalai tesque, 06977-34), and 10% FBS. To induce amino acid starvation, the cells were washed three times with amino acid–free DMEM (Fujifilm Wako, 048-33575) containing 10% FBS and then incubated in this medium for 1 h.

Primary neuron culture and AAV production

The AAV vectors were packaged as described previously [202] using the AAV-DJ Helper Free Expression System (Cell Biolabs, VPK-410-DJ). Briefly, pAAV transfer plasmid was transfected into HEK293T cells with packaging plasmids. The AAV vector particles in the crude lysates were purified by serial ultracentrifugation with cesium chloride and dialyzed against PBS containing 0.001% Pluronic F-68 (Sigma–Aldrich, P5556-100ML), followed by concentration with an Amicon 10 K MWCO filter (Merck Millipore, UFC801096). The viral genome (vg) copy number was measured by real-time quantitative PCR with primers targeting the WPRE3 region (forward 5′-GGTATTCTTAACTATGTTGCTCCTT-3′ and reverse 5′-GAATTGTCAGTGCCCAACAG-3′).

Primary cortical neurons were prepared as previously described [203]. Briefly, cortices were isolated from embryonic day 15.5 (E15.5) ICR mouse embryos,

enzymatically and mechanically dissociated, and plated onto poly-D-lysine-coated 10-cm culture dishes at 2.0×10^6 cells/ml. The neurons were maintained in a humidified 5% CO_2 incubator at 37°C in Neurobasal-A medium (Thermo Fisher Scientific, 10888-022) supplemented with 2% B-27 (Thermo Fisher Scientific), 1% GlutaMAX (Thermo Fisher Scientific, 35050-061), and 25% Neuron Culture Medium (FUJIFILM Wako, 148-09671). At 6 days *in vitro* (DIV6), AAV vectors were added directly to the culture medium at a final concentration of 1.4×10^{11} vg/ml. Neurons at DIV9 were used for downstream experiments.

In situ APEX labeling in human cell culture and mouse primary neurons

APEX labeling was initiated by replacing the culture medium with fresh medium containing 0.5 mM desthiobiotin tyramide (Iris Biotech, LS-1660). For cultured primary neurons, 0.5 mM desthiobiotin tyramide was added directly to the medium. After a 30 min incubation, the reaction was started by treating the cells with a final concentration of 1 mM H_2O_2 (nacalai tesque, 18411-25) for 1 min at room temperature. The reaction was quenched by replacing the medium with quench-PBS buffer consisting of 10 mM sodium azide (nacalai tesque, 31233-42), 10 mM sodium ascorbate (Sigma–Aldrich, A7631), and 5 mM Trolox (Sigma–Aldrich, 238813) in PBS; the cells were subsequently washed twice with quench-PBS buffer. After the second wash step, the cells were immediately placed on ice.

Quenched cells were lysed directly on dishes with 500 µl of APEX lysis buffer (20 mM Tris-HCl pH 7.5, 150 mM NaCl, 5 mM $MgCl_2$, 1% Triton X-100, 1 mM dithiothreitol, 100 µg/ml cycloheximide, 100 µg/ml chloramphenicol, 10 mM sodium azide, 10 mM sodium ascorbate, and 5 mM Trolox) and incubated with 25 U/ml TURBO

DNase (Thermo Fisher Scientific, AM2238) for 10 min. After DNase treatment, the lysates were clarified by centrifugation at 20,000 × g for 10 min at 4°C.

Purification of desthiobiotinylated ribosomes and RNAs

To remove unreacted desthiobiotin tyramide, the supernatant was applied to a NAP5 column (Cytiva, 17085302) according to the manufacturer's instructions. Elution was performed with 1000 µl of APEX lysis buffer, and 150 µl of the lysate was retained to serve as the input samples for APEX-Ribo-Seq and APEX-RNA-Seq. The remaining lysate was subjected to further purification.

To enrich the sample for biotinylated proteins and RNA, 100 µl of Dynabeads MyOne Streptavidin C1 (Thermo Fisher Scientific, 65002) preequilibrated with APEX lysis buffer was added to the NAP5 eluate and incubated at 4°C for 1 h. The beads were washed five times with 500 µl of APEX lysis buffer, with transfer to a fresh tube during each wash step. For elution, the beads were resuspended in 150 µl of APEX lysis buffer supplemented with 5 mM D-biotin (Thermo Fisher Scientific, B20656) and incubated overnight at 4°C. The supernatant was collected, and the beads were preincubated with an additional 150 µl of APEX lysis buffer containing 5 mM D-biotin for 1 h at 4°C. This elution step was repeated twice, yielding 450 µl of eluate in total.

Library preparation for Ribo-Seq

For the streptavidin pulldown and corresponding input samples, Thor-Ribo-Seq library preparation was performed with 300 µl of eluate and 100 µl of lysate, respectively [71]. Briefly, lysates were treated with 0.067 U/µl RNase I (LGC Biosearch Technologies, N6901K) at 25°C for 45 min. After ultracentrifugation, RNA was extracted from the

ribosome pellet using TRIzol reagent (Thermo Fisher Scientific, 15596018) and a Direct-zol RNA MicroPrep Kit (Zymo Research, R2062). The RNA fragments corresponding to 17–34 nt in length were excised from the gel, dephosphorylated by T4 polynucleotide kinase (New England Biolabs, M0201S), and ligated to the 3′ DNA linkers containing barcodes and the T7 promoter sequence by T4 RNA Ligase 2, truncated KQ (New England Biolabs, M0373L). After hybridization of complementary DNA to the T7 promoter sequence, RNAs were amplified by *in vitro* transcription using the T7-Scribe Standard RNA IVT Kit (CELLSCRIPT, C-AS3107). rRNA depletion was performed using Human Ribo-Seq riboPOOL (siTOOLs biotech, dp-K024-000042) and Mouse-Rat Ribo-Seq riboPOOL (siTOOLs biotech, dp-K024-000052). The RNAs were then ligated with a 5′ linker, reverse transcribed with ProtoScript II Reverse Transcriptase (New England Biolabs, M0368L), and amplified by PCR.

For the centrinone B-treated samples, cell lysates containing 10 μg of total RNA were used for the Thor-Ribo-Seq library preparation. The RNA concentration of the lysates was measured with a Qubit RNA BR kit (Thermo Fisher Scientific, Q10210).

Library preparation for RNA-Seq

For the streptavidin pulldown and corresponding input samples, total RNA was extracted from 150 μl of eluate and 50 μl of lysate, respectively, with TRIzol LS (Thermo Fisher Scientific, 10296-010) and a Direct-zol RNA MicroPrep Kit (Zymo Research, R2062). The libraries were prepared using the SEQuoia Express Stranded RNA Library Prep Kit (Bio-Rad, 12017265). For the centrinone B-treated samples, 500 ng of total RNA extracted from the cell lysate was used.

All libraries were sequenced on a NovaSeq 6000, NovaSeq X Plus, or HiSeq 4000 system (Illumina) to produce 150-nt paired-end reads (Table S5).

SDS–PAGE, SYPRO Ruby protein staining, and Western blotting

Equal amounts of purified lysates from APEX2-NES-EGFP cells under the indicated conditions were separated by SDS-PAGE. The gels were stained with SYPRO Ruby Protein Gel Stain (Thermo Fisher Scientific, S12001) and imaged using a Pharos FX imaging system (Bio-Rad).

For Western blotting, the proteins were transferred from the gels to nitrocellulose membranes, which were subsequently blocked with Intercept (TBS) Blocking Buffer (LI-COR, 927-60001). Immunoblotting was performed using an anti-RPS17 (Abcam, AB138991, 1:1,000) primary antibody and an IRDye 680RD anti-rabbit IgG (LI-COR, 926-68071, 1:10,000) secondary antibody. IRDye 800CW streptavidin (LI-COR, 925-32230, 1:2,000) was used for the detection of desthiobiotinylated proteins. Images were acquired with an Odyssey CLx imager (LI-COR).

Polysome profiling

Polysome profiling was performed as previously described [204,205], with some modifications. Lysates with in situ APEX labeling (as described in the "*In situ APEX labeling in human cell culture and mouse primary neurons*" section) were loaded onto the top of a 10–50% (w/v) sucrose gradient in APEX polysome buffer (20 mM Tris-HCl pH 7.5, 150 mM NaCl, 5 mM $MgCl_2$, 1 mM dithiothreitol, 100 µg/ml cycloheximide; and 10 mM sodium azide) and centrifuged at 221,230 × g for 2.5 h at 4°C in a P40ST rotor (Hitachi Koki). Fractionation and absorbance monitoring were performed using the

Gradient Station (BioComp) and the TRiAX Flowcell (BioComp). For Western blotting, the fractions were incubated with 20% trichloroacetic acid (Fujifilm Wako) for 20 min on ice and then centrifuged at 20,000 × g for 15 min at 4°C. The precipitates were washed twice with 150 µl of ice-cold acetone, dried, and resuspended in 15 µl of 1 M Tris-HCl, pH 7.5. For RNA dot blotting, RNA was extracted from the fractions using a Maxwell RSC simplyRNA Cells Kit (Promega, AS1390) and a Maxwell RSC Instrument (Promega).

RNA dot blotting

The RNA samples were diluted in RNA denaturing buffer (50% dimethyl sulfoxide and 1 M glyoxal in 0.01 M Na_2PO_4-$NaHPO_4$ buffer, pH 7.5) and incubated at 50°C for 1 h. The mixtures were spotted on a Zeta-Probe blotting membrane (Bio-Rad, 1620153) with Bio-Dot SF (Bio-Rad, 1706542), then washed once with 100 µl of TE buffer (10 mM Tris-HCl and 1 mM ethylenediaminetetraacetic acid, pH 8.0) and once with 100 µl of 2×SSC (0.3 M NaCl and 0.03 M sodium citrate, pH 7.0). The membranes were then dried, incubated at 80°C for 1 h for crosslinking, blocked for 2 h using Intercept (TBS) Blocking Buffer with 1% SDS, and blotted with IRDye 800CW Streptavidin (LI-COR, 925-32230, 1:2,000). Total RNA was visualized using methylene blue staining buffer (0.2% methylene blue in 0.4 M sodium acetate and 0.4 M acetic acid). Images were acquired using an Odyssey CLx (LI-COR).

Immunofluorescence staining and fluorescence microscopy

Cells seeded on 12-mm coverslips (Matsunami glass, C012001) were fixed in 4% paraformaldehyde in PBS at room temperature for 15 min. After two washes with PBS,

the cells were permeabilized in 0.1% Triton X-100 in PBS at room temperature for 10 min, again washed twice with PBS, and blocked for 1 h at room temperature in Intercept (TBS) Blocking Buffer (LI-COR, 927-60001) containing 0.2% Triton X-100. The cells were then incubated overnight at 4°C with the primary and secondary antibodies listed in Table S6. The cells were washed twice with PBS containing 0.2% Triton X-100 and mounted in VECTASHIELD Vibrance (Vector Labs, H-1800). Images were acquired using a Zeiss LSM 710 confocal microscope with a 63× objective lens (Zeiss, Plan-Apochromat 63x/1.4 Oil DIC M27) or an Olympus IX83 inverted microscope with a 100× objective lens (Olympus, UPLXAPO100XO) and a CMOS camera ORCA-Fusion (Hamamatsu Photonics, C15939-20U).

smiFISH

Single-molecule inexpensive FISH (smiFISH) was performed as previously described [92,206] with modifications. Cells seeded on 12-mm coverslips were fixed in 4% paraformaldehyde in PBS at room temperature for 15 min, washed three times with PBS, and then permeabilized in 70% ethanol in PBS overnight at 4°C. After two washes with PBS, the coverslips were incubated with 120 µl of prehybridization buffer (2×SSC containing 10% formamide, 5 mg/ml UltraPure BSA [Thermo Fisher Scientific, AM2618], 2 mM vanadyl ribonucleoside complexes solution [Sigma–Aldrich, 94742], and 0.1% Triton X-100) for 30 min at room temperature and subsequently hybridized with FLAP probes.

To prepare the FLAP probes, target-specific oligonucleotide probe sets (0.4 µM each, listed in Table S7) were mixed with 20 µM Cy3- or Cy5-labeled FLAP oligo (synthesized by Integrated DNA Technologies) in FLAP buffer (5 mM Tris-HCl pH 7.5,

10 mM NaCl, and 1 mM $MgCl_2$). The mixture was incubated at 85°C for 3 min, 65°C for 3 min, and 25°C for 5 min using a thermal cycler for annealing and then held at 12°C until use.

For hybridization, cells on coverslips were placed on a drop of 20 µl hybridization mix comprising FLAP probe duplexes (4 nM each), 10% formamide, 0.5 mg/ml BSA, 2 mM vanadyl ribonucleoside complex, 0.1% Triton X-100, 1 mg/ml yeast tRNA (Thermo Fisher Scientific, AM7119), and 12% dextran sulfate and incubated at 37°C for 3 h. Coverslips were then washed three times with RNA wash buffer (2×SSC containing 10% formamide and 0.1% Triton X-100) and incubated in RNA wash buffer for 30 min at 37°C, followed by immunostaining and mounting as described in the "*Immunofluorescence staining and fluorescence microscopy*" section. Images were obtained with an Olympus IX83 inverted microscope with a 100× objective lens (Olympus, UPLXAPO100XO) and a CMOS camera ORCA-Fusion (Hamamatsu Photonics, C15939-20U).

smiFISH spot detection and quantification

smiFISH images were processed as maximum-intensity z-projections and then analyzed using a custom pipeline in Fiji (ImageJ, ver. 2.16.0) [207] and then analyzed using a custom pipeline. Nuclei were segmented via CellPose (ver. 2.2, nuclei model) [208], and cell boundaries were estimated by watershed expansion of nuclear masks within cytoplasmic regions defined by the smiFISH fluorescence signal. Organelle masks were generated for each image by applying an organelle-specific Laplacian of Gaussian filter, followed by adaptive thresholding. To refine each mask, small objects and holes were removed by size-based morphological filtering using the "skimage.morphology" module. The

detailed filtering and thresholding parameters for each organelle are provided in Table S7.

smiFISH puncta were detected with Big-FISH (ver. 0.6.2) [209] using parameters optimized for a 100 nm pixel size and ~150 nm spot radius. The detected spots were assigned to individual cells on the basis of their spatial overlap with the segmentation masks. Colocalization with organelles was defined by whether the center of a spot fell within the refined organelle masks in the corresponding cell. The number and fraction of colocalized spots were quantified on a per-cell basis.

Mapping of deep sequencing data

The libraries generated in this study are summarized in Table S5. The sequencing reads were processed as previously described [71,210]. Briefly, we used fastp (ver. 0.21.0) [211] for read quality filtering and adapter trimming, cutadapt (ver. 3.7) [212] for demultiplexing by linker barcodes, and UMI-tools (ver. 1.1.2) [213] for deduplication on the basis of unique molecule identifiers. Reads that mapped to noncoding RNAs were removed, and the remaining reads were aligned to the human genome hg38 or mouse genome mm39 and assigned to the GENCODE Human release 44 reference or Mouse VM36 reference using STAR (ver. 2.7.0a) [214]. Libraries of poor quality (see Table S5 for details) were used only to show the correlation between replicates (Figure S3E and S5B) and were excluded from other downstream analyses. All downstream analyses focused exclusively on canonical transcripts defined by MANE Select (ver. 1.0) for humans [215]. Ensembl canonical genes that were missed by MANE Select were also included in the list. For the mouse datasets, the Ensembl canonical gene set was used.

Enrichment calculation for 14 organelle compartments

Transcripts with ≥10 read counts in both NES-Pulldown replicates (7408 genes in total) were included for downstream APEX-Ribo-Seq and APEX-RNA-Seq analyses of the 14 organelles. Mitochondrial genome-encoded genes were excluded, except for the matrix APEX-Ribo/RNA-Seq datasets and the associated analysis. Genes used as APEX baits were also excluded.

Differential expression analysis of the read counts was performed using DESeq2 (ver. 1.32.0) [216]. The $\log_2$-transformed fold enrichment for each region was calculated by comparing the count for each pulldown to that of the cytosolic control, with normalization to the input samples, *i.e.*, $\log_2$[(target pulldown/input)/(cytosol pulldown/input)] (Figure S2E). The input libraries for all 14 regions were handled as replicates, as previously described [63].

The specificity and sensitivity of ERM APEX-Ribo-Seq were evaluated via receiver operating characteristic (ROC) curve analysis [91]. Using BirA proximity-specific ribosome profiling as a positive reference [57], positive mRNAs for local translation were defined by $\log_2$ fold enrichment (ERM/cytosol) > 0.503 and adjusted P value < 0.05 (Figure S2F). These criteria were applied to all 14 organelle datasets of both APEX-Ribo-Seq datasets. The $\log_2$ fold enrichment for all analyzed mRNAs across each subcellular location are summarized in Table S1.

Protein annotations and localization database

Annotation of secretory and membrane-inserted/translocated genes was performed using Phobius [217], TMHMM [218], and SignalP [219], as described in earlier studies [63,65]. MitoCarta 3.0 [95] was used for the annotation of mitochondrial proteins. For the autophagosome

analysis, the autophagosome interactome [174] and the autophagosome secretome [173] were used.

Protein localization data were obtained from two sources: immunofluorescence-based annotations in the Human Protein Atlas (HPA) [97,106] and a proximity-dependent biotinylation dataset generated via BioID [97,106]. For the HPA dataset, we used 28 major protein localization classes defined by immunofluorescence imaging. For the BioID dataset, we used 19 nonnegative matrix factorization (NMF)-derived localization categories, excluding the "miscellaneous" class. For each dataset, genes identified as positive for a given compartment by APEX-Ribo-Seq were extracted, and the relative abundance of each gene in its corresponding localization categories was calculated.

Functional term clustering by STRING

Functional term clustering was performed using the STRING database (ver. 12.0) [107]. Terms with a high-confidence interaction score cutoff (combined score ≥ 0.7) and a false discovery rate (FDR) < 0.05 were retained for subsequent analyses. Clusters with term similarity > 0.5 were merged. To highlight compartment-specific biological processes, clusters that appeared in more than four compartments were excluded.

Detection of co-co–assembled protein complexes

Locally assembled heteromeric protein complexes were identified using a predicted co-co–translation dataset [129]. Complexes were classified as uniquely co-co–translated if at least one constituent gene was detected exclusively in a single compartment within the local translation atlas.

Enrichment analysis for short sequence motifs

To identify sequence motifs associated with differential translation localization across the 14 compartments, we employed HOMER (ver. 5.1) [220] for *de novo* motif discovery from the full-length transcript sequences in the mRNAs defined in Figure S3G. For each compartment, transcripts were categorized as target (high localization: $\log_2$ fold enrichment > 70th percentile and > 0) or background (low localization: $\log_2$ fold enrichment < 30th percentile and < 0). HOMER was used to compare the target and background sets, searching for enriched RNA motifs of 5–7 nucleotides. We then parsed the results, calculating enrichment *P* values, fold enrichment (%target/%background), and target prevalence (%target) for each identified motif. High-confidence motifs were selected according to the following criteria: *P* value < 1e−5, $\log_2$ fold enrichment > 1.5 and %target > 5.0%.

Linear regression and random forest using sequence lengths

To evaluate the predictive power of basic RNA length features, we employed linear regression and random forest regression. The input features for these models were the lengths of the full transcript, 5′ UTR, ORF, and 3′ UTR. The target variables were the $\log_2$ fold enrichment for the 14 organelles, which were standardized by subtracting the mean and scaling to unit variance. Models were trained using the predefined training set; in all machine learning tasks, we consistently used the data (a total of 3040 sequences with valid sequences) partitioned into training (70%, 2124 sequences), validation (15%, 456 sequences), and testing (15%, 460 sequences) sets using stratified random sampling. For the random forest model, 100 estimators (n_estimators=100) were used with no maximum depth restriction. Model performance was evaluated according to the Pearson's

correlation coefficient between the predicted and true $\log_2$ fold enrichment in the held-out test set for each organelle.

Residual convolutional neural network (CNN) approach

As a baseline for nucleotide sequence-based machine learning, we implemented a residual convolutional neural network (ResNet-CNN). Full transcript sequences were first converted into one-hot encoded representations (A, C, G, U channels) and padded or truncated to a fixed maximum length (set as 15000 nt). The CNN architecture comprised an initial convolutional layer, followed by batch normalization and ReLU activation, succeeded by a series of residual blocks, each containing two convolutional layers, batch normalization, ReLU, dropout, and a shortcut connection to facilitate gradient flow. Key architectural hyperparameters, including the number of filters, kernel sizes, strides (for downsampling), and dilation rates within these blocks, were varied during tuning. Following the residual blocks, a global average pooling layer was applied to condense the sequence dimension into a fixed-size feature vector irrespective of the effective sequence length after convolution. This pooled representation was then processed by a final feed-forward network consisting of a hidden layer with ReLU and dropout, connected to a linear output layer predicting the 14 continuous $\log_2$ fold enrichment.

The Pearson's correlation coefficient shown in Figure 4B was for the model that achieved the highest average Pearson's correlation coefficient across the organelles. This specific architecture used an initial convolutional layer with 32 filters and a kernel size of 7 (stride 1), followed by two residual blocks. The first residual block maintained 32 input channels and output 64 channels using a kernel size of 7 (stride 1, dilation 1). The second block received 64 input channels and output 128 channels using a kernel size of 5 (stride 2,

dilation 1). A dropout rate of 0.3 was applied within the residual blocks and before the final output layer. The final feed-forward network utilized a hidden layer with 128 units.

Per-nucleotide embedding generation for attention model analysis

We utilized the pretrained RiNALMo language model [144] (giga-v1, 650 M parameters) accessed via the rinalmo.pretrained library (https://github.com/lbcb-sci/RiNALMo) to generate feature representations for RNA sequences. Input sequences corresponding to different segments (5′ UTR, ORF, 3′ UTR, or full sequence [5′ UTR+ORF+3′ UTR]) were used. The tokenized sequences were processed by the frozen RiNALMo model to obtain per-nucleotide embeddings from the final transformer layer. This resulted in a tensor of shape (sequence length × embedding dimension 1280) for each input RNA sequence/segment. A similar procedure was conducted for AIDO.RNA 1.6B (embedding dimension 2048) [143]. For the Evo 2 DNA model, we used intermediate embeddings as suggested (layer_name = 'blocks.28.mlp.l3', embedding dimension 4096) [145]. For AIDO.RNA and Evo 2, we removed sequences longer than 7200 nucleotides (28 sequences in total, <1%) as these sequences produced memory errors during the embedding calculation.

Mean-pooling feed-forward network (FNN) approach

We also evaluated a baseline model using mean-pooled embeddings. For this approach, we utilized the per-nucleotide embeddings corresponding to a specific transcript region (5′ UTR, ORF, 3′ UTR, or full sequence). For each transcript within the selected region, a single fixed-size feature vector was generated by calculating the elementwise mean

across all nucleotide embeddings in that sequence. This mean-pooled vector (with dimension 1280) served as the direct input to the regressor.

The regressor itself was a standard feed-forward network (FNN). Its architecture consisted of an input layer matching the pooled embedding dimension, followed by a configurable number of hidden layers employing ReLU activations and dropout for regularization. The final linear layer mapped the features from the last hidden layer to the 14 target compartment outputs.

To evaluate the performances of different RNA language models (RiNALMo, AIDO.RNA, and Evo 2), their respective embeddings were used as inputs for this mean-pooling FNN. The performance, as assessed by the Pearson's correlation between the predicted and experimental $\log_2$ fold enrichment from a held-out test set, is presented in Figure S6C. For these comparisons, an FNN architecture with three hidden layers (containing 512, 256, and 128 units, respectively) was selected, as this configuration yielded the highest average correlation across various input settings. All three embedding types demonstrated strong predictive performance, though RiNALMo and AIDO.RNA embeddings achieved slightly higher correlations than did Evo 2 embeddings.

Interpretable attention regressor model (TransLocAttn)

We developed a feed-forward neural network (FNN) model to predict continuous $\log_2$ fold enrichment across 14 subcellular compartments using precomputed, per-nucleotide RiNALMo embeddings (embedding dimension d_embed=1280). Input representations for each transcript were created by concatenating embeddings derived from its 5′ UTR, ORF, and 3′ UTR regions. To manage the dimensionality of these sequence embeddings, an optional linear projection layer with ReLU activation and layer normalization was

implemented at the input stage, reducing the embedding dimension to a specified size (*e.g.*, d_proj=128 or d_proj=256) before attention processing.

The core of the model utilized an attention pooling module inspired by DeepLoc 2.0 [221]. Instead of a single attention vector, this module learns K (*e.g.*, K=4) distinct attention (query) vectors for each of the 14 target compartments. For a given compartment, each of its K attention vectors is used to independently calculate a set of raw attention scores via dot product with the (potentially projected) per-nucleotide embeddings. These K sets of scores are then individually smoothed along the sequence using a 1D Gaussian filter (sigma=2). Subsequently, K sets of normalized attention weights for that compartment are generated by applying a softmax function across the sequence length to each smoothed score set. Each of these K attention weight sets is then used to compute a compartment-specific, vector-specific pooled representation via a weighted average of the (projected) input nucleotide embeddings. Finally, these K pooled representations for the compartment are averaged to yield a single, robust pooled vector of dimension d_proj for that compartment. The interpretable attention weights for each compartment, used for analysis, are the average of its K corresponding normalized attention weight sets.

This process results in 14 final compartment-specific pooled vectors. Each of these 14 vectors was then fed into its own dedicated FNN prediction head. Each head consisted of typically two or three hidden layers featuring ReLU activation and dropout, culminating in a single linear output neuron predicting the $\log_2$ fold enrichment for that specific compartment. The entire model, including the optional input projection, the multiple attention vectors per task, and the separate FNN heads, was trained end-to-end.

For the final reported results (*e.g.*, Figure 4B), we utilize the model (we call TransLocAttn) with RiNALMo embeddings, K=4 attention vectors per compartment, and

an input projection layer reducing the dimension to d_proj=128. The independent FNN head for each compartment in this example configuration could comprise two hidden layers with 128 and 64 units, respectively. Training hyperparameters were: learning rate of 5e−5, dropout of 0.5, and weight decay of 1e−3.

Attention-based region identification and comparison with eCLIP-Seq

After training, the learned attention weights for sequences in the test set were extracted from the best-performing model configuration. For interpretability, these attention weights, which represent the learned importance of each nucleotide position for generating the compartment-specific pooled representation, were processed and visualized as profiles along the sequence length for the relevant compartments (Figure 4C-E, S6E-F).

To assess whether these model-learned attention profiles corresponded to known protein–RNA interaction sites, we systematically compared these profiles with the collection of eCLIP-Seq datasets [136] (see the "*eCLIP-Seq data processing*" for details). For each gene common to the test set, we processed its association with eCLIP-Seq read distribution.

After filtering eCLIP tracks on the basis of a minimum peak height (min_eclip_peak=10.0), we computed the correlations between each remaining eCLIP-Seq distribution and the smoothed (Gaussian filter, sigma=5) attention profiles corresponding to the gene's most relevant compartments. Two primary metrics were calculated, namely, the Spearman's rank correlation and a tail dependence score assessing the co-occurrence of high-signal regions (signal_frac=0.05 quantile, normalized by signal_frac^2 = 0.0025). The maximum correlation score across the relevant

compartments was retained for each gene-eCLIP pair for both metrics. To estimate significance, these scores were compared against thresholds (sp_threshold=0.6 for the Spearman's correlation coefficient, corr_threshold=2.5 for tail dependence) and against null correlations obtained by comparing attention profiles to randomly shifted eCLIP signals. mRNA-eCLIP pairs exceeding either threshold were deemed significantly correlated. The overall distributions of observed versus randomly shifted correlation scores across all the mRNA-eCLIP pairs were plotted as histograms (Figure S6G-H) and a scatter plot (Figure S6I) to evaluate the global enrichment of high correlations compared with random chance.

eCLIP-Seq data processing

For analysis of the eCLIP-Seq datasets [136], the BAM files aligned to hg38 were obtained from the ENCODE portal (https://www.encodeproject.org). The 5′ ends of the reads corresponding to each region (5′ UTR, ORF, and 3′ UTR, based on the GENCODE Human release 44) were counted. The eCLIP-Seq enrichment was then calculated using DESeq2 (ver. 1.32.0) as the fold change in IP samples relative to size-matched input samples in each region. Only mRNAs with a read count of at least one were included in the analysis. The mean eCLIP enrichment was calculated for each RBP–cell line combination from mRNAs positively enriched in the local translation atlas.

Measuring spatial translation kinetics

Previously reported Ribo-Calibration datasets of HEK293 T-REx cells were used to quantify ribosome number and density [72]. Elongation rates were estimated from ribosome run-off assay data within the same dataset, filtering the mRNAs locally translated at the

ERM or OMM. To ensure that a sufficient number of genes were included in analysis, we selected genes with ORFs of more than 1000 codons. Read counts were normalized to the average read density within the 800–1000 codons from the start codon. Translation initiation rates were then inferred from the average elongation rate in each region and the number of mRNA-specific ribosomes, as described previously [72]. Codon optimality for each transcript was calculated according to the codon usage statistics obtained from the Codon Usage Database [222].

Enrichment calculation for centrosomes at the specific cell cycle phase, stress granules, and autophagosomes

mRNAs with read counts ≥10 in both APEX-Ribo-Seq replicates of G1 phase CEP192-pulldown (for centrosomes, 10311 mRNAs), G3BP1-pulldown (for stress granules, 13500 mRNAs), or LC3-pulldown (for autophagosomes, 10635 mRNAs) were selected for downstream analyses. For centrosomes at each cell cycle phase, enrichment calculation was performed by comparing the counts in the pulldown for each cell cycle phase against that of the cytosol, normalized according to input samples of asynchronous cells (both cytosol and centrosomes), *i.e.*, $\log_2$[(CEP192 pulldown/input)/(NES pulldown/input)] (Figure S7G). For stress granules and autophagosomes, comparisons between each count in the pulldown under stressed conditions and that of the control, normalized by input, *i.e.*, $\log_2$[(pulldown in the stressed condition/input)/(pulldown in the control condition/input)] (Figure S8F), were conducted. The definition of a positive list for local translation was the same as that described in the "*Enrichment calculation for 14 organelle compartments*" ($\log_2$ fold enrichment > 0.503 and adjusted P value < 0.05).

Enrichment calculation for neuronal compartments

mRNAs with read counts ≥ 1 in both APEX-Ribo-Seq replicates of Nefl-pulldown, Map2-pulldown, or Snca-pulldown (14766 genes in total) were selected for downstream analyses. The enrichment was calculated as pulldown samples normalized by each input, *i.e.*, target pulldown/input. mRNAs with $\log_2$ fold enrichment > 0 and adjusted *P* value < 0.05 were defined as locally translated genes.

The following neuron-specific transcriptome and translatome datasets were compared with our data: RNA-Seq data from microdissected neuropils [180], Ribo-Seq data from microdissected neuropils [52], TRAP-Seq data from CA1 neuropils [181], and dendritic PL-Ribo-Seq data [62].

Data availability

The Ribo-Seq, APEX-Ribo-Seq, RNA-Seq, and APEX-RNA-Seq data obtained in this study (GSE297505) [https://www.ncbi.nlm.nih.gov/geo/query/acc.cgi?acc=GSE297505] were deposited in the National Center for Biotechnology Information (NCBI) database.

This study also used previously deposited Ribo-Seq and RNA-Seq data (GSE233555) [https://www.ncbi.nlm.nih.gov/geo/query/acc.cgi?acc=GSE233555] [72].

Code availability

Custom scripts for the mapping and quantification for ribosome profiling are available at https://github.com/ingolia-lab/RiboSeq. The other key custom scripts used in this study

are available at Zenodo (DOI: 10.5281/zenodo.15484640) [https://zenodo.org/records/15484640].

Figure and Table Legends

Figure 1. Benchmarking of APEX-Ribo-Seq.

(A) Schematic of APEX-Ribo-Seq and APEX-RNA-Seq.

(B) Scatter plot of the ribosome footprints from each mRNA in standard Ribo-Seq (input) and cytosol APEX-Ribo-Seq. mRNAs encoded in the mitochondrial genome are highlighted.

(C) Scatter plot of the ribosome footprints from each mRNA in cytosol APEX-Ribo-Seq and matrix APEX-Ribo-Seq. mRNAs encoded in the mitochondrial genome are highlighted.

(D-E) Volcano plots showing organelle enrichment determined by APEX-Ribo-Seq (Figure S2E). mRNAs with an adjusted *P* value of 0.05 or lower are shown. The colored areas represent mRNAs that met the fold change threshold defined by ROC analysis (Figure S2F). On top, histograms for the indicated groups of mRNAs depicted within the volcano plots are shown.

(F) Fraction of mRNAs locally translated on the OMM among all mitochondria-targeting proteins (defined by MitoCarta 3.0) [95].

(G) Box plots of the ORF length for the indicated groups of mRNAs.

TPM, transcripts per million; *r*, Pearson's correlation coefficient.

Box plots show the median (centerline), upper/lower quartiles (box limits), and 1.5× interquartile range (whiskers).

See also Figures S1-2 and Table S1.

Figure 2. Local translation atlas for 14 subcellular compartments.

(A) t-SNE plot [223] for mRNAs locally translated at at least one site in 14 organelles (Figure S3G) according to organelle enrichment determined by APEX-Ribo-Seq (Figure S2E). The gray groups are described in the main text.

(B) Fraction of overlap among locations where the mRNA is classified as undergoing local translation by APEX-Ribo-Seq.

(C) Heatmap of organelle enrichment determined by APEX-Ribo-Seq (Figure S2E) for mRNAs classified at a unique locus. The color scale indicates the degree of organelle enrichment.

(D) Heatmap of the correspondence of locally translated mRNAs and the localization of proteins encoded in the mRNAs. Protein localization is defined by BioID-based proximity labeling [97]. The *Z* score represents the standardized enrichment or depletion of the localization term within the local translation category. The color scale indicates the *Z* score. The black box tiles are described in the main text.

(E and G) Heatmaps of organelle enrichment determined by APEX-Ribo-Seq (Figure S2E) for the indicated mRNAs. The color scale indicates the degree of organelle enrichment.

(F) The number of membrane-inserted or membrane-translocated proteins (see Methods for details) for each local translation category.

See also Figures S3-4 and Table S1.

Figure 3. Local translational control beyond RNA localization.

(A) Bar plots of the Pearson's correlation coefficients between organelle enrichment determined by APEX-Ribo-Seq and that by APEX-RNA-Seq (Figure S2E).

(B) Scatter plots of organelle enrichment determined by APEX-Ribo-Seq and APEX-RNA-Seq (Figure S2E) at the indicated loci.

(C) Heatmap of the enrichment of eCLIP-Seq reads within the 5′ UTR, ORF, and 3′ UTR for the indicated group of mRNAs. The top five RBPs ($\log_2$ eCLIP-Seq enrichment > 0 and P value < 0.01), ranked by P value, were visualized. All the results are summarized in Table S8. The color scale indicates the degree of the eCLIP-Seq read enrichment.

r, Pearson's correlation coefficient.

See also Figure S5 and Table S1.

Figure 4. Prediction of local translation via language model.

(A) Occurrence of short motifs (5-7 mer) that are enriched in the mRNAs with high organelle enrichment according to APEX-Ribo-Seq.

(B) Pearson's correlation between machine-learning predicted and actual organelle enrichment determined by APEX-Ribo-Seq on the test set. The linear regression and random forest models included only the lengths of the 5′ UTR, ORF, and 5′ UTR as inputs. ResCNN, ResNet using one-hot encoded sequences; RiNALMO-Full/ORF/5′ UTR/3′ UTR, feed-forward network (FNN) applied to mean-pooled RiNALMO embeddings from the specified sequence region (full mRNA sequence, ORF, 5′ UTR, or 3′ UTR); TransLocAttn, FNN applied to attention-weighted mean-pooled RiNALMO embeddings. See Methods for model details.

(C-E) Examples of attention weights from TransLocAttn (top) and eCLIP-Seq read distributions (bottom) along the indicated mRNAs. eCLIP-Seq datasets with high correlation with the attention weights are shown in color; all other eCLIP-Seq datasets (*i.e.*, those that did not meet the threshold) are shown in gray.

(F-H) Box plots of changes in Ribo-Seq and RNA-Seq after siRNA-mediated knockdown of *LAPR4* (F), *AKAP1* (G), and *IGF2BP1* (H) in the indicated mRNA groups. *P* values were calculated with the Mann–Whitney *U* test (two-tailed).

Box plots show the median (centerline), upper/lower quartiles (box limits), and 1.5× interquartile range (whiskers).

See also Figure S6 and Table S2.

Figure 5. Slow translation kinetics on the ERM and OMM.

(A) Box plots of calibrated ribosome number per 100 codons [72] across mRNAs locally translated at the indicated loci.

(B-C) Regression line between chase time and the ribosome-free region downstream of the start codon in the harringtonine-mediated ribosome run-off assay [72]. The slope represents the translation elongation rate. Errors represent a 95% confidence interval of the fit. *P* values were assessed by two-tailed *Z* test using the means and standard errors for each group.

(D-E) Box plots showing the translation initiation rates (D) and codon optimality [222] (E) for the indicated mRNA groups. *P* values were calculated with the Mann–Whitney *U* test (two-tailed).

Box plots show the median (centerline), upper/lower quartiles (box limits), and 1.5× interquartile range (whiskers).

See also Figure S6.

Figure 6. Local translation is regulated by internal and external cues.

(A) Heatmap of cell cycle phase-dependent centrosome enrichment determined by APEX-Ribo-Seq (Figure S7G). The color scale indicates the degree of phase-dependent centrosome enrichment.

(B) Fraction of overlap among phases for mRNAs classified as undergoing local translation at the centrosome by APEX-Ribo-Seq.

(C) Heatmaps of phase-dependent centrosome enrichment determined by APEX-Ribo-Seq (Figure S7G) for the indicated mRNAs. The color scale indicates the degree of phase-dependent centrosome enrichment. The results of smFISH analysis of the indicated mRNAs [22] are shown.

(D) Bar plots of the Pearson's correlation coefficients between phase-dependent centrosome enrichment determined by APEX-Ribo-Seq and that determined by APEX-RNA-Seq (Figure S7G).

(E) Heatmap of the enrichment of eCLIP-Seq reads within the 5′ UTR, ORF, and 3′ UTR for the indicated group of mRNAs. The results of the 5 RBPs with the highest read enrichment (mean $\log_2$ eCLIP-Seq enrichment > 0 and *P* value < 0.01) are shown for each group of mRNAs. The color scale indicates the degree of eCLIP-Seq read enrichment. A complete list of significant RBPs is provided in Table S8.

(F) Box plots of changes in translation efficiency in *EIF4G2* knockout cells [154], as measured by Ribo-Seq and RNA-Seq. *P* values were calculated with the Mann–Whitney *U* test (two-tailed).

(G-H) Volcano plots showing stress-dependent enrichment of G3BP1/stress granules (Figure S8F) determined by APEX-Ribo-Seq (G) and that by APEX-RNA-Seq (H). mRNAs with an adjusted *P* value of 0.05 or lower are shown. The colored areas represent mRNAs that met the fold change threshold defined by ROC analysis (Figure S2F).

(I) Scatter plot of stress-dependent enrichment of G3BP1/stress granules by APEX-Ribo-Seq and that by APEX-RNA-Seq (Figure S8F). Localized or locally translated mRNAs defined by APEX-RNA-Seq and APEX-Ribo-Seq are highlighted.

(J) Volcano plot showing stress-dependent enrichment of LC3B/autophagosomes (Figure S8F) determined by APEX-Ribo-Seq. mRNAs with an adjusted *P* value of 0.05 or lower are shown. The colored areas represent mRNAs that met the fold change threshold defined by ROC analysis (Figure S2F).

(K) Complexes encoded by mRNAs localized on autophagosomes as ribosome–mRNA complexes were assessed by STRING analysis [107]. The results of the top 15 terms, ranked by false discovery rate (FDR) value, are visualized. The terms shown in color are described in the main text. The color scale indicates the strength of the associations in the network (ranging from 0 to 1), which is a confidence indicator [107].

(L) Box plots of the net charge of the N-terminal 100 amino acids (aa) of proteins encoded in the indicated mRNA groups.

r, Pearson's correlation coefficient.

Box plots show the median (centerline), upper/lower quartiles (box limits), and 1.5× interquartile range (whiskers).

See also Figures S7-9 and Table S3.

Figure 7. Local translation profiling of neuronal compartments.

(A) Volcano plots showing neuronal compartment enrichment (Figure S10F) for dendrites, axons, and presynapses determined by APEX-Ribo-Seq. mRNAs with an adjusted *P* value of 0.05 or lower are shown. The colored areas represent enriched mRNAs.

(B) Heatmap of neuronal compartment enrichment determined by APEX-Ribo-Seq (Figure S10F) for the indicated neuronal compartments. The color scale indicates the degree of neuronal compartment enrichment.

(C) Fraction of overlap among locations where the mRNA is classified as undergoing local translation by APEX-Ribo-Seq.

(D) Venn diagram of locally translated mRNAs in the indicated neuronal compartments.

(E) Scatter plots of neuronal compartment enrichment as determined by APEX-Ribo-Seq and APEX-RNA-Seq (Figure S10F). Localized or locally translated mRNAs defined by APEX-RNA-Seq and APEX-Ribo-Seq are highlighted.

(F) Fraction of overlap among locations where the mRNA is classified as undergoing local translation by APEX-RNA-Seq.

(G) A Venn diagram of localized mRNAs in the indicated neuronal compartments

(H) Box plots of the lengths of the 5′ UTR, ORF, and 3′ UTR of the indicated mRNA groups defined by APEX-Ribo-Seq. *P* values were calculated with the Mann–Whitney *U* test (two-tailed).

(I) Complexes encoded in locally translated mRNAs in the indicated neuronal compartments were assessed by STRING analysis [107]. The results of the top 10 terms, ranked by false discovery rate (FDR) value, after removing clusters present in more than three compartments, are shown. Terms shown in color are described in the main text. The color scale indicates the strength of the associations in the network (ranging from 0 to 1), which is a confidence indicator [107].

r, Pearson's correlation coefficient.

Box plots show the median (centerline), upper/lower quartiles (box limits), and 1.5× interquartile range (whiskers).

See also Figure S10 and Table S4.

Figure S1. Optimization of the APEX-Ribo-Seq protocol, related to Figure 1.

(A) Schematics of constructs for APEX2 fusion protein expression.

(B) Immunofluorescence analysis of the indicated proteins (detected by EGFP) and desthiobiotinylated proteins/RNAs (detected with Alexa Fluor 555-conjugated streptavidin). DAPI (4',6-diamidino-2-phenylindole) was used to stain the DNA. The scale bar represents 10 μm.

(C) Western blotting and RNA dot blotting for proteins and RNAs under the indicated conditions. Desthiobiotinylated proteins and RNAs were detected using infrared dye-conjugated streptavidin. As a loading control, RPS17 protein was subjected to Western blotting, and total RNA was stained with methylene blue.

(D) Polysome profiling under the indicated conditions.

(E) Western blotting and RNA dot blotting for proteins and RNAs along the fractions of polysome profiling (see D for the corresponding fraction numbers). Desthiobiotinylated proteins and RNAs were detected by infrared dye-conjugated streptavidin. Total RNA was stained with methylene blue.

(F) Scatter plot of the ribosome footprints from each mRNA in standard Ribo-Seq. The results in the presence and absence of H_2O_2 were compared.

(G) SYPRO Ruby staining of proteins purified after streptavidin pulldown and elution under the indicated conditions.

(H) Fractions of usable reads (reads after deduplication and removal of noncoding RNA-mapped reads) in standard Ribo-Seq and cytosol APEX-Ribo-Seq under the indicated conditions.

(I) Distribution of ribosome footprint length under the indicated conditions.

(J) Metagene plots of ribosome footprints (the 5′-end positions) around the start codon under the indicated conditions. The data for the 29-nt footprints are shown.

(K) Fraction of the frame position for the 5′ end of the footprint (29 nt) under the indicated conditions.

(L) Scatter plot of the ribosome footprints from each mRNA in cytosol APEX-Ribo-Seq replicates.

(M) Immunofluorescence analysis of the indicated proteins (detected by V5) and desthiobiotinylated proteins/RNAs (detected with Alexa Fluor 555-conjugated streptavidin). TOM20 was detected as a mitochondrial marker. The scale bar represents 10 μm.

(N) Fraction of the frame position for the 5′ end of the mitoribosome footprint (32 nt) in matrix APEX-Ribo-Seq.

TPM, transcripts per million; *r*, Pearson's correlation coefficient; RPM, reads per million reads.

For H, K, and N, the means (bars), s.d.s (errors), and individual replicates (n = 2, points) are shown.

Figure S2. Characterization of ERM and OMM APEX-Ribo-Seq data, related to Figure 1.

(A) Immunofluorescence analysis of the indicated proteins (detected by V5) with desthiobiotinylated proteins/RNAs (detected with Alexa Fluor 555-conjugated streptavidin). CANX was detected as a marker of the ER. The scale bar represents 10 μm.

(B) Distribution of ribosome footprint length under the indicated conditions.

(C) Metagene plots of ribosome footprints (the 5′-end positions) around the start codon under the indicated conditions. The data for the 29-nt footprints are shown.

(D) Fraction of the frame position for the 5′ end of the footprint (29 nt) under the indicated conditions.

(E) Schematics of the organelle enrichment calculation.

(F) ROC curve to determine the fold change threshold for organelle enrichment.

(G) Cumulative distributions of ERM enrichment in APEX-Ribo-Seq with respect to the mRNAs found in the secretome (see Methods for details) and by Frac-Seq [89], APEX-RIP [65], and APEX-RNA-Seq [63] targeting the ERM. *P* values were calculated with the Mann–Whitney *U* test (two-tailed).

(H) Immunofluorescence analysis of the indicated proteins (detected by V5) with smiFISH for the indicated mRNAs. DAPI was used to stain the DNA. An enlarged view of the region indicated by the dashed square is shown. The scale bar represents 10 μm.

(I) Quantification of the data shown in H. The colocalization rates of the marker proteins and the indicated RNAs are shown. Nuclear *NEAT1* lncRNA was detected and analyzed as a negative control. The median (bars) and individual data (points, n for the number of cells analyzed) are shown. *P* values were calculated with the Mann–Whitney *U* test (two-tailed).

(J) Immunofluorescence analysis of the indicated proteins (detected by V5) with desthiobiotinylated proteins/RNAs (detected with Alexa Fluor 555-conjugated streptavidin). TOM20 was detected as a mitochondrial marker. The scale bar represents 10 μm.

(K) Distribution of ribosome footprint length under the indicated conditions.

(L) Fraction of the frame position for the 5′ end of the footprint (29 nt) under the indicated conditions. The means (bars), s.d.s (errors), and individual replicates (n = 2, points) are shown.

(M) Cumulative distributions of OMM enrichment in APEX-Ribo-Seq with respect to the mRNAs found in APEX-RNA-Seq [63] targeting the OMM. *P* values were calculated with the Mann–Whitney *U* test (two-tailed).

(N) Box plots of matrix and OMM enrichment (E) determined via APEX-Ribo-Seq for mitochondrial genome-encoded mRNAs (left) and mRNAs locally translated on the OMM (defined in Figure 1E). *P* values were calculated with the Mann–Whitney *U* test (two-tailed).

RPM, reads per million reads.

For D and L, the means (bars), s.d.s (errors), and individual replicates (n = 2, points) are shown.

Box plots show the median (centerline), upper/lower quartiles (box limits), and 1.5× interquartile range (whiskers).

Figure S3. Characterization of APEX-Ribo-Seq data for 12 loci, related to Figure 2.

(A) Immunofluorescence analysis of the indicated proteins (detected by EGFP or V5) with desthiobiotinylated proteins/RNAs (detected with Alexa Fluor 555-conjugated streptavidin). The following proteins were detected as organelle markers: catalase (peroxisomes), TGN46 (*trans*-Golgi), GM130 (*cis*-Golgi), EEA1 (endosomes), RUFY1 (early endosomes), AP2S1 (clathrin-coated vesicles), GFAP (intermediate filaments), and PCNT (centrosomes). DAPI was used to stain the DNA. LysoTracker was used to stain lysosomes. The scale bar represents 10 μm.

(B) Immunofluorescence analysis of the indicated proteins (detected by V5). PCNT was detected as a centrosomal marker. The white boxes highlight centrosomes with aberrant architecture. The scale bar represents 10 μm.

(C) Distribution of ribosome footprint length under the indicated conditions.

(D) Fraction of the frame position for the 5′ end of the footprint (29 nt) under the indicated conditions. The means (bars), s.d.s (errors), and individual replicates (n = 2, points) are shown.

(E) Heatmap of the Pearson correlation coefficients (*r*) of APEX-Ribo-Seq and input standard Ribo-Seq under the indicated conditions. The value of *r* is indicated by the color scale.

(F) Volcano plots showing organelle enrichment determined by APEX-Ribo-Seq (Figure S2E). mRNAs with an adjusted *P* value of 0.05 or lower are shown. The colored areas represent mRNAs that met the fold change threshold defined by ROC analysis (Figure S2F).

(G) Heatmap of organelle enrichment determined by APEX-Ribo-Seq (Figure S2E) for mRNAs locally translated at least one site in 14 organelles. The color scale indicates the degree of organelle enrichment.

(H, J, L, N, and P) Immunofluorescence analysis of the indicated proteins (detected by V5) with smiFISH for the indicated mRNAs. DAPI was used to stain the DNA. An enlarged view of the region indicated by the dashed square is shown. The scale bar represents 10 μm.

(I, K, M, O, and Q) Quantification of the data shown in H, J, L, N, and P. The colocalization rates of the marker proteins and the indicated RNAs are shown. Nuclear *NEAT1* lncRNA was detected and analyzed as a negative control. The median (bars) and

individual data (points, n for the number of cells analyzed) are shown. *P* values were calculated with the Mann–Whitney *U* test (two-tailed).

(R) Cumulative distributions of translation efficiency changes (measured by standard Ribo-Seq and RNA-Seq) with respect to the mRNAs locally translated on the centrosome (defined in F). *P* values were calculated with the Mann–Whitney *U* test (two-tailed).

Figure S4. Comparative analysis of the local translation atlas with publicly available data, related to Figure 2.

(A) Heatmap of the correspondence of locally translated mRNAs and the localization of proteins encoded in the mRNAs. Protein localization is defined by immunofluorescence microscopy (The Human Protein Atlas) [106]. The *Z* score represents the standardized enrichment or depletion of each localization term within the local translation category. The color scale indicates the *Z* score. The black box tiles are described in the main text.

(B) Complexes encoded by mRNAs locally translated at the indicated organelles were assessed by STRING analysis [107]. The results of the top 10 terms, ranked by false discovery rate (FDR) value, are visualized. The terms shown in color are described in the main text. The color scale indicates the strength of the associations in the network (ranging from 0 to 1), which is a confidence indicator [107].

(C) Heatmap of organelle enrichment determined by APEX-Ribo-Seq (Figure S2E) for the indicated mRNAs. The color scale indicates the degree of organelle enrichment.

(D) Tile plot showing the candidate co-co–assembled pairs [129] in the indicated mRNA groups. Pairs unique to each locus are highlighted.

Figure S5. Characterization of APEX-RNA-Seq data, related to Figure 3.

(A) Schematic of the mechanisms for local translation and the correlation between APEX-Ribo-Seq and APEX-RNA-Seq.

(B) Heatmap of the Pearson correlation coefficients (*r*) of APEX-RNA-Seq and input standard RNA-Seq under the indicated conditions. The value of *r* is indicated by the color scale.

(C) Box plots of relative matrix translation efficiency (matrix APEX-Ribo-Seq normalized by matrix APEX-RNA-Seq) for the indicated mRNA groups. *P* values were calculated with the Mann–Whitney *U* test (two-tailed).

Figure S6. Application of the language model to the local translation atlas, related to Figure 4.

(A) Box plots of calibrated numbers of ribosomes on the ORFs (per 100 codons) [72] translated on the indicated organelles.

(B) Coefficients from linear regression using all data, where the inputs are the lengths of each 5′ UTR, ORF, and 3′ UTR sequence, and the outputs are organelle enrichment determined by APEX-Ribo-Seq ($\log_2$ fold enrichment).

(C) Pearson's correlation between predicted and actual organelle enrichment determined by APEX-Ribo-Seq on the test set, where the models apply FNN to mean-pooled embeddings from the specified sequence region (full mRNA sequence, ORF, 5′ UTR, or 3′ UTR). RiNALMo, using embeddings generated by RiNALMo; AIDO.RNA, using embeddings generated by AIDO.RNA; Evo 2, using embeddings generated by Evo 2.

(D) Architecture of the TransLocAttn model. See Methods for details.

(E-F) Examples of attention weights from TransLocAttn (top) and eCLIP-Seq read distributions (bottom) along the indicated mRNAs. eCLIP-Seq data with high correlation

with the attention weights are shown with color-highlighted lines, and all other eCLIP-Seq datasets that do not pass the threshold are shown in gray.

(G) Histogram of the tail dependence score, which quantifies the co-occurrence of high-signal regions (signal_frac=0.05) between the attention weight tracks and eCLIP-Seq map. The score is normalized by signal_frac^2=0.0025 so that if the two datasets are completely random, the expected score is 1. Blue represents the actual data, and orange represents the random shift control.

(H) Histogram of the Spearman's correlation coefficients between the attention weight tracks and eCLIP-Seq map. Blue represents the actual data, and orange represents the random shift control.

(I) Scatter plot of the tail dependence score and Spearman's correlation coefficients. Each dot represents an attention weight–eCLIP-Seq mapping pair. Blue represents the actual data, and orange represents the random shift control.

(J) Volcano plots showing eCLIP-Seq enrichment on ORFs for mRNAs locally translated on the OMM (defined in Figure 1E). eCLIP-Seq datasets with a *P* value of 0.01 or lower are shown. eCLIP-Seq data for LARP4 and AKAP1 are highlighted.

Box plots show the median (centerline), upper/lower quartiles (box limits), and 1.5× interquartile range (whiskers).

Figure S7. Characterization of the cell cycle phase-dependent regulation of centrosome translation, related to Figure 6.

(A) Histograms of propidium iodide staining of cell cycle phase-synchronized cells.

(B) Immunofluorescence analysis of the indicated proteins (detected by V5) with desthiobiotinylated proteins/RNAs (detected with Alexa Fluor 555-conjugated

streptavidin) in cells synchronized at the indicated cell cycle phases. DAPI was used to stain the DNA. The scale bar represents 10 μm.

(C) Centrosome condensation rate under the indicated conditions. The means (bars, n for the number of cells analyzed) and s.d.s (errors) are shown.

(D) Distribution of ribosome footprint length under the indicated conditions.

(E) Fraction of the frame position for the 5′ end of the footprint (29 nt) under the indicated conditions. The means (bars), s.d.s (errors), and individual replicates (n = 2, points) are shown.

(F) Heatmap of the Pearson correlation coefficients (*r*) of APEX-Ribo-Seq and input standard Ribo-Seq under the indicated conditions. The value of *r* is indicated by the color scale.

(G) Schematic of the phase-dependent centrosome enrichment calculation.

(H) Volcano plots showing phase-dependent centrosome enrichment determined by APEX-Ribo-Seq (G). mRNAs with an adjusted *P* value of 0.05 or lower are shown. The colored areas represent mRNAs that met the fold change threshold defined by ROC analysis (Figure S2F).

(I) Box plots of centrosome enrichment (in asynchronous cells) in APEX-Ribo-Seq for the indicated mRNA groups (defined in H).

(J) Heatmaps of the indicated genes involved in phase-dependent centrosome enrichment determined by APEX-Ribo-Seq (G).

(K) Heatmap of the Pearson correlation coefficients (*r*) of APEX-RNA-Seq and input standard RNA-Seq under the indicated conditions. The value of *r* is indicated by the color scale.

Box plots show the median (centerline), upper/lower quartiles (box limits), and 1.5× interquartile range (whiskers).

Figure S8. Characterization of the local translation on stress granules, related to Figure 6.

(A) Schematics of constructs for APEX2 fusion protein expression.

(B) Immunofluorescence analysis of the indicated proteins (detected by V5) with desthiobiotinylated proteins/RNAs (detected with Alexa Fluor 555-conjugated streptavidin) with or without thapsigargin (Tg, 500 nM for 30 min). DAPI was used to stain the DNA. The scale bar represents 10 μm.

(C) Distribution of ribosome footprint length under the indicated conditions.

(D) Fraction of the frame position for the 5′ end of the footprint (29 nt) under the indicated conditions. The means (bars), s.d.s (errors), and individual replicates (n = 2, points) are shown.

(E) Heatmap of the Pearson correlation coefficients (*r*) of APEX-Ribo-Seq and input standard Ribo-Seq under the indicated conditions. The value of *r* is indicated by the color scale.

(F) Schematics of the stress-dependent enrichment calculation.

(G) Volcano plot showing translation changes caused by Tg treatment in the input standard Ribo-Seq. mRNAs with an adjusted *P* value of 0.05 or lower are shown. mRNAs possessing uORFs [162] are highlighted.

(H) Heatmap of the Pearson correlation coefficients (*r*) of APEX-RNA-Seq and input standard RNA-Seq under the indicated conditions. The value of *r* is indicated by the color scale.

(I) Cumulative distributions of stress granule enrichment in APEX-RNA-Seq with respect to the 5′ TOP mRNAs [166]. *P* values were calculated with the Mann–Whitney *U* test (two-tailed).

(J) Heatmap of the enrichment of eCLIP-Seq reads on the 5′ UTR, ORF, and 3′ UTR for the indicated group of mRNAs. The results of the top 5 RBPs (mean $\log_2$ eCLIP-Seq enrichment > 0 and *P* value < 0.01) for each group of mRNAs are shown. The color scale indicates the degree of eCLIP-Seq read enrichment. A complete list of significant RBPs is provided in Table S8.

Box plots show the median (centerline), upper/lower quartiles (box limits), and 1.5× interquartile range (whiskers).

Figure S9. Characterization of local translation on autophagosomes, related to Figure 6.

(A) Schematics of constructs for APEX2 fusion protein expression.

(B) Immunofluorescence analysis of the indicated proteins (detected by V5) with desthiobiotinylated proteins/RNAs (detected with Alexa Fluor 555-conjugated streptavidin) with or without amino acid depletion (AA dep., for 1 h). DAPI was used to stain the DNA. The scale bar represents 10 μm.

(C) Distribution of ribosome footprint length under the indicated conditions.

(D) Fraction of the frame position for the 5′ end of the footprint (29 nt) under the indicated conditions. The means (bars), s.d.s (errors), and individual replicates (n = 2, points) are shown.

(E) Heatmap of the Pearson correlation coefficients (*r*) of APEX-Ribo-Seq and input standard Ribo-Seq under the indicated conditions. The value of *r* is indicated by the color scale.

(F) Cumulative distributions of translation changes caused by amino acid depletion in the input standard Ribo-Seq with respect to the 5′ TOP mRNAs [166]. *P* values were calculated with the Mann–Whitney *U* test (two-tailed).

(G) Volcano plot showing translation changes caused by amino acid depletion in the input standard Ribo-Seq. mRNAs with an adjusted *P* value of 0.05 or lower are shown. mRNAs possessing uORFs [162] are highlighted.

(H) Heatmap of the Pearson correlation coefficients (*r*) of APEX-RNA-Seq and input standard RNA-Seq under the indicated conditions. The value of *r* is indicated by the color scale.

(I) Volcano plot showing stress-dependent enrichment of LC3B/autophagosomes (Figure S8F) determined by APEX-RNA-Seq. mRNAs with an adjusted *P* value of 0.05 or lower are shown. The colored areas represent mRNAs that met the fold change threshold defined by ROC analysis (Figure S2F).

(J) Scatter plots of autophagosome enrichment determined by APEX-Ribo-Seq and APEX-RNA-Seq (Figure S8F). Localized mRNAs or localized ribosome–mRNA complexes defined by APEX-RNA-Seq and APEX-Ribo-Seq are highlighted.

(K) Tile plot showing the comparison of autophagosome-localized ribosome–mRNA complexes found in APEX-Ribo-Seq with the LC3 secretome [173] and LC3 interactome [174]. Histone proteins and ribosomal proteins are highlighted.

Figure S10. Characterization of local translation in neuronal compartments, related to Figure 7.

(A) Schematics of constructs for APEX2 fusion protein expression.

(B) Immunofluorescence analysis of the indicated proteins (detected by EGFP) with desthiobiotinylated proteins/RNAs (detected with Alexa Fluor 555-conjugated streptavidin) in mouse primary neurons. DAPI was used to stain the DNA. Tubb3 and Syn1 were detected as axon and presynapse markers, respectively. The scale bar represents 10 μm.

(C) Distribution of ribosome footprint length under the indicated conditions.

(D) Fraction of the frame position for the 5′ end of the footprint (29 nt) under the indicated conditions. The means (bars), s.d.s (errors), and individual replicates (n = 2, points) are shown.

(E) Heatmap of the Pearson correlation coefficients (*r*) of APEX-Ribo-Seq and input standard Ribo-Seq under the indicated conditions. The value of *r* is indicated by the color scale.

(F) Schematics of the neuronal compartment enrichment calculation.

(G) GO analysis of cellular components [107] for the indicated mRNA groups. The results of the top 10 terms, ranked by signal score, are visualized. The color-highlighted terms are described in the main text.

(H) Volcano plots same as Figure 7A. On top, histograms for mRNAs defined by RNA-Seq (microdissected neuropil) [180], Ribo-Seq (microdissected neuropil) [52], TRAP-Seq (CA1 neuropil) [181], and PL-Ribo-Seq (dendrite) [62] within the volcano plots are shown.

(I) Fraction of mRNAs defined by dendrite PL-Ribo-Seq [62] among mRNAs translated in the indicated neuronal compartments (defined in Figure 7A).

(J) Heatmap of the Pearson correlation coefficients (*r*) of APEX-RNA-Seq and input standard RNA-Seq under the indicated conditions. The value of *r* is indicated by the color scale.

(K) Volcano plots showing neuronal compartment enrichment (Figure S10F) for dendrites, axons, and presynapses determined by APEX-RNA-Seq. mRNAs with an adjusted *P* value of 0.05 or lower are shown. The colored areas represent enriched mRNAs.

(L) Box plots of the lengths of the 5′ UTR, ORF, and 3′ UTR of the indicated mRNA groups defined by APEX-RNA-Seq. *P* values were calculated with the Mann–Whitney *U* test (two-tailed).

Box plots show the median (centerline), upper/lower quartiles (box limits), and 1.5× interquartile range (whiskers).

Table S1. Log_2 fold enrichment and statistical metrics of APEX-Ribo-Seq and APEX-RNA-Seq in atlas analysis, related to Figures 1, 2, 3, S2, and S3.

Table S2. Summary of HOMER and TransLocAttn analysis, related to Figures 4 and S6.

Table S3. Log_2 fold enrichment and statistical metrics of APEX-Ribo-Seq and APEX-RNA-Seq at the specific cell cycle phase, stress granules, and autophagosomes, related to Figures 6, S7, S8, and S9.

Table S4. Log_2 fold enrichment and statistical metrics of APEX-Ribo-Seq and APEX-RNA-Seq at neuronal compartments, related to Figures 7 and S10.

Table S5. Library information of APEX-Ribo-Seq and APEX-RNA-Seq, related to all Figures.

Table S6. Antibody list, related to Figures S1, S2, S3, S7, S8, S9, and S10.

Table S7. Sequence of smiFISH probes and organelle mask parameters, related to Figures S2 and S3.

Table S8. Comparison of eCLIP-Seq with APEX-Ribo-Seq and APEX-RNA-Seq, related to Figures 3, 6, and S8.

References

1. Bourke, A.M., Schwarz, A., and Schuman, E.M. (2023). De-centralizing the Central Dogma: mRNA translation in space and time. Mol. Cell *83*, 452–468.

2. Das, S., Vera, M., Gandin, V., Singer, R.H., and Tutucci, E. (2021). Intracellular mRNA transport and localized translation. Nat. Rev. Mol. Cell Biol. *22*, 483–504.

3. Gamerdinger, M., and Deuerling, E. (2024). Cotranslational sorting and processing of newly synthesized proteins in eukaryotes. Trends Biochem. Sci. *49*, 105–118.

4. Gemmer, M., and Förster, F. (2020). A clearer picture of the ER translocon complex. J. Cell Sci. *133*, jcs231340.

5. Lautier, O., Penzo, A., Rouvière, J.O., Chevreux, G., Collet, L., Loïodice, I., Taddei, A., Devaux, F., Collart, M.A., and Palancade, B. (2021). Co-translational assembly and localized translation of nucleoporins in nuclear pore complex biogenesis. Mol. Cell *81*, 2417–2427.e5.

6. Liao, G., Mingle, L., Van De Water, L., and Liu, G. (2015). Control of cell migration through mRNA localization and local translation. Wiley Interdiscip. Rev. RNA *6*, 1–15.

7. Trcek, T., and Lehmann, R. (2019). Germ granules in *Drosophila*. Traffic *20*, 650–660.

8. Parker, D.M., Winkenbach, L.P., Boyson, S., Saxton, M.N., Daidone, C., Al-Mazaydeh, Z.A., Nishimura, M.T., Mueller, F., and Osborne Nishimura, E. (2020). mRNA localization is linked to translation regulation in the *Caenorhabditis elegans*

germ lineage. Development *147*, dev186817.

9. Dufourt, J., Bellec, M., Trullo, A., Dejean, M., De Rossi, S., Favard, C., and Lagha, M. (2021). Imaging translation dynamics in live embryos reveals spatial heterogeneities. Science *372*, 840–844.

10. Chen, R., Stainier, W., Dufourt, J., Lagha, M., and Lehmann, R. (2024). Direct observation of translational activation by a ribonucleoprotein granule. Nat. Cell Biol. *26*, 1322–1335.

11. Holt, C.E., Martin, K.C., and Schuman, E.M. (2019). Local translation in neurons: visualization and function. Nat. Struct. Mol. Biol. *26*, 557–566.

12. Cioni, J.-M., Koppers, M., and Holt, C.E. (2018). Molecular control of local translation in axon development and maintenance. Curr. Opin. Neurobiol. *51*, 86–94.

13. Lesnik, C., Golani-Armon, A., and Arava, Y. (2015). Localized translation near the mitochondrial outer membrane: An update. RNA Biol. *12*, 801–809.

14. De Pace, R., Ghosh, S., Ryan, V.H., Sohn, M., Jarnik, M., Rezvan Sangsari, P., Morgan, N.Y., Dale, R.K., Ward, M.E., and Bonifacino, J.S. (2024). Messenger RNA transport on lysosomal vesicles maintains axonal mitochondrial homeostasis and prevents axonal degeneration. Nat. Neurosci. *27*, 1087–1102.

15. Baumann, S., König, J., Koepke, J., and Feldbrügge, M. (2014). Endosomal transport of septin mRNA and protein indicates local translation on endosomes and is required for correct septin filamentation. EMBO Rep. *15*, 94–102.

16. Liao, Y.-C., Fernandopulle, M.S., Wang, G., Choi, H., Hao, L., Drerup, C.M., Patel, R., Qamar, S., Nixon-Abell, J., Shen, Y., et al. (2019). RNA granules hitchhike on lysosomes for long-distance transport, using annexin A11 as a molecular tether. Cell *179*, 147–164.e20.

17. Popovic, D., Nijenhuis, W., Kapitein, L.C., and Pelkmans, L. (2020). Co-translational targeting of transcripts to endosomes. bioRxiv, 2020.07.17.208652. https://doi.org/10.1101/2020.07.17.208652.

18. Cioni, J.-M., Lin, J.Q., Holtermann, A.V., Koppers, M., Jakobs, M.A.H., Azizi, A., Turner-Bridger, B., Shigeoka, T., Franze, K., Harris, W.A., et al. (2019). Late endosomes act as mRNA translation platforms and sustain mitochondria in axons. Cell *176*, 56–72.e15.

19. Chouaib, R., Safieddine, A., Pichon, X., Imbert, A., Kwon, O.S., Samacoits, A., Traboulsi, A.-M., Robert, M.-C., Tsanov, N., Coleno, E., et al. (2020). A dual protein-mRNA localization screen reveals compartmentalized translation and widespread co-translational RNA targeting. Dev. Cell *54*, 773–791.e5.

20. Hampoelz, B., Schwarz, A., Ronchi, P., Bragulat-Teixidor, H., Tischer, C., Gaspar, I., Ephrussi, A., Schwab, Y., and Beck, M. (2019). Nuclear pores assemble from Nucleoporin condensates during oogenesis. Cell *179*, 671–686.e17.

21. Dahan, N., Bykov, Y.S., Boydston, E.A., Fadel, A., Gazi, Z., Hochberg-Laufer, H., Martenson, J., Denic, V., Shav-Tal, Y., Weissman, J.S., et al. (2022). Peroxisome function relies on organelle-associated mRNA translation. Sci. Adv. *8*, eabk2141.

22. Safieddine, A., Coleno, E., Salloum, S., Imbert, A., Traboulsi, A.-M., Kwon, O.S., Lionneton, F., Georget, V., Robert, M.-C., Gostan, T., et al. (2021). A choreography of centrosomal mRNAs reveals a conserved localization mechanism involving active polysome transport. Nat. Commun. *12*, 1352.

23. Lerit, D.A. (2022). Signed, sealed, and delivered: RNA localization and translation at centrosomes. Mol. Biol. Cell *33*. https://doi.org/10.1091/mbc.E21-03-0128.

24. Eliscovich, C., Peset, I., Vernos, I., and Méndez, R. (2008). Spindle-localized CPE-mediated translation controls meiotic chromosome segregation. Nat. Cell Biol. *10*, 858–865.

25. Sepulveda, G., Antkowiak, M., Brust-Mascher, I., Mahe, K., Ou, T., Castro, N.M., Christensen, L.N., Cheung, L., Jiang, X., Yoon, D., et al. (2018). Co-translational protein targeting facilitates centrosomal recruitment of PCNT during centrosome maturation in vertebrates. Elife *7*. https://doi.org/10.7554/eLife.34959.

26. Bergalet, J., Patel, D., Legendre, F., Lapointe, C., Benoit Bouvrette, L.P., Chin, A., Blanchette, M., Kwon, E., and Lécuyer, E. (2020). Inter-dependent centrosomal co-localization of the *cen* and *ik2 cis*-natural antisense mRNAs in *Drosophila*. Cell Rep. *30*, 3339–3352.e6.

27. Pascual, R., Segura-Morales, C., Omerzu, M., Bellora, N., Belloc, E., Castellazzi, C.L., Reina, O., Eyras, E., Maurice, M.M., Millanes-Romero, A., et al. (2020). mRNA spindle localization and mitotic translational regulation by CPEB1 and CPEB4. RNA *27*, 291–302.

28. Blower, M.D., Feric, E., Weis, K., and Heald, R. (2007). Genome-wide analysis demonstrates conserved localization of messenger RNAs to mitotic microtubules. J. Cell Biol. *179*, 1365–1373.

29. Fingerhut, J.M., and Yamashita, Y.M. (2020). mRNA localization mediates maturation of cytoplasmic cilia in *Drosophila* spermatogenesis. J. Cell Biol. *219*. https://doi.org/10.1083/jcb.202003084.

30. Hao, K., Chen, Y., Yan, X., and Zhu, X. (2021). Cilia locally synthesize proteins to sustain their ultrastructure and functions. Nat. Commun. *12*, 6971.

31. Liu, H., Li, H., Jiang, Z., Jin, S., Song, R., Yang, Y., Li, J., Huang, J., Zhang, X., Dong, X., et al. (2023). A local translation program regulates centriole amplification in the airway epithelium. Sci. Rep. *13*, 7090.

32. Park, S., Dahn, R., Kurt, E., Presle, A., VanDenHeuvel, K., Moravec, C., Jambhekar, A., Olukoga, O., Shepherd, J., Echard, A., et al. (2023). The mammalian midbody and midbody remnant are assembly sites for RNA and localized translation. Dev. Cell *58*, 1917–1932.e6.

33. Farmer, T., Vaeth, K.F., Han, K.-J., Goering, R., Taliaferro, M.J., and Prekeris, R. (2023). The role of midbody-associated mRNAs in regulating abscission. J. Cell Biol. *222*. https://doi.org/10.1083/jcb.202306123.

34. Mardakheh, F.K., Paul, A., Kümper, S., Sadok, A., Paterson, H., Mccarthy, A., Yuan, Y., and Marshall, C.J. (2015). Global analysis of mRNA, translation, and protein localization: Local translation is a key regulator of cell protrusions. Dev.

Cell *35*, 344–357.

35. Moissoglu, K., Yasuda, K., Wang, T., Chrisafis, G., and Mili, S. (2019). Translational regulation of protrusion-localized RNAs involves silencing and clustering after transport. Elife *8*. https://doi.org/10.7554/eLife.44752.

36. Mili, S., Moissoglu, K., and Macara, I.G. (2008). Genome-wide screen reveals APC-associated RNAs enriched in cell protrusions. Nature *453*, 115–119.

37. Dermit, M., Dodel, M., Lee, F.C.Y., Azman, M.S., Schwenzer, H., Jones, J.L., Blagden, S.P., Ule, J., and Mardakheh, F.K. (2020). Subcellular mRNA localization regulates ribosome biogenesis in migrating cells. Dev. Cell *55*, 298–313.e10.

38. Mateju, D., Eichenberger, B., Voigt, F., Eglinger, J., Roth, G., and Chao, J.A. (2020). Single-molecule imaging reveals translation of mRNAs localized to stress granules. Cell *183*, 1801–1812.e13.

39. Moon, S.L., Morisaki, T., Khong, A., Lyon, K., Parker, R., and Stasevich, T.J. (2019). Multicolour single-molecule tracking of mRNA interactions with RNP granules. Nat. Cell Biol. *21*, 162–168.

40. Wilbertz, J.H., Voigt, F., Horvathova, I., Roth, G., Zhan, Y., and Chao, J.A. (2019). Single-molecule imaging of mRNA localization and regulation during the integrated stress response. Mol. Cell *73*, 946–958.e7.

41. Ramat, A., Haidar, A., Garret, C., and Simonelig, M. (2024). Spatial organization of translation and translational repression in two phases of germ granules. Nat.

Commun. *15*, 8020.

42. Yasuda, K., Zhang, H., Loiselle, D., Haystead, T., Macara, I.G., and Mili, S. (2013). The RNA-binding protein Fus directs translation of localized mRNAs in APC-RNP granules. J. Cell Biol. *203*, 737–746.

43. Zhao, R., Huang, S., Li, J., Gu, A., Fu, M., Hua, W., Mao, Y., Lei, Q.-Y., Lu, B., and Wen, W. (2024). Excessive STAU1 condensate drives mTOR translation and autophagy dysfunction in neurodegeneration. J. Cell Biol. *223*. https://doi.org/10.1083/jcb.202311127.

44. Zhuang, Y., Li, Z., Xiong, S., Sun, C., Li, B., Wu, S.A., Lyu, J., Shi, X., Yang, L., Chen, Y., et al. (2023). Circadian clocks are modulated by compartmentalized oscillating translation. Cell *186*, 3245–3260.e23.

45. Buxbaum, A.R., Wu, B., and Singer, R.H. (2014). Single β-actin mRNA detection in neurons reveals a mechanism for regulating its translatability. Science *343*, 419–422.

46. Wang, C., Han, B., Zhou, R., and Zhuang, X. (2016). Real-Time Imaging of Translation on Single mRNA Transcripts in Live Cells. Cell *165*, 990–1001.

47. Yan, X., Hoek, T.A., Vale, R.D., and Tanenbaum, M.E. (2016). Dynamics of Translation of Single mRNA Molecules In Vivo. Cell *165*, 976–989.

48. Wu, B., Eliscovich, C., Yoon, Y.J., and Singer, R.H. (2016). Translation dynamics of single mRNAs in live cells and neurons. Science *352*, 1430–1435.

49. Morisaki, T., Lyon, K., DeLuca, K.F., DeLuca, J.G., English, B.P., Zhang, Z.,

Lavis, L.D., Grimm, J.B., Viswanathan, S., Looger, L.L., et al. (2016). Real-time quantification of single RNA translation dynamics in living cells. Science *352*, 1425–1429.

50. Zeng, H., Huang, J., Ren, J., Wang, C.K., Tang, Z., Zhou, H., Zhou, Y., Shi, H., Aditham, A., Sui, X., et al. (2023). Spatially resolved single-cell translatomics at molecular resolution. Science *380*, eadd3067.

51. Ingolia, N.T., Ghaemmaghami, S., Newman, J.R.S., and Weissman, J.S. (2009). Genome-wide analysis in vivo of translation with nucleotide resolution using ribosome profiling. Science *324*, 218–223.

52. Glock, C., Biever, A., Tushev, G., Nassim-Assir, B., Kao, A., Bartnik, I., Tom Dieck, S., and Schuman, E.M. (2021). The translatome of neuronal cell bodies, dendrites, and axons. Proc. Natl. Acad. Sci. U. S. A. *118*, e2113929118.

53. Biever, A., Glock, C., Tushev, G., Ciirdaeva, E., Dalmay, T., Langer, J.D., and Schuman, E.M. (2020). Monosomes actively translate synaptic mRNAs in neuronal processes. Science *367*. https://doi.org/10.1126/science.aay4991.

54. Moor, A.E., Golan, M., Massasa, E.E., Lemze, D., Weizman, T., Shenhav, R., Baydatch, S., Mizrahi, O., Winkler, R., Golani, O., et al. (2017). Global mRNA polarization regulates translation efficiency in the intestinal epithelium. Science *357*, 1299–1303.

55. Reid, D.W., and Nicchitta, C.V. (2012). Primary role for endoplasmic reticulum-bound ribosomes in cellular translation identified by ribosome profiling. J. Biol.

Chem. *287*, 5518–5527.

56. Simbriger, K., Amorim, I.S., Chalkiadaki, K., Lach, G., Jafarnejad, S.M., Khoutorsky, A., and Gkogkas, C.G. (2020). Monitoring translation in synaptic fractions using a ribosome profiling strategy. J. Neurosci. Methods *329*, 108456.

57. Jan, C.H., Williams, C.C., and Weissman, J.S. (2014). Principles of ER cotranslational translocation revealed by proximity-specific ribosome profiling. Science *346*, 1257521.

58. Costa, E.A., Subramanian, K., Nunnari, J., and Weissman, J.S. (2018). Defining the physiological role of SRP in protein-targeting efficiency and specificity. Science *359*, 689–692.

59. Shurtleff, M.J., Itzhak, D.N., Hussmann, J.A., Schirle Oakdale, N.T., Costa, E.A., Jonikas, M., Weibezahn, J., Popova, K.D., Jan, C.H., Sinitcyn, P., et al. (2018). The ER membrane protein complex interacts cotranslationally to enable biogenesis of multipass membrane proteins. Elife *7*. https://doi.org/10.7554/eLife.37018.

60. Williams, C.C., Jan, C.H., and Weissman, J.S. (2014). Targeting and plasticity of mitochondrial proteins revealed by proximity-specific ribosome profiling. Science *346*, 748–751.

61. Zhang, Z., Xu, A., Bai, Y., Chen, Y., Cates, K., Kerr, C., Bermudez, A., Susanto, T.T., Wysong, K., García Marqués, F.J., et al. (2025). A subcellular map of translational machinery composition and regulation at the single-molecule level. Science *387*, eadn2623.

62. Hacisuleyman, E., Hale, C.R., Noble, N., Luo, J.-D., Fak, J.J., Saito, M., Chen, J., Weissman, J.S., and Darnell, R.B. (2024). Neuronal activity rapidly reprograms dendritic translation via eIF4G2:uORF binding. Nat. Neurosci. *27*, 822–835.

63. Fazal, F.M., Han, S., Parker, K.R., Kaewsapsak, P., Xu, J., Boettiger, A.N., Chang, H.Y., and Ting, A.Y. (2019). Atlas of Subcellular RNA Localization Revealed by APEX-Seq. Cell *178*, 473–490.e26.

64. Padrón, A., Iwasaki, S., and Ingolia, N.T. (2019). Proximity RNA Labeling by APEX-Seq Reveals the Organization of Translation Initiation Complexes and Repressive RNA Granules. Mol. Cell *75*, 875–887.e5.

65. Kaewsapsak, P., Shechner, D.M., Mallard, W., Rinn, J.L., and Ting, A.Y. (2017). Live-cell mapping of organelle-associated RNAs via proximity biotinylation combined with protein-RNA crosslinking. Elife *6*. https://doi.org/10.7554/eLife.29224.

66. Lam, S.S., Martell, J.D., Kamer, K.J., Deerinck, T.J., Ellisman, M.H., Mootha, V.K., and Ting, A.Y. (2015). Directed evolution of APEX2 for electron microscopy and proximity labeling. Nat. Methods *12*, 51–54.

67. Lee, S.-Y., Kang, M.-G., Park, J.-S., Lee, G., Ting, A.Y., and Rhee, H.-W. (2016). APEX Fingerprinting Reveals the Subcellular Localization of Proteins of Interest. Cell Rep. *15*, 1837–1847.

68. Hung, V., Udeshi, N.D., Lam, S.S., Loh, K.H., Cox, K.J., Pedram, K., Carr, S.A., and Ting, A.Y. (2016). Spatially resolved proteomic mapping in living cells with

the engineered peroxidase APEX2. Nat. Protoc. *11*, 456–475.

69. Tran, J.R., Paulson, D.I., Moresco, J.J., Adam, S.A., Yates, J.R., Goldman, R.D., and Zheng, Y. (2021). An APEX2 proximity ligation method for mapping interactions with the nuclear lamina. J. Cell Biol. *220*. https://doi.org/10.1083/jcb.202002129.

70. Dumrongprechachan, V., Salisbury, R.B., Soto, G., Kumar, M., MacDonald, M.L., and Kozorovitskiy, Y. (2021). Cell-type and subcellular compartment-specific APEX2 proximity labeling reveals activity-dependent nuclear proteome dynamics in the striatum. Nat. Commun. *12*, 1–16.

71. Mito, M., Shichino, Y., and Iwasaki, S. (2023). Thor-Ribo-Seq: ribosome profiling tailored for low input with RNA-dependent RNA amplification. bioRxiv, 2023.01.15.524129. https://doi.org/10.1101/2023.01.15.524129.

72. Tomuro, K., Mito, M., Toh, H., Kawamoto, N., Miyake, T., Chow, S.Y.A., Doi, M., Ikeuchi, Y., Shichino, Y., and Iwasaki, S. (2024). Calibrated ribosome profiling assesses the dynamics of ribosomal flux on transcripts. Nat Commun *15*. https://doi.org/10.1038/s41467-024-51258-0.

73. Han, S., Udeshi, N.D., Deerinck, T.J., Svinkina, T., Ellisman, M.H., Carr, S.A., and Ting, A.Y. (2017). Proximity biotinylation as a method for mapping proteins associated with mtDNA in living cells. Cell Chem. Biol. *24*, 404–414.

74. Zhou, Y., Wang, G., Wang, P., Li, Z., Yue, T., Wang, J., and Zou, P. (2019). Expanding APEX2 substrates for proximity-dependent labeling of nucleic acids

and proteins in living cells. Angew. Chem. Int. Ed Engl. *58*, 11763–11767.

75. Zheng, F., Yu, C., Zhou, X., and Zou, P. (2023). Genetically encoded photocatalytic protein labeling enables spatially-resolved profiling of intracellular proteome. Nat. Commun. *14*, 2978.

76. Markmiller, S., Soltanieh, S., Server, K.L., Mak, R., Jin, W., Fang, M.Y., Luo, E.-C., Krach, F., Yang, D., Sen, A., et al. (2018). Context-dependent and disease-specific diversity in protein interactions within stress granules. Cell *172*, 590–604.e13.

77. Lee, S.-Y., Kang, M.-G., Shin, S., Kwak, C., Kwon, T., Seo, J.K., Kim, J.-S., and Rhee, H.-W. (2017). Architecture mapping of the inner mitochondrial membrane proteome by chemical tools in live cells. J. Am. Chem. Soc. *139*, 3651–3662.

78. Kim, D.I., Cutler, J.A., Na, C.H., Reckel, S., Renuse, S., Madugundu, A.K., Tahir, R., Goldschmidt, H.L., Reddy, K.L., Huganir, R.L., et al. (2018). BioSITe: A method for direct detection and quantitation of site-specific biotinylation. J. Proteome Res. *17*, 759–769.

79. Shin, S., Lee, S.-Y., Kang, M.-G., Jang, D.-G., Kim, J., Rhee, H.-W., and Kim, J.-S. (2024). Super-resolution proximity labeling with enhanced direct identification of biotinylation sites. Commun. Biol. *7*, 554.

80. Hirsch, J.D., Eslamizar, L., Filanoski, B.J., Malekzadeh, N., Haugland, R.P., Beechem, J.M., and Haugland, R.P. (2002). Easily reversible desthiobiotin binding to streptavidin, avidin, and other biotin-binding proteins: uses for protein labeling,

detection, and isolation. Anal. Biochem. *308*, 343–357.

81. McGlincy, N.J., and Ingolia, N.T. (2017). Transcriptome-wide measurement of translation by ribosome profiling. Methods *126*, 112–129.

82. Mito, M., Mishima, Y., and Iwasaki, S. (2020). Protocol for disome profiling to survey ribosome collision in humans and zebrafish. STAR Protoc *1*, 100168.

83. Temperley, R.J., Wydro, M., Lightowlers, R.N., and Chrzanowska-Lightowlers, Z.M. (2010). Human mitochondrial mRNAs—like members of all families, similar but different. Biochimica et Biophysica Acta (BBA) - Bioenergetics *1797*, 1081–1085.

84. Kummer, E., and Ban, N. (2021). Mechanisms and regulation of protein synthesis in mitochondria. Nat. Rev. Mol. Cell Biol. *22*, 307–325.

85. Li, Q., Yang, H., Stroup, E.K., Wang, H., and Ji, Z. (2022). Low-input RNase footprinting for simultaneous quantification of cytosolic and mitochondrial translation. Genome Res. *32*, 545–557.

86. Soto, I., Couvillion, M., Hansen, K.G., McShane, E., Moran, J.C., Barrientos, A., and Churchman, L.S. (2022). Balanced mitochondrial and cytosolic translatomes underlie the biogenesis of human respiratory complexes. Genome Biol. *23*, 170.

87. Wakigawa, T., Mito, M., Yamashiro, H., Tomuro, K., Tomizawa, K., Chujo, T., Nagao, A., Suzuki, T., Wei, F.-Y., Shichino, Y., et al. (2024). The complexity and dynamics of in organello translation assessed by high-resolution mitochondrial ribosome profiling. bioRxiv, 2023.07.19.549812.

https://doi.org/10.1101/2023.07.19.549812.

88. Uhlén, M., Karlsson, M.J., Hober, A., Svensson, A.-S., Scheffel, J., Kotol, D., Zhong, W., Tebani, A., Strandberg, L., Edfors, F., et al. (2019). The human secretome. Sci. Signal. *12*, eaaz0274.

89. Sterne-Weiler, T., Martinez-Nunez, R.T., Howard, J.M., Cvitovik, I., Katzman, S., Tariq, M.A., Pourmand, N., and Sanford, J.R. (2013). Frac-seq reveals isoform-specific recruitment to polyribosomes. Genome Res. *23*, 1615–1623.

90. Lee, S.-Y., Kang, M.-G., Park, J.-S., Lee, G., Ting, A.Y., and Rhee, H.-W. (2016). APEX fingerprinting reveals the subcellular localization of proteins of interest. Cell Rep. *15*, 1837–1847.

91. Linden, A. (2006). Measuring diagnostic and predictive accuracy in disease management: an introduction to receiver operating characteristic (ROC) analysis. J. Eval. Clin. Pract. *12*, 132–139.

92. Tsanov, N., Samacoits, A., Chouaib, R., Traboulsi, A.-M., Gostan, T., Weber, C., Zimmer, C., Zibara, K., Walter, T., Peter, M., et al. (2016). smiFISH and FISH-quant - a flexible single RNA detection approach with super-resolution capability. Nucleic Acids Res. *44*, e165.

93. Jacobs, J.L., and Coyne, C.B. (2013). Mechanisms of MAVS regulation at the mitochondrial membrane. J. Mol. Biol. *425*, 5009–5019.

94. Wu, M., Pei, Z., Long, G., Chen, H., Jia, Z., and Xia, W. (2023). Mitochondrial antiviral signaling protein: a potential therapeutic target in renal disease. Front.

Immunol. *14*, 1266461.

95. Rath, S., Sharma, R., Gupta, R., Ast, T., Chan, C., Durham, T.J., Goodman, R.P., Grabarek, Z., Haas, M.E., Hung, W.H.W., et al. (2021). MitoCarta3.0: an updated mitochondrial proteome now with sub-organelle localization and pathway annotations. Nucleic Acids Res. *49*, D1541–D1547.

96. Qin, W., Cheah, J.S., Xu, C., Messing, J., Freibaum, B.D., Boeynaems, S., Taylor, J.P., Udeshi, N.D., Carr, S.A., and Ting, A.Y. (2023). Dynamic mapping of proteome trafficking within and between living cells by TransitID. Cell *186*, 3307–3324.e30.

97. Go, C.D., Knight, J.D.R., Rajasekharan, A., Rathod, B., Hesketh, G.G., Abe, K.T., Youn, J.-Y., Samavarchi-Tehrani, P., Zhang, H., Zhu, L.Y., et al. (2021). A proximity-dependent biotinylation map of a human cell. Nature *595*, 120–124.

98. Wong, Y.L., Anzola, J.V., Davis, R.L., Yoon, M., Motamedi, A., Kroll, A., Seo, C.P., Hsia, J.E., Kim, S.K., Mitchell, J.W., et al. (2015). Cell biology. Reversible centriole depletion with an inhibitor of Polo-like kinase 4. Science *348*, 1155–1160.

99. Maaten, L., and Hinton, G.E. (2008). Visualizing Data using t-SNE. Journal of Machine Learning Research *9*, 2579–2605.

100. Wilson, E.L., and Metzakopian, E. (2021). ER-mitochondria contact sites in neurodegeneration: genetic screening approaches to investigate novel disease mechanisms. Cell Death Differ. *28*, 1804–1821.

101. Huotari, J., and Helenius, A. (2011). Endosome maturation. EMBO J. *30*, 3481–

3500.

102. Podinovskaia, M., Prescianotto-Baschong, C., Buser, D.P., and Spang, A. (2021). A novel live-cell imaging assay reveals regulation of endosome maturation. Elife *10*. https://doi.org/10.7554/eLife.70982.

103. McMahon, H.T., and Boucrot, E. (2011). Molecular mechanism and physiological functions of clathrin-mediated endocytosis. Nat. Rev. Mol. Cell Biol. *12*, 517–533.

104. Robinson, D.G., and Pimpl, P. (2014). Clathrin and post-Golgi trafficking: a very complicated issue. Trends Plant Sci. *19*, 134–139.

105. Nakano, A. (2022). The Golgi apparatus and its next-door neighbors. Front. Cell Dev. Biol. *10*, 884360.

106. Thul, P.J., Åkesson, L., Wiking, M., Mahdessian, D., Geladaki, A., Ait Blal, H., Alm, T., Asplund, A., Björk, L., Breckels, L.M., et al. (2017). A subcellular map of the human proteome. Science *356*. https://doi.org/10.1126/science.aal3321.

107. Szklarczyk, D., Kirsch, R., Koutrouli, M., Nastou, K., Mehryary, F., Hachilif, R., Gable, A.L., Fang, T., Doncheva, N.T., Pyysalo, S., et al. (2023). The STRING database in 2023: protein-protein association networks and functional enrichment analyses for any sequenced genome of interest. Nucleic Acids Res. *51*, D638–D646.

108. Itskanov, S., and Park, E. (2023). Mechanism of protein translocation by the Sec61 translocon complex. Cold Spring Harb. Perspect. Biol. *15*, a041250.

109. Jaskolowski, M., Jomaa, A., Gamerdinger, M., Shrestha, S., Leibundgut, M.,

Deuerling, E., and Ban, N. (2023). Molecular basis of the TRAP complex function in ER protein biogenesis. Nat. Struct. Mol. Biol. *30*, 770–777.

110. Zanotti, A., Coelho, J.P.L., Kaylani, D., Singh, G., Tauber, M., Hitzenberger, M., Avci, D., Zacharias, M., Russell, R.B., Lemberg, M.K., et al. (2022). The human signal peptidase complex acts as a quality control enzyme for membrane proteins. Science *378*, 996–1000.

111. Liaci, A.M., Steigenberger, B., Telles de Souza, P.C., Tamara, S., Gröllers-Mulderij, M., Ogrissek, P., Marrink, S.J., Scheltema, R.A., and Förster, F. (2021). Structure of the human signal peptidase complex reveals the determinants for signal peptide cleavage. Mol. Cell *81*, 3934–3948.e11.

112. Ramírez, A.S., de Capitani, M., Pesciullesi, G., Kowal, J., Bloch, J.S., Irobalieva, R.N., Reymond, J.-L., Aebi, M., and Locher, K.P. (2022). Molecular basis for glycan recognition and reaction priming of eukaryotic oligosaccharyltransferase. Nat. Commun. *13*, 7296.

113. Bai, L., Wang, T., Zhao, G., Kovach, A., and Li, H. (2018). The atomic structure of a eukaryotic oligosaccharyltransferase complex. Nature *555*, 328–333.

114. Nussberger, S., Ghosh, R., and Wang, S. (2024). New insights into the structure and dynamics of the TOM complex in mitochondria. Biochem. Soc. Trans. *52*, 911–922.

115. Coyne, A.N., and Rothstein, J.D. (2022). Nuclear pore complexes - a doorway to neural injury in neurodegeneration. Nat. Rev. Neurol. *18*, 348–362.

116. Spiliotis, E.T., and McMurray, M.A. (2020). Masters of asymmetry - lessons and perspectives from 50 years of septins. Mol. Biol. Cell *31*, 2289–2297.

117. Arakel, E.C., and Schwappach, B. (2018). Formation of COPI-coated vesicles at a glance. J. Cell Sci. *131*. https://doi.org/10.1242/jcs.209890.

118. van der Beek, J., Jonker, C., van der Welle, R., Liv, N., and Klumperman, J. (2019). CORVET, CHEVI and HOPS - multisubunit tethers of the endo-lysosomal system in health and disease. J. Cell Sci. *132*, jcs189134.

119. Hollopeter, G. (2024). Stepwise assembly of the AP2 endocytic clathrin adaptor complex. Proc. Natl. Acad. Sci. U. S. A. *121*, e2415313121.

120. Seaman, M.N.J. (2021). The retromer complex: From genesis to revelations. Trends Biochem. Sci. *46*, 608–620.

121. Forgac, M. (2007). Vacuolar ATPases: rotary proton pumps in physiology and pathophysiology. Nat. Rev. Mol. Cell Biol. *8*, 917–929.

122. Ghosh, E., Kumari, P., Jaiman, D., and Shukla, A.K. (2015). Methodological advances: the unsung heroes of the GPCR structural revolution. Nat. Rev. Mol. Cell Biol. *16*, 69–81.

123. Lorenzo, D.N., Edwards, R.J., and Slavutsky, A.L. (2023). Spectrins: molecular organizers and targets of neurological disorders. Nat. Rev. Neurosci. *24*, 195–212.

124. Bonifacino, J.S., and Hierro, A. (2011). Transport according to GARP: receiving retrograde cargo at the trans-Golgi network. Trends Cell Biol. *21*, 159–167.

125. Barrowman, J., Bhandari, D., Reinisch, K., and Ferro-Novick, S. (2010). TRAPP complexes in membrane traffic: convergence through a common Rab. Nat. Rev. Mol. Cell Biol. *11*, 759–763.

126. Herranz-Montoya, I., Park, S., and Djouder, N. (2021). A comprehensive analysis of prefoldins and their implication in cancer. iScience *24*, 103273.

127. Halic, M., and Beckmann, R. (2005). The signal recognition particle and its interactions during protein targeting. Curr. Opin. Struct. Biol. *15*, 116–125.

128. Bertolini, M., Fenzl, K., Kats, I., Wruck, F., Tippmann, F., Schmitt, J., Auburger, J.J., Tans, S., Bukau, B., and Kramer, G. (2021). Interactions between nascent proteins translated by adjacent ribosomes drive homomer assembly. Science *371*, 57–64.

129. Mallik, S., Venezian, J., Lobov, A., Heidenreich, M., Garcia-Seisdedos, H., Yeates, T.O., Shiber, A., and Levy, E.D. (2025). Structural determinants of co-translational protein complex assembly. Cell *188*, 764–777.e22.

130. Muthukumar, G., Stevens, T.A., Inglis, A.J., Esantsi, T.K., Saunders, R.A., Schulte, F., Voorhees, R.M., Guna, A., and Weissman, J.S. (2024). Triaging of α-helical proteins to the mitochondrial outer membrane by distinct chaperone machinery based on substrate topology. Mol. Cell *84*, 1101–1119.e9.

131. Gemmer, M., Chaillet, M.L., van Loenhout, J., Cuevas Arenas, R., Vismpas, D., Gröllers-Mulderij, M., Koh, F.A., Albanese, P., Scheltema, R.A., Howes, S.C., et al. (2023). Visualization of translation and protein biogenesis at the ER membrane.

Nature *614*, 160–167.

132. Ott, M., and Herrmann, J.M. (2010). Co-translational membrane insertion of mitochondrially encoded proteins. Biochim. Biophys. Acta *1803*, 767–775.

133. Shao, S., and Hegde, R.S. (2011). Membrane protein insertion at the endoplasmic reticulum. Annu. Rev. Cell Dev. Biol. *27*, 25–56.

134. McShane, E., Couvillion, M., Ietswaart, R., Prakash, G., Smalec, B.M., Soto, I., Baxter-Koenigs, A.R., Choquet, K., and Churchman, L.S. (2024). A kinetic dichotomy between mitochondrial and nuclear gene expression processes. Mol. Cell *84*, 1541–1555.e11.

135. Béthune, J., Jansen, R.-P., Feldbrügge, M., and Zarnack, K. (2019). Membrane-associated RNA-binding proteins orchestrate organelle-coupled translation. Trends Cell Biol. *29*, 178–188.

136. Van Nostrand, E.L., Freese, P., Pratt, G.A., Wang, X., Wei, X., Xiao, R., Blue, S.M., Chen, J.-Y., Cody, N.A.L., Dominguez, D., et al. (2020). A large-scale binding and functional map of human RNA-binding proteins. Nature *583*, 711–719.

137. Horste, E.L., Fansler, M.M., Cai, T., Chen, X., Mitschka, S., Zhen, G., Lee, F.C.Y., Ule, J., and Mayr, C. (2023). Subcytoplasmic location of translation controls protein output. Mol. Cell *83*, 4509–4523.e11.

138. Lewis, B.M., Cho, C.Y., Her, H.-L., Mizrahi, O., Hunter, T., and Yeo, G.W. (2024). LARP4 is an RNA-binding protein that binds nuclear-encoded mitochondrial mRNAs to promote mitochondrial function. RNA *30*, 223–239.

139. Coleman, J.C., Tattersall, L., Yianni, V., Knight, L., Yu, H., Hallett, S.R., Johnson, P., Caetano, A.J., Cosstick, C., Ridley, A.J., et al. (2024). The RNA binding proteins LARP4A and LARP4B promote sarcoma and carcinoma growth and metastasis. iScience *27*, 109288.

140. Gabrovsek, L., Collins, K.B., Aggarwal, S., Saunders, L.M., Lau, H.-T., Suh, D., Sancak, Y., Trapnell, C., Ong, S.-E., Smith, F.D., et al. (2020). A-kinase-anchoring protein 1 (dAKAP1)-based signaling complexes coordinate local protein synthesis at the mitochondrial surface. J. Biol. Chem. *295*, 10749–10765.

141. Zipor, G., Haim-Vilmovsky, L., Gelin-Licht, R., Gadir, N., Brocard, C., and Gerst, J.E. (2009). Localization of mRNAs coding for peroxisomal proteins in the yeast, *Saccharomyces cerevisiae*. Proc. Natl. Acad. Sci. U. S. A. *106*, 19848–19853.

142. Consens, M.E., Dufault, C., Wainberg, M., Forster, D., Karimzadeh, M., Goodarzi, H., Theis, F.J., Moses, A., and Wang, B. (2025). Transformers and genome language models. Nat. Mach. Intell. https://doi.org/10.1038/s42256-025-01007-9.

143. Zou, S., Tao, T., Mahbub, S., Ellington, C.N., Algayres, R.J., Li, D., Zhuang, Y., Wang, H., Song, L., and Xing, E.P. (2024). A large-scale foundation model for RNA function and structure prediction. bioRxiv. https://doi.org/10.1101/2024.11.28.625345.

144. Penić, R.J., Vlašić, T., Huber, R.G., Wan, Y., and Šikić, M. (2024). RiNALMo: General-purpose RNA language models can generalize well on structure prediction tasks. arXiv [q-bio.BM].

145. Brixi, G., Durrant, M.G., Ku, J., Poli, M., Brockman, G., Chang, D., Gonzalez, G.A., King, S.H., Li, D.B., Merchant, A.T., et al. (2025). Genome modeling and design across all domains of life with Evo 2. bioRxiv. https://doi.org/10.1101/2025.02.18.638918.

146. Voigt, F., Zhang, H., Cui, X.A., Triebold, D., Liu, A.X., Eglinger, J., Lee, E.S., Chao, J.A., and Palazzo, A.F. (2017). Single-molecule quantification of translation-dependent association of mRNAs with the endoplasmic reticulum. Cell Rep. *21*, 3740–3753.

147. Ingolia, N.T., Lareau, L.F., and Weissman, J.S. (2011). Ribosome profiling of mouse embryonic stem cells reveals the complexity and dynamics of mammalian proteomes. Cell *147*, 789–802.

148. Barrington, C.L., Galindo, G., Koch, A.L., Horton, E.R., Morrison, E.J., Tisa, S., Stasevich, T.J., and Rissland, O.S. (2023). Synonymous codon usage regulates translation initiation. Cell Rep. *42*, 113413.

149. Lyons, E.F., Devanneaux, L.C., Muller, R.Y., Freitas, A.V., Meacham, Z.A., McSharry, M.V., Trinh, V.N., Rogers, A.J., Ingolia, N.T., and Lareau, L.F. (2023). Translation elongation as a rate limiting step of protein production. bioRxiv. https://doi.org/10.1101/2023.11.27.568910.

150. Couvillion, M.T., Soto, I.C., Shipkovenska, G., and Churchman, L.S. (2016). Synchronized mitochondrial and cytosolic translation programs. Nature *533*, 499–503.

151. Zein-Sabatto, H., and Lerit, D.A. (2021). The identification and functional analysis of mRNA localizing to centrosomes. Front Cell Dev Biol *9*, 782802.

152. Tanenbaum, M.E., Stern-Ginossar, N., Weissman, J.S., and Vale, R.D. (2015). Regulation of mRNA translation during mitosis. Elife *4*. https://doi.org/10.7554/eLife.07957.

153. Ryder, P.V., Fang, J., and Lerit, D.A. (2020). <ita>centrocortin</ita> RNA localization to centrosomes is regulated by FMRP and facilitates error-free mitosis. J. Cell Biol. *219*. https://doi.org/10.1083/jcb.202004101.

154. Weber, R., Kleemann, L., Hirschberg, I., Chung, M.-Y., Valkov, E., and Igreja, C. (2022). DAP5 enables main ORF translation on mRNAs with structured and uORF-containing 5' leaders. Nat. Commun. *13*, 7510.

155. Glauninger, H., Wong Hickernell, C.J., Bard, J.A.M., and Drummond, D.A. (2022). Stressful steps: Progress and challenges in understanding stress-induced mRNA condensation and accumulation in stress granules. Mol. Cell *82*, 2544–2556.

156. Pan, C.R., Knutson, S.D., Huth, S.W., and MacMillan, D.W.C. (2025). µMap proximity labeling in living cells reveals stress granule disassembly mechanisms. Nat. Chem. Biol. *21*, 490–500.

157. Yang, P., Mathieu, C., Kolaitis, R.-M., Zhang, P., Messing, J., Yurtsever, U., Yang, Z., Wu, J., Li, Y., Pan, Q., et al. (2020). G3BP1 is a tunable switch that triggers phase separation to assemble stress granules. Cell *181*, 325–345.e28.

158. Ren, Z., Tang, W., Peng, L., and Zou, P. (2023). Profiling stress-triggered RNA

condensation with photocatalytic proximity labeling. Nat. Commun. *14*, 7390.

159. Youn, J.-Y., Dunham, W.H., Hong, S.J., Knight, J.D.R., Bashkurov, M., Chen, G.I., Bagci, H., Rathod, B., MacLeod, G., Eng, S.W.M., et al. (2018). High-density proximity mapping reveals the subcellular organization of mRNA-associated granules and bodies. Mol. Cell *69*, 517–532.e11.

160. Guillén-Boixet, J., Kopach, A., Holehouse, A.S., Wittmann, S., Jahnel, M., Schlüßler, R., Kim, K., Trussina, I.R.E.A., Wang, J., Mateju, D., et al. (2020). RNA-induced conformational switching and clustering of G3BP drive stress granule assembly by condensation. Cell *181*, 346–361.e17.

161. Sanders, D.W., Kedersha, N., Lee, D.S.W., Strom, A.R., Drake, V., Riback, J.A., Bracha, D., Eeftens, J.M., Iwanicki, A., Wang, A., et al. (2020). Competing protein-RNA interaction networks control multiphase intracellular organization. Cell *181*, 306–324.e28.

162. Andreev, D.E., O'Connor, P.B.F., Fahey, C., Kenny, E.M., Terenin, I.M., Dmitriev, S.E., Cormican, P., Morris, D.W., Shatsky, I.N., and Baranov, P.V. (2015). Translation of 5' leaders is pervasive in genes resistant to eIF2 repression. Elife *4*, e03971.

163. Khong, A., Matheny, T., Jain, S., Mitchell, S.F., Wheeler, J.R., and Parker, R. (2017). The stress granule transcriptome reveals principles of mRNA accumulation in stress granules. Mol. Cell *68*, 808–820.e5.

164. Damgaard, C.K., and Lykke-Andersen, J. (2011). Translational coregulation of

5'TOP mRNAs by TIA-1 and TIAR. Genes Dev. *25*, 2057–2068.

165. Halstead, J.M., Lionnet, T., Wilbertz, J.H., Wippich, F., Ephrussi, A., Singer, R.H., and Chao, J.A. (2015). Translation. An RNA biosensor for imaging the first round of translation from single cells to living animals. Science *347*, 1367–1671.

166. Philippe, L., van den Elzen, A.M.G., Watson, M.J., and Thoreen, C.C. (2020). Global analysis of LARP1 translation targets reveals tunable and dynamic features of 5′ TOP motifs. Proceedings of the National Academy of Sciences *117*, 5319–5328.

167. Repici, M., Hassanjani, M., Maddison, D.C., Garção, P., Cimini, S., Patel, B., Szegö, É.M., Straatman, K.R., Lilley, K.S., Borsello, T., et al. (2019). The Parkinson's disease-linked protein DJ-1 associates with cytoplasmic mRNP granules during stress and neurodegeneration. Mol. Neurobiol. *56*, 61–77.

168. Nakatogawa, H. (2020). Mechanisms governing autophagosome biogenesis. Nat. Rev. Mol. Cell Biol. *21*, 439–458.

169. Kawabata, T., and Yoshimori, T. (2020). Autophagosome biogenesis and human health. Cell Discov. *6*, 33.

170. Darnell, A.M., Subramaniam, A.R., and O'Shea, E.K. (2018). Translational control through differential ribosome pausing during amino acid limitation in mammalian cells. Mol. Cell *71*, 229–243.e11.

171. Pu, J., Schindler, C., Jia, R., Jarnik, M., Backlund, P., and Bonifacino, J.S. (2015). BORC, a multisubunit complex that regulates lysosome positioning. Dev. Cell *33*,

176–188.

172. Jia, R., Guardia, C.M., Pu, J., Chen, Y., and Bonifacino, J.S. (2017). BORC coordinates encounter and fusion of lysosomes with autophagosomes. Autophagy *13*, 1648–1663.

173. Leidal, A.M., Huang, H.H., Marsh, T., Solvik, T., Zhang, D., Ye, J., Kai, F., Goldsmith, J., Liu, J.Y., Huang, Y.-H., et al. (2020). The LC3-conjugation machinery specifies the loading of RNA-binding proteins into extracellular vesicles. Nat. Cell Biol. *22*, 187–199.

174. Behrends, C., Sowa, M.E., Gygi, S.P., and Harper, J.W. (2010). Network organization of the human autophagy system. Nature *466*, 68–76.

175. Shinoda, S., Sakai, Y., Matsui, T., Uematsu, M., Koyama-Honda, I., Sakamaki, J.-I., Yamamoto, H., and Mizushima, N. (2024). Syntaxin 17 recruitment to mature autophagosomes is temporally regulated by PI4P accumulation. Elife *12*. https://doi.org/10.7554/eLife.92189.

176. Makino, S., Kawamata, T., Iwasaki, S., and Ohsumi, Y. (2021). Selectivity of mRNA degradation by autophagy in yeast. Nat. Commun. *12*, 2316.

177. Zhang, W., Fu, Y., Peng, L., Ogawa, Y., Ding, X., Rasband, A., Zhou, X., Shelly, M., Rasband, M.N., and Zou, P. (2023). Immunoproximity biotinylation reveals the axon initial segment proteome. Nat. Commun. *14*, 8201.

178. Sainio, M.T., Rasila, T., Molchanova, S.M., Järvilehto, J., Torregrosa-Muñumer, R., Harjuhaahto, S., Pennonen, J., Huber, N., Herukka, S.-K., Haapasalo, A., et al.

(2021). Neurofilament light regulates axon caliber, synaptic activity, and organelle trafficking in cultured human motor neurons. Front. Cell Dev. Biol. *9*, 820105.

179. Chung, C.Y., Khurana, V., Yi, S., Sahni, N., Loh, K.H., Auluck, P.K., Baru, V., Udeshi, N.D., Freyzon, Y., Carr, S.A., et al. (2017). In situ peroxidase labeling and mass-spectrometry connects alpha-synuclein directly to endocytic trafficking and mRNA metabolism in neurons. Cell Syst. *4*, 242–250.e4.

180. Cajigas, I.J., Tushev, G., Will, T.J., tom Dieck, S., Fuerst, N., and Schuman, E.M. (2012). The local transcriptome in the synaptic neuropil revealed by deep sequencing and high-resolution imaging. Neuron *74*, 453–466.

181. Hale, C.R., Sawicka, K., Mora, K., Fak, J.J., Kang, J.J., Cutrim, P., Cialowicz, K., Carroll, T.S., and Darnell, R.B. (2021). FMRP regulates mRNAs encoding distinct functions in the cell body and dendrites of CA1 pyramidal neurons. Elife *10*. https://doi.org/10.7554/eLife.71892.

182. Kratz, A., Beguin, P., Kaneko, M., Chimura, T., Suzuki, A.M., Matsunaga, A., Kato, S., Bertin, N., Lassmann, T., Vigot, R., et al. (2014). Digital expression profiling of the compartmentalized translatome of Purkinje neurons. Genome Res. *24*, 1396–1410.

183. Graber, T.E., Hébert-Seropian, S., Khoutorsky, A., David, A., Yewdell, J.W., Lacaille, J.-C., and Sossin, W.S. (2013). Reactivation of stalled polyribosomes in synaptic plasticity. Proc. Natl. Acad. Sci. U. S. A. *110*, 16205–16210.

184. Bauer, K.E., de Queiroz, B.R., Kiebler, M.A., and Besse, F. (2023). RNA granules

in neuronal plasticity and disease. Trends Neurosci. *46*, 525–538.

185. Conde, C., and Cáceres, A. (2009). Microtubule assembly, organization and dynamics in axons and dendrites. Nat. Rev. Neurosci. *10*, 319–332.

186. Chamberlain, K.A., and Sheng, Z.-H. (2019). Mechanisms for the maintenance and regulation of axonal energy supply. J. Neurosci. Res. *97*, 897–913.

187. Xia, C., Fan, J., Emanuel, G., Hao, J., and Zhuang, X. (2019). Spatial transcriptome profiling by MERFISH reveals subcellular RNA compartmentalization and cell cycle-dependent gene expression. Proc. Natl. Acad. Sci. U. S. A. *116*, 19490–19499.

188. tom Dieck, S., Kochen, L., Hanus, C., Heumüller, M., Bartnik, I., Nassim-Assir, B., Merk, K., Mosler, T., Garg, S., Bunse, S., et al. (2015). Direct visualization of newly synthesized target proteins in situ. Nat. Methods *12*, 411–414.

189. Villanueva, E., Smith, T., Pizzinga, M., Elzek, M., Queiroz, R.M.L., Harvey, R.F., Breckels, L.M., Crook, O.M., Monti, M., Dezi, V., et al. (2023). System-wide analysis of RNA and protein subcellular localization dynamics. Nat. Methods *21*, 60–71.

190. Roux, K.J., Kim, D.I., Raida, M., and Burke, B. (2012). A promiscuous biotin ligase fusion protein identifies proximal and interacting proteins in mammalian cells. J. Cell Biol. *196*, 801–810.

191. Rhee, H.-W., Zou, P., Udeshi, N.D., Martell, J.D., Mootha, V.K., Carr, S.A., and Ting, A.Y. (2013). Proteomic mapping of mitochondria in living cells via spatially

restricted enzymatic tagging. Science *339*, 1328–1331.

192. Branon, T.C., Bosch, J.A., Sanchez, A.D., Udeshi, N.D., Svinkina, T., Carr, S.A., Feldman, J.L., Perrimon, N., and Ting, A.Y. (2018). Efficient proximity labeling in living cells and organisms with TurboID. Nat. Biotechnol. *36*, 880–887.

193. Cho, K.F., Branon, T.C., Rajeev, S., Svinkina, T., Udeshi, N.D., Thoudam, T., Kwak, C., Rhee, H.-W., Lee, I.-K., Carr, S.A., et al. (2020). Split-TurboID enables contact-dependent proximity labeling in cells. Proc. Natl. Acad. Sci. U. S. A. *117*, 12143–12154.

194. Marmor-Kollet, H., Siany, A., Kedersha, N., Knafo, N., Rivkin, N., Danino, Y.M., Moens, T.G., Olender, T., Sheban, D., Cohen, N., et al. (2020). Spatiotemporal proteomic analysis of stress granule disassembly using APEX reveals regulation by SUMOylation and links to ALS pathogenesis. Mol. Cell *80*, 876–891.e6.

195. Middleton, S.A., Eberwine, J., and Kim, J. (2019). Comprehensive catalog of dendritically localized mRNA isoforms from sub-cellular sequencing of single mouse neurons. BMC Biol. *17*, 5.

196. Tushev, G., Glock, C., Heumüller, M., Biever, A., Jovanovic, M., and Schuman, E.M. (2018). Alternative 3′ UTRs modify the localization, regulatory potential, stability, and plasticity of mRNAs in neuronal compartments. Neuron *98*, 495–511.e6.

197. Tanimura, A., Nezu, A., Morita, T., Turner, R.J., and Tojyo, Y. (2004). Fluorescent biosensor for quantitative real-time measurements of inositol 1,4,5-trisphosphate in

single living cells. J. Biol. Chem. *279*, 38095–38098.

198. Varnai, P., Thyagarajan, B., Rohacs, T., and Balla, T. (2006). Rapidly inducible changes in phosphatidylinositol 4,5-bisphosphate levels influence multiple regulatory functions of the lipid in intact living cells. J. Cell Biol. *175*, 377–382.

199. Wilhelmsen, K., Litjens, S.H.M., Kuikman, I., Tshimbalanga, N., Janssen, H., van den Bout, I., Raymond, K., and Sonnenberg, A. (2005). Nesprin-3, a novel outer nuclear membrane protein, associates with the cytoskeletal linker protein plectin. J. Cell Biol. *171*, 799–810.

200. Zellner, S., Schifferer, M., and Behrends, C. (2021). Systematically defining selective autophagy receptor-specific cargo using autophagosome content profiling. Mol. Cell *81*, 1337–1354.e8.

201. Meitinger, F., Ohta, M., Lee, K.-Y., Watanabe, S., Davis, R.L., Anzola, J.V., Kabeche, R., Jenkins, D.A., Shiau, A.K., Desai, A., et al. (2020). TRIM37 controls cancer-specific vulnerability to PLK4 inhibition. Nature *585*, 440–446.

202. Sano, H., Kobayashi, K., Yoshioka, N., Takebayashi, H., and Nambu, A. (2020). Retrograde gene transfer into neural pathways mediated by adeno-associated virus (AAV)-AAV receptor interaction. J. Neurosci. Methods *345*, 108887.

203. Horio, T., Ishikura, Y., Ohashi, R., and Shiina, N. (2023). Regulation of RNG105/caprin1 dynamics by pathogenic cytoplasmic FUS and TDP-43 in neuronal RNA granules modulates synaptic loss. Heliyon *9*, e17065.

204. Shichino, Y., Yamaguchi, T., Kashiwagi, K., Mito, M., Takahashi, M., Ito, T.,

Ingolia, N.T., Kuba, K., and Iwasaki, S. (2024). eIF4A1 enhances LARP1-mediated translational repression during mTORC1 inhibition. Nat. Struct. Mol. Biol. *31*, 1557–1566.

205. Wu, Q., Shichino, Y., Abe, T., Suetsugu, T., Omori, A., Kiyonari, H., Iwasaki, S., and Matsuzaki, F. (2022). Selective translation of epigenetic modifiers affects the temporal pattern and differentiation of neural stem cells. Nat. Commun. *13*, 470.

206. Kobayashi, H., and Singer, R.H. (2022). Single-molecule imaging of microRNA-mediated gene silencing in cells. Nat. Commun. *13*, 1435.

207. Schindelin, J., Arganda-Carreras, I., Frise, E., Kaynig, V., Longair, M., Pietzsch, T., Preibisch, S., Rueden, C., Saalfeld, S., Schmid, B., et al. (2012). Fiji: an open-source platform for biological-image analysis. Nat. Methods *9*, 676–682.

208. Stringer, C., Wang, T., Michaelos, M., and Pachitariu, M. (2021). Cellpose: a generalist algorithm for cellular segmentation. Nat. Methods *18*, 100–106.

209. Imbert, A., Ouyang, W., Safieddine, A., Coleno, E., Zimmer, C., Bertrand, E., Walter, T., and Mueller, F. (2022). FISH-quant v2: a scalable and modular tool for smFISH image analysis. RNA *28*, 786–795.

210. Kashiwagi, K., Shichino, Y., Osaki, T., Sakamoto, A., Nishimoto, M., Takahashi, M., Mito, M., Weber, F., Ikeuchi, Y., Iwasaki, S., et al. (2021). eIF2B-capturing viral protein NSs suppresses the integrated stress response. Nat. Commun. *12*, 7102.

211. Chen, S., Zhou, Y., Chen, Y., and Gu, J. (2018). fastp: an ultra-fast all-in-one

FASTQ preprocessor. Bioinformatics *34*, i884–i890.

212. Martin, M. (2011). Cutadapt removes adapter sequences from high-throughput sequencing reads. EMBnet J. *17*, 10.

213. Smith, T., Heger, A., and Sudbery, I. (2017). UMI-tools: modeling sequencing errors in Unique Molecular Identifiers to improve quantification accuracy. Genome Res. *27*, 491–499.

214. Dobin, A., Davis, C.A., Schlesinger, F., Drenkow, J., Zaleski, C., Jha, S., Batut, P., Chaisson, M., and Gingeras, T.R. (2013). STAR: ultrafast universal RNA-seq aligner. Bioinformatics *29*, 15–21.

215. Morales, J., Pujar, S., Loveland, J.E., Astashyn, A., Bennett, R., Berry, A., Cox, E., Davidson, C., Ermolaeva, O., Farrell, C.M., et al. (2022). A joint NCBI and EMBL-EBI transcript set for clinical genomics and research. Nature *604*, 310–315.

216. Love, M.I., Huber, W., and Anders, S. (2014). Moderated estimation of fold change and dispersion for RNA-seq data with DESeq2. Genome Biol. *15*, 550.

217. Käll, L., Krogh, A., and Sonnhammer, E.L.L. (2004). A combined transmembrane topology and signal peptide prediction method. J. Mol. Biol. *338*, 1027–1036.

218. Krogh, A., Larsson, B., von Heijne, G., and Sonnhammer, E.L. (2001). Predicting transmembrane protein topology with a hidden Markov model: application to complete genomes. J. Mol. Biol. *305*, 567–580.

219. Petersen, T.N., Brunak, S., von Heijne, G., and Nielsen, H. (2011). SignalP 4.0: discriminating signal peptides from transmembrane regions. Nat. Methods *8*, 785–

786.

220. Heinz, S., Benner, C., Spann, N., Bertolino, E., Lin, Y.C., Laslo, P., Cheng, J.X., Murre, C., Singh, H., and Glass, C.K. (2010). Simple combinations of lineage-determining transcription factors prime cis-regulatory elements required for macrophage and B cell identities. Mol. Cell *38*, 576–589.

221. Thumuluri, V., Almagro Armenteros, J.J., Johansen, A.R., Nielsen, H., and Winther, O. (2022). DeepLoc 2.0: multi-label subcellular localization prediction using protein language models. Nucleic Acids Res. *50*, W228–W234.

222. Nakamura, Y., Gojobori, T., and Ikemura, T. (2000). Codon usage tabulated from international DNA sequence databases: status for the year 2000. Nucleic Acids Res. *28*, 292.

223. van der Maaten, L. (2014). Accelerating t-SNE using Tree-Based Algorithms. Journal of Machine Learning Research *15*, 3221–3245.

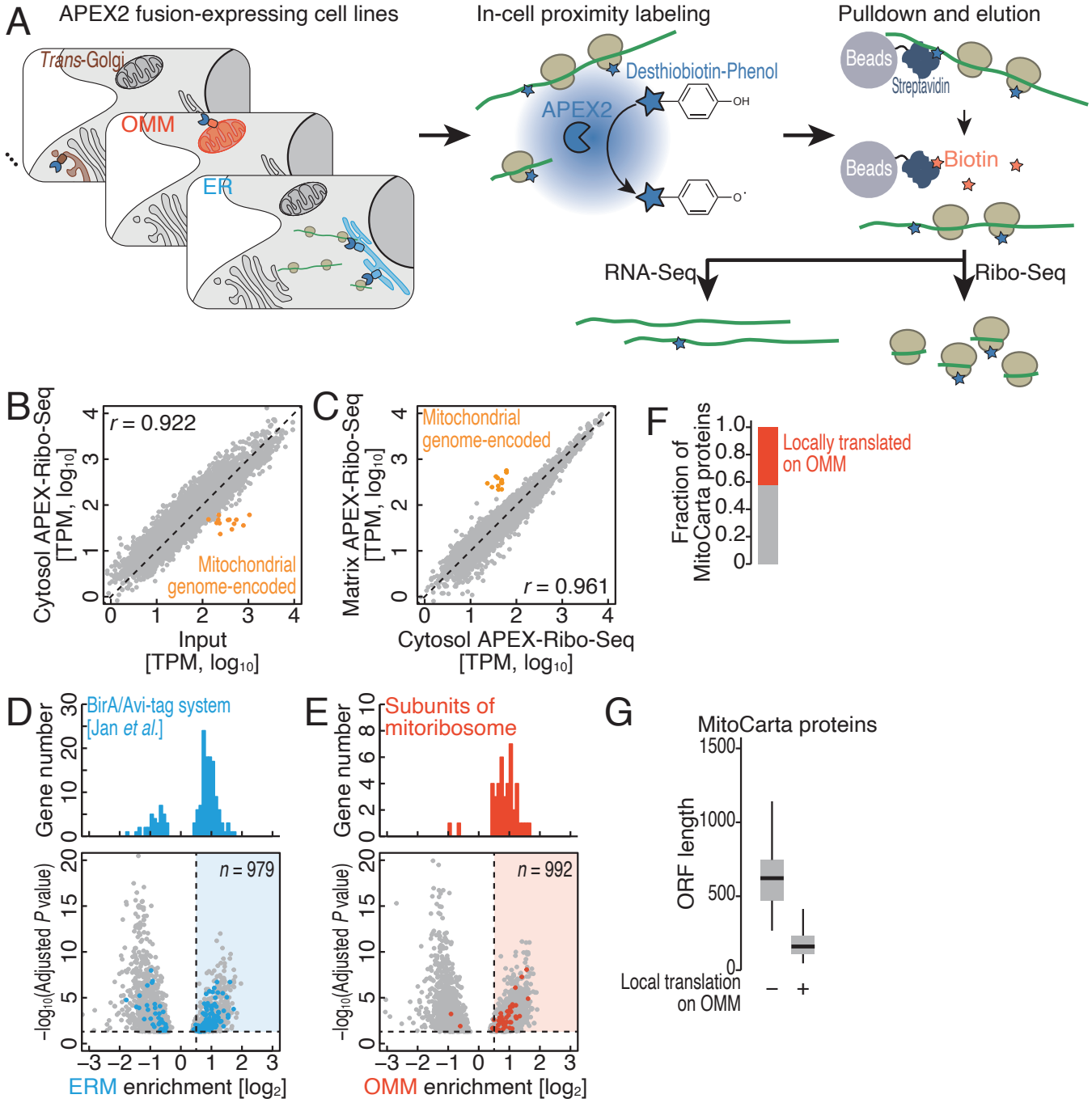

Figure 1 Tomuro *et al.* (2025)

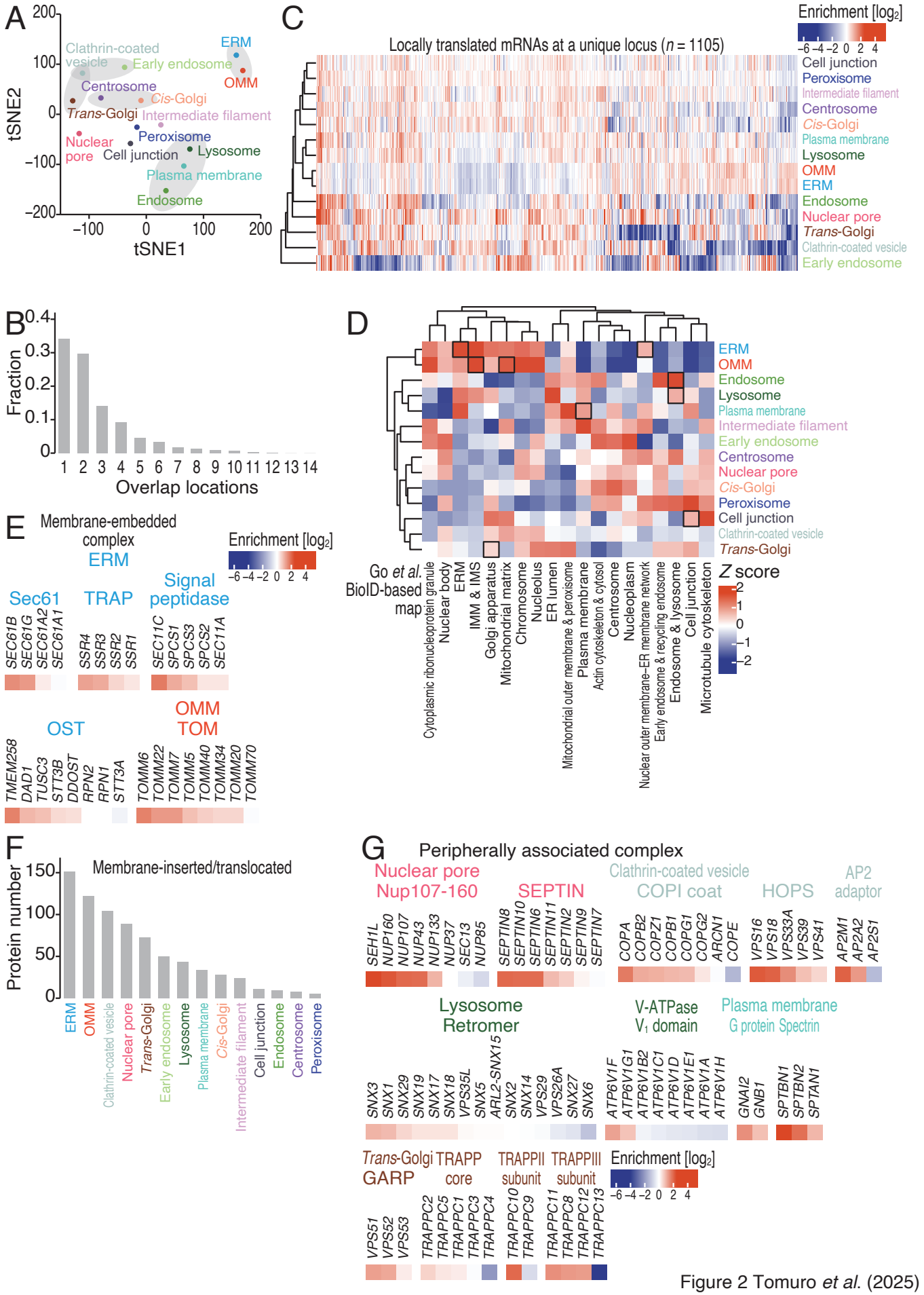

Figure 2 Tomuro *et al.* (2025)

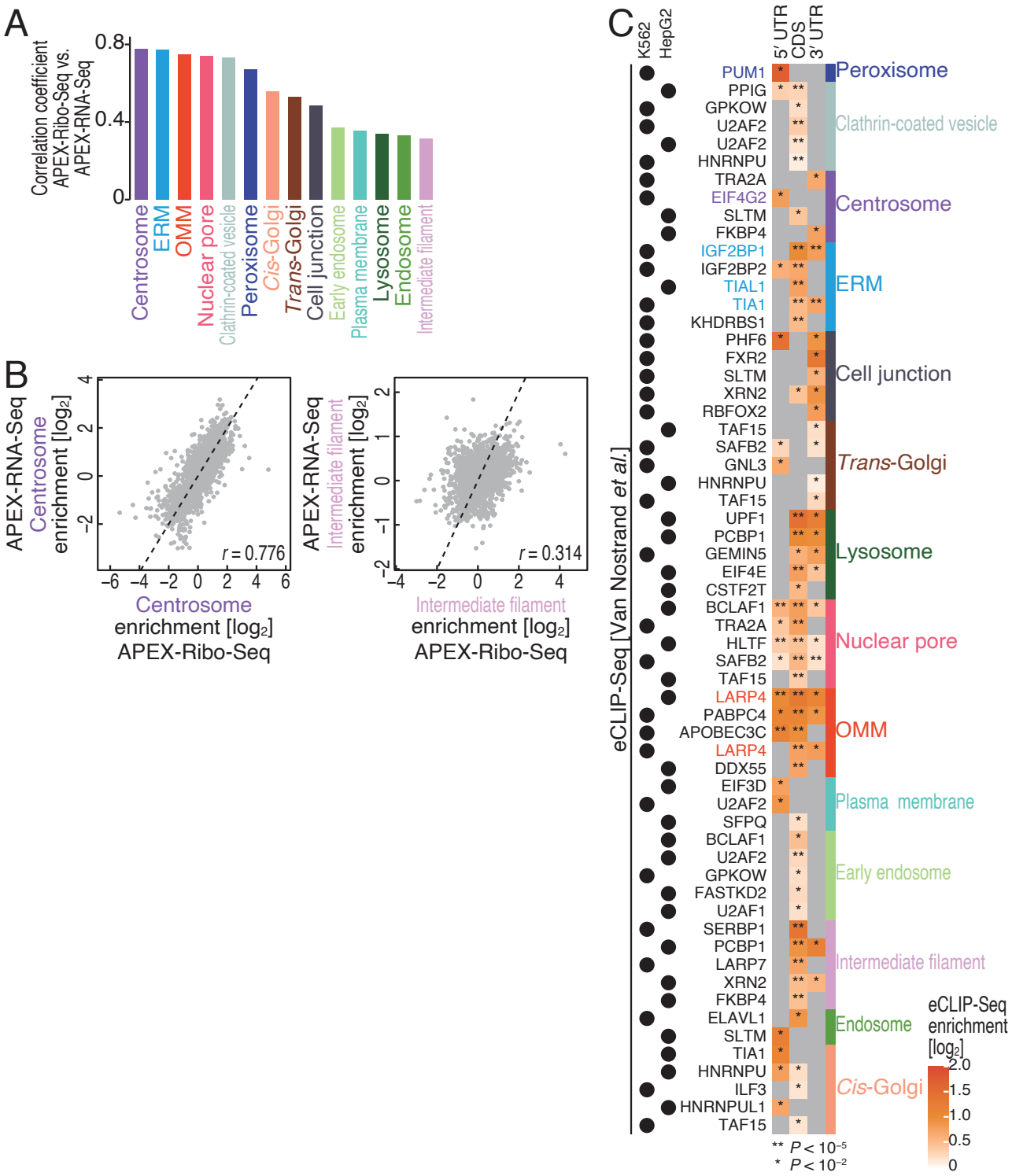

Figure 3 Tomuro *et al.* (2025)

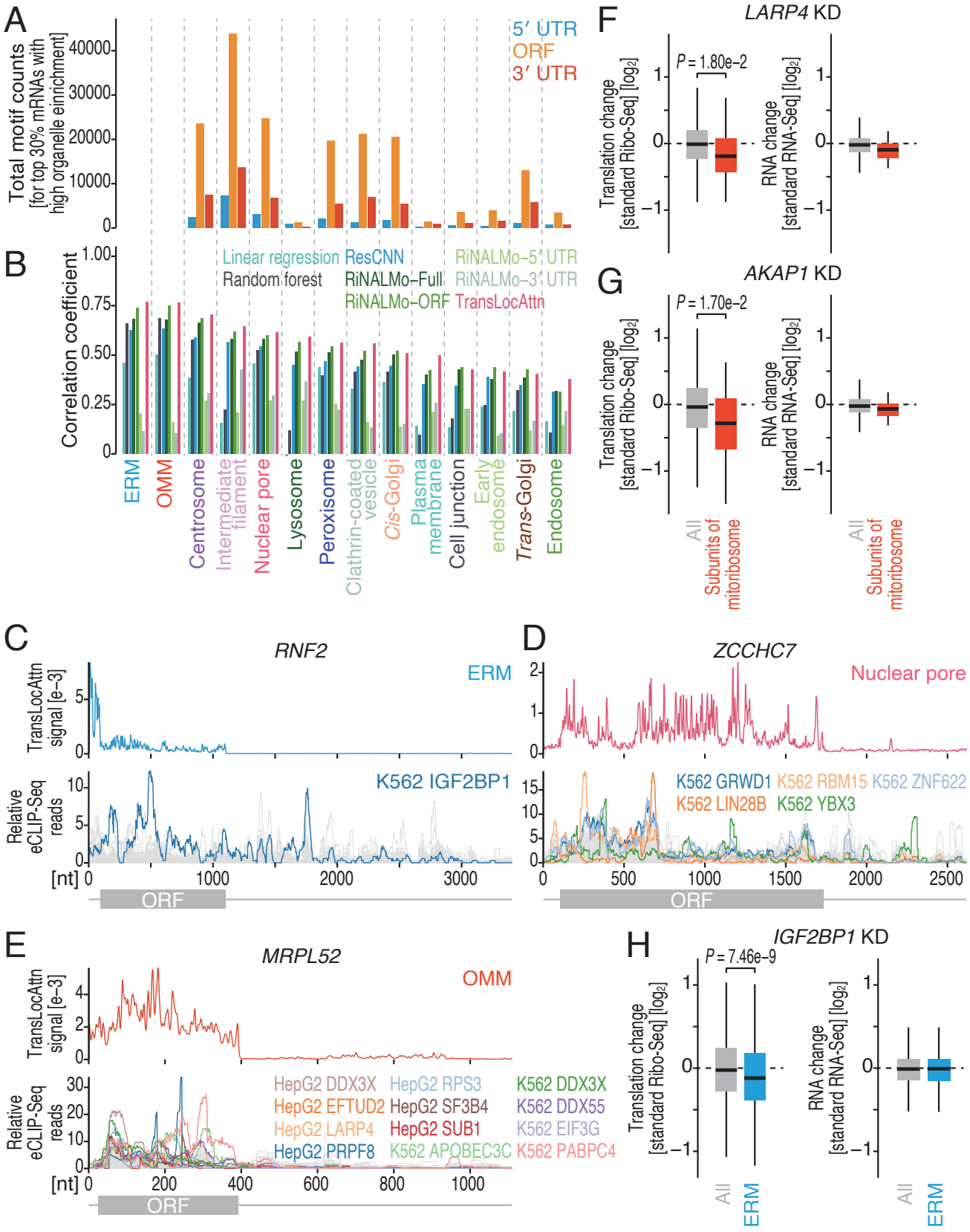

Figure 4 Tomuro *et al.* (2025)

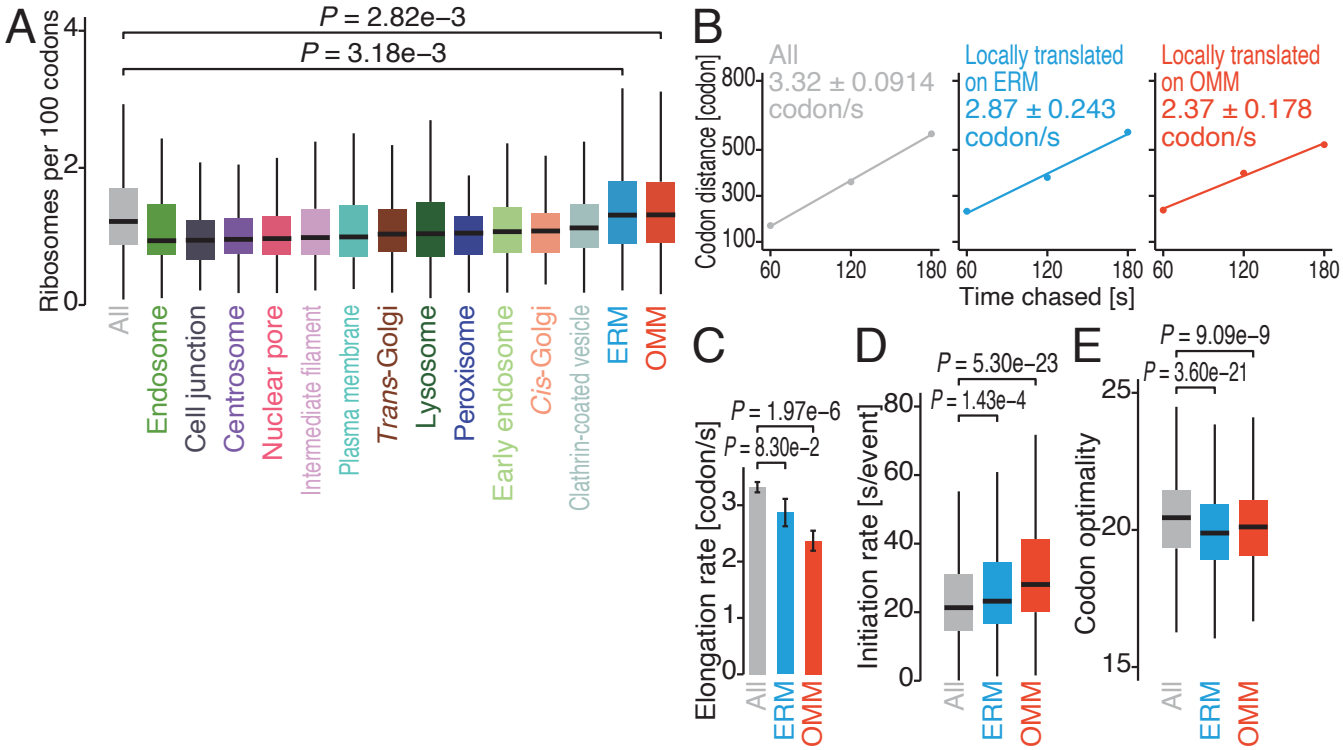

Figure 5 Tomuro *et al.* (2025)

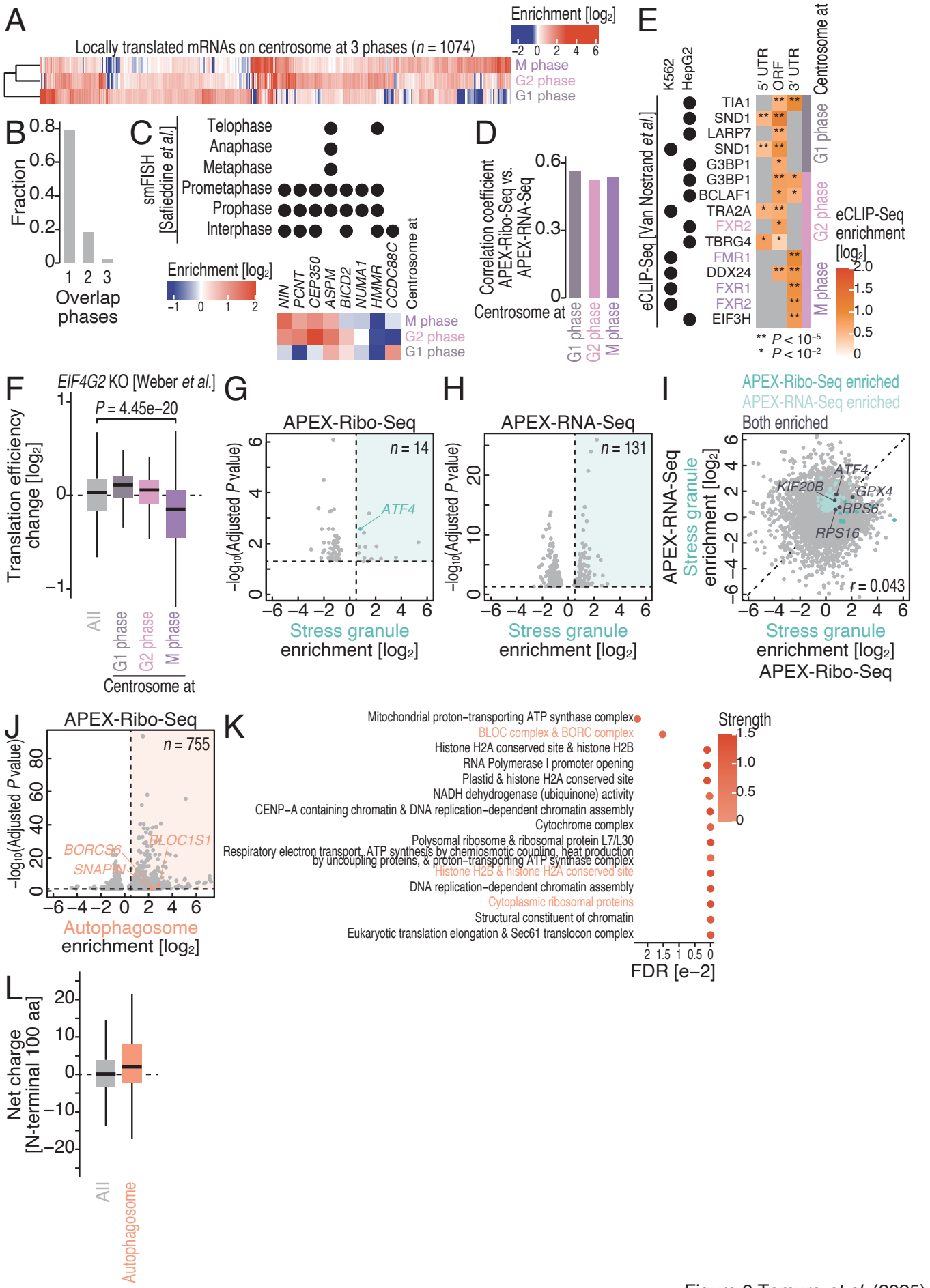

Figure 6 Tomuro *et al.* (2025)

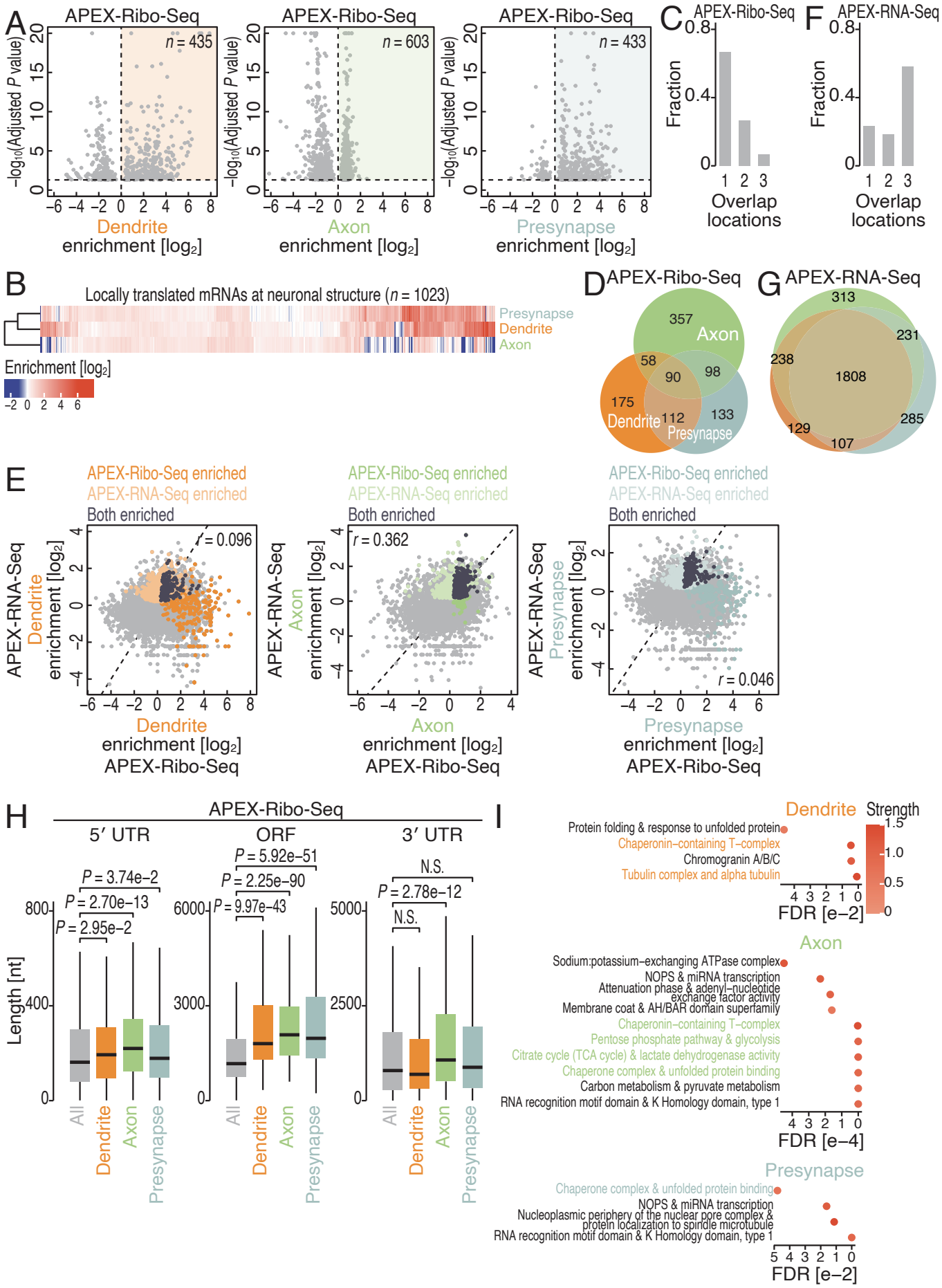

Figure 7 Tomuro *et al.* (2025)

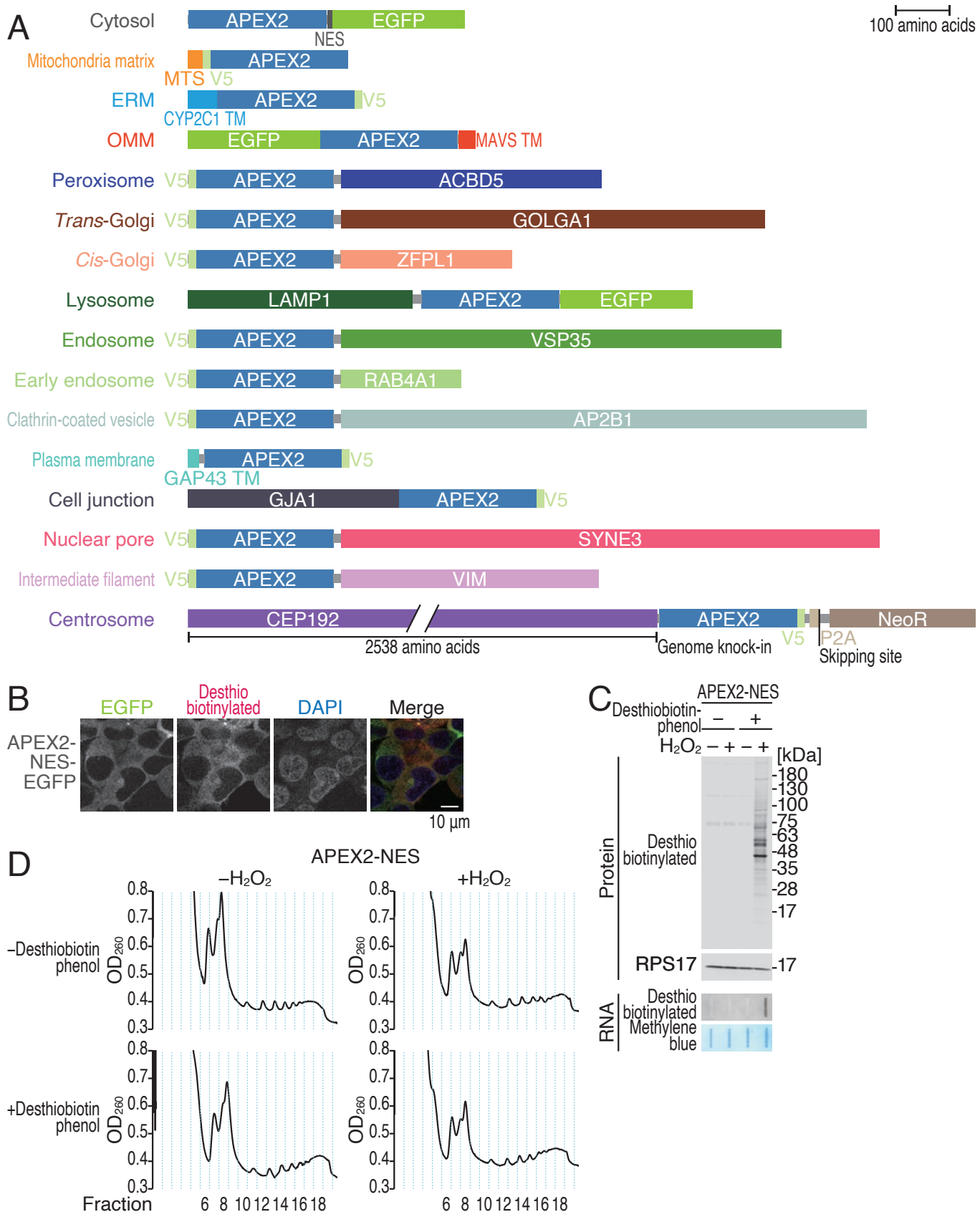

Figure S1 Tomuro *et al.* (2025)

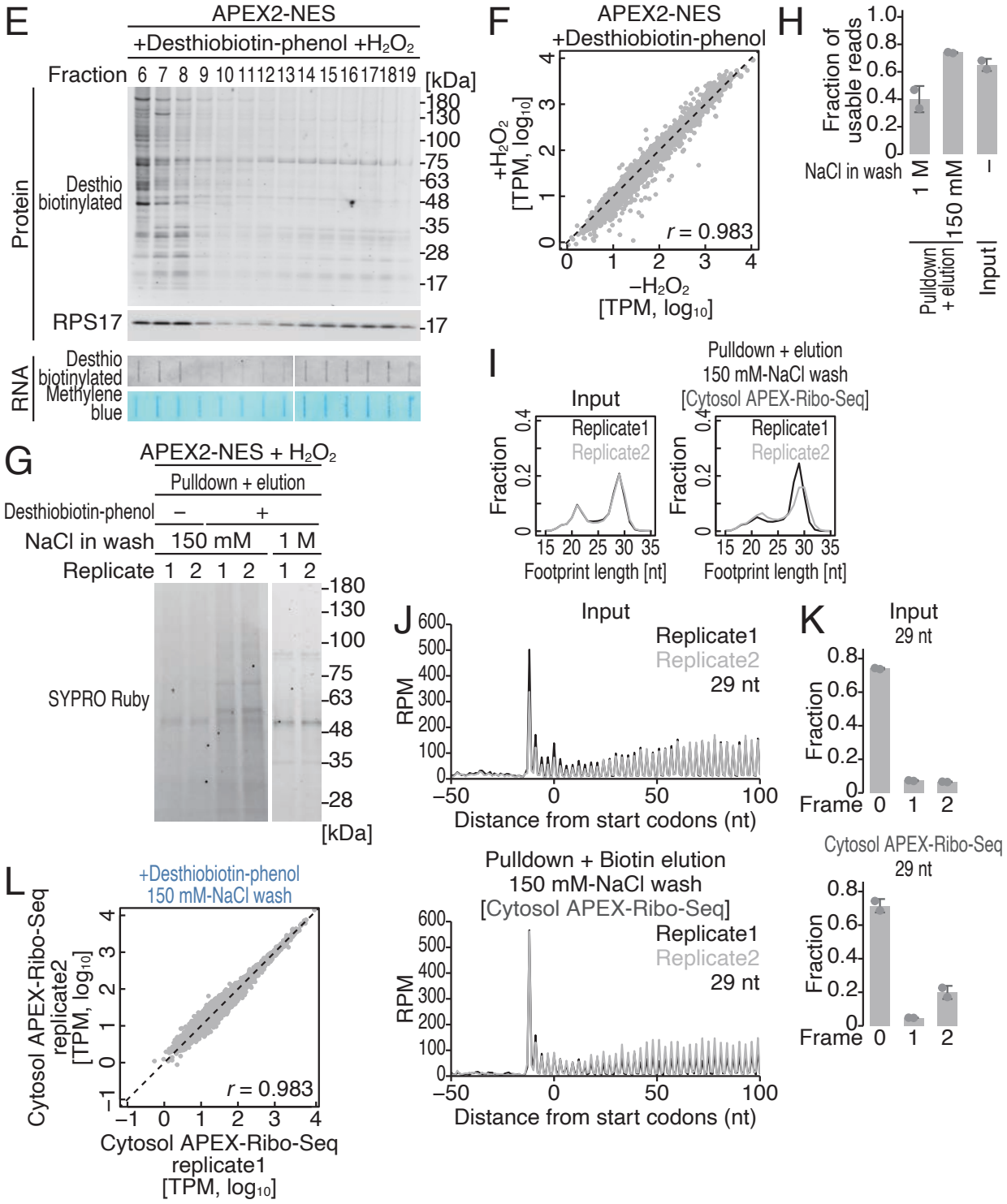

Figure S1 Tomuro *et al.* (2025)

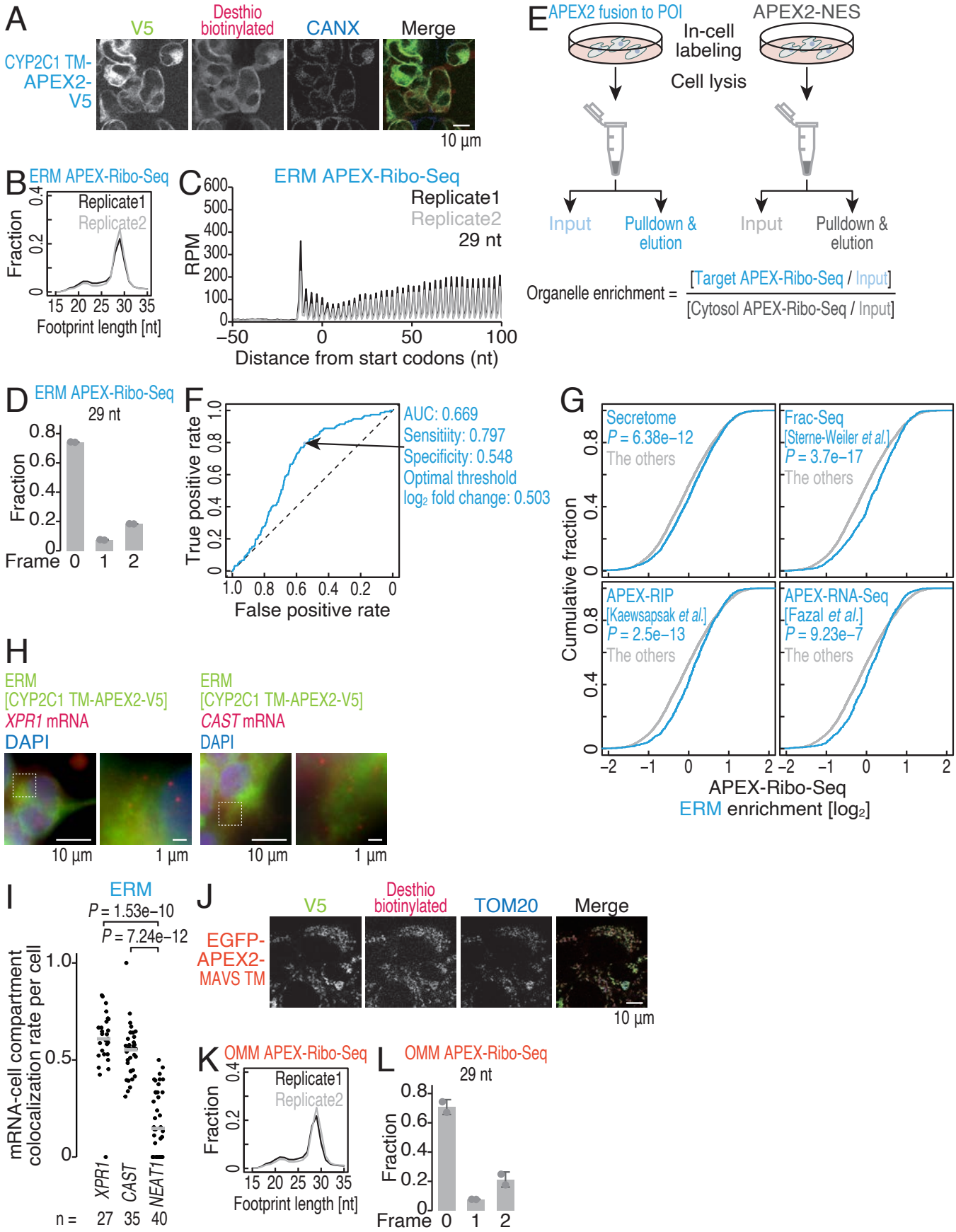

Figure S2 Tomuro *et al.* (2025)

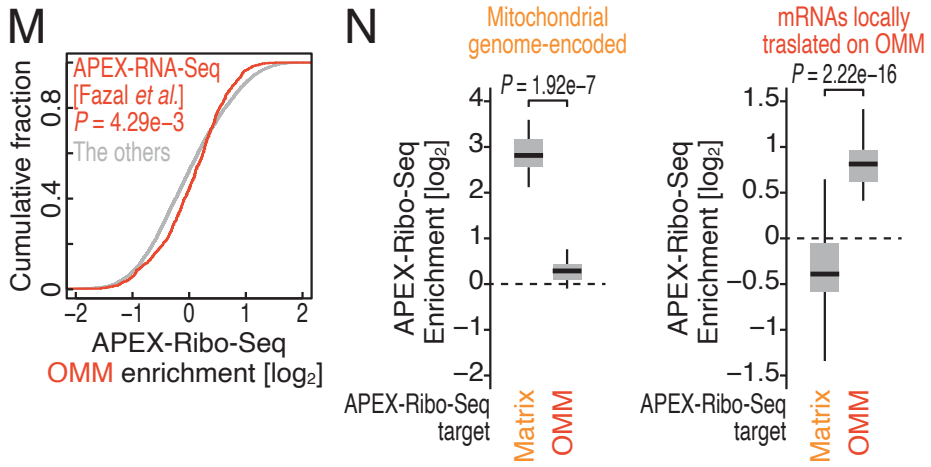

Figure S2 Tomuro *et al.* (2025)

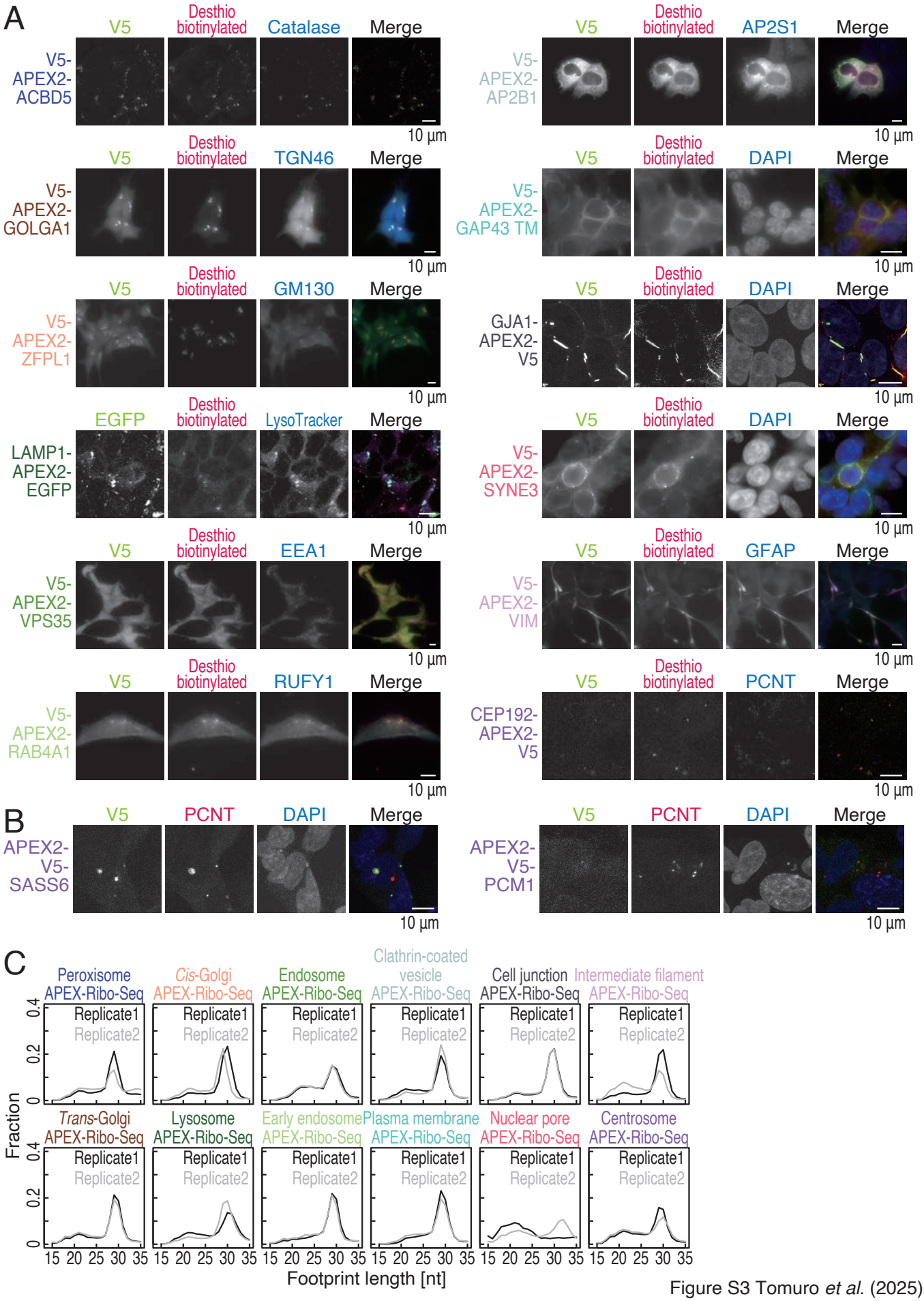

Figure S3 Tomuro *et al.* (2025)

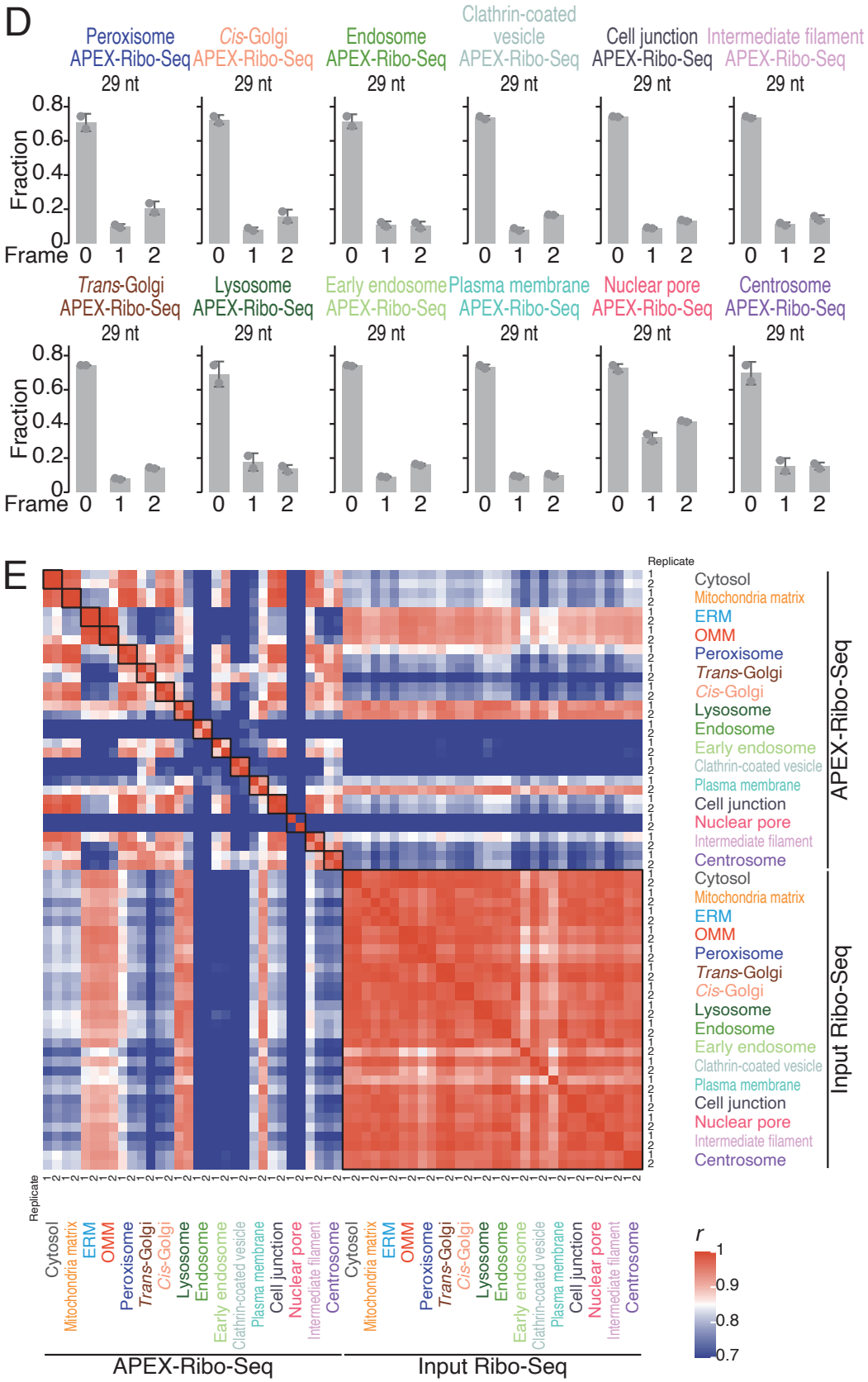

Figure S3 Tomuro *et al.* (2025)

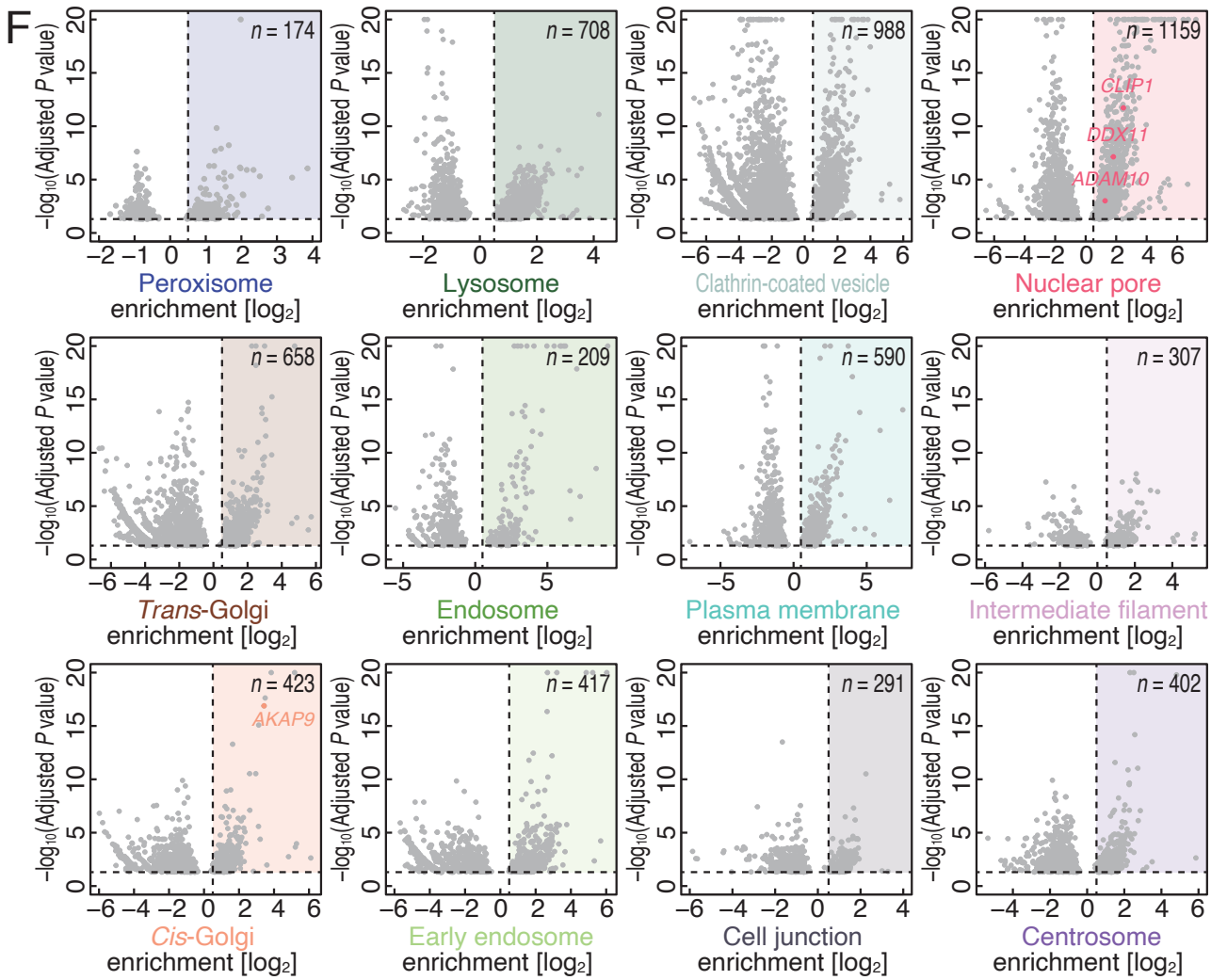

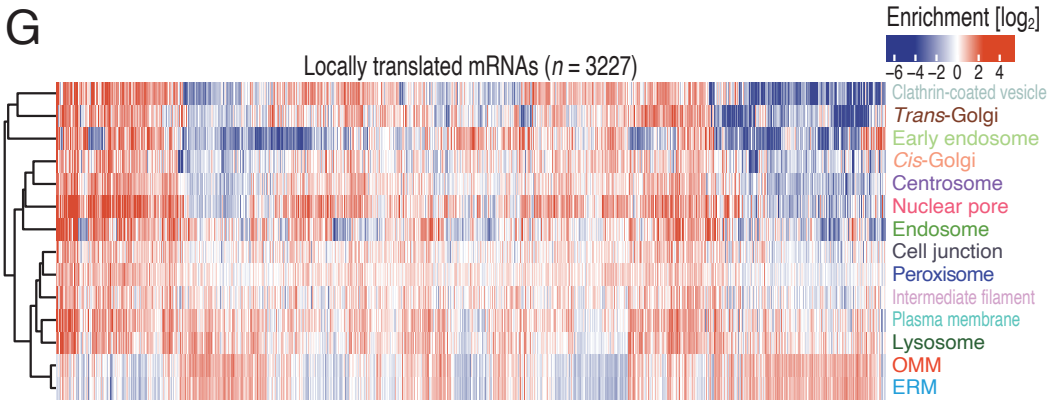

Figure S3 Tomuro *et al.* (2025)

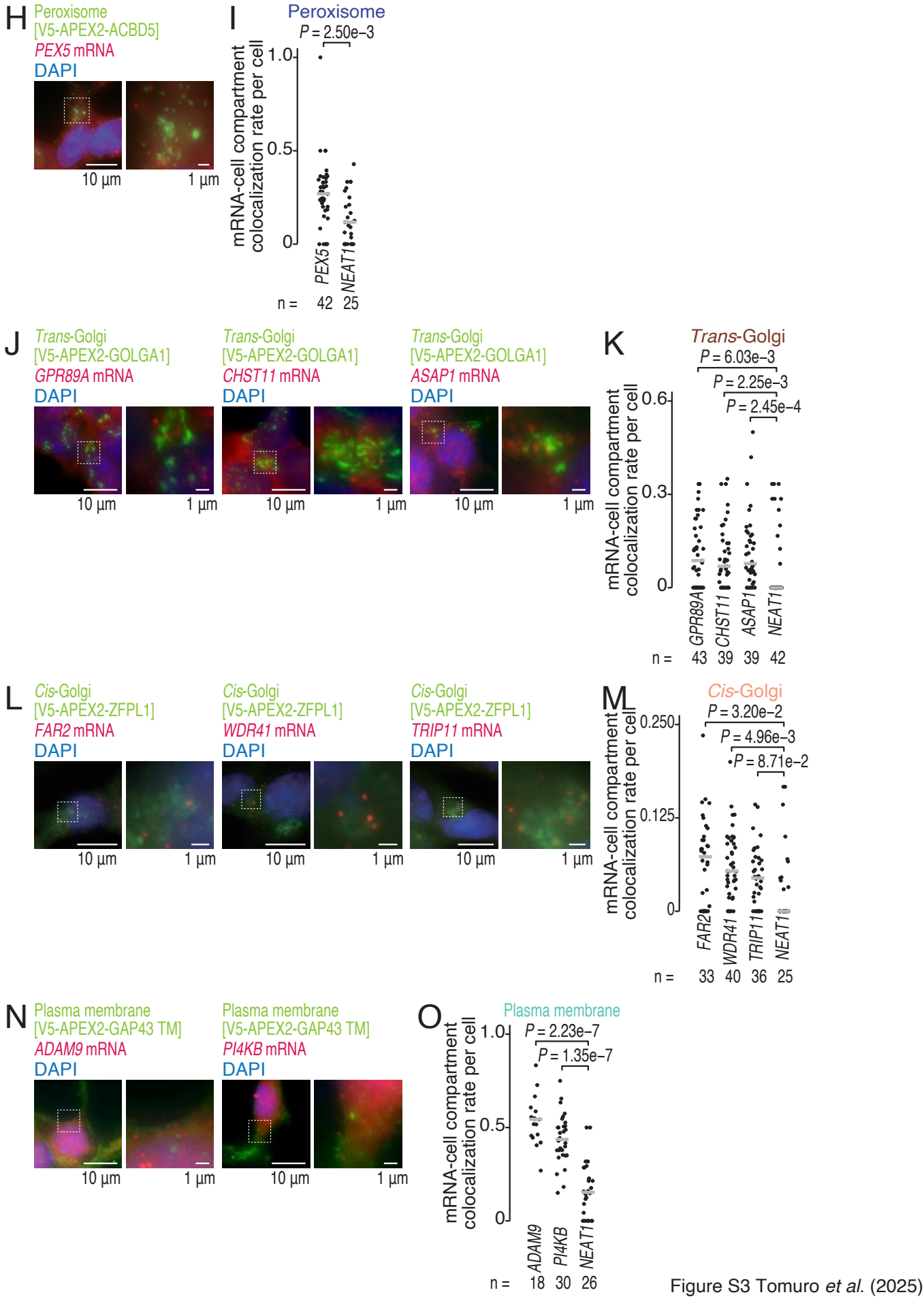

Figure S3 Tomuro *et al.* (2025)

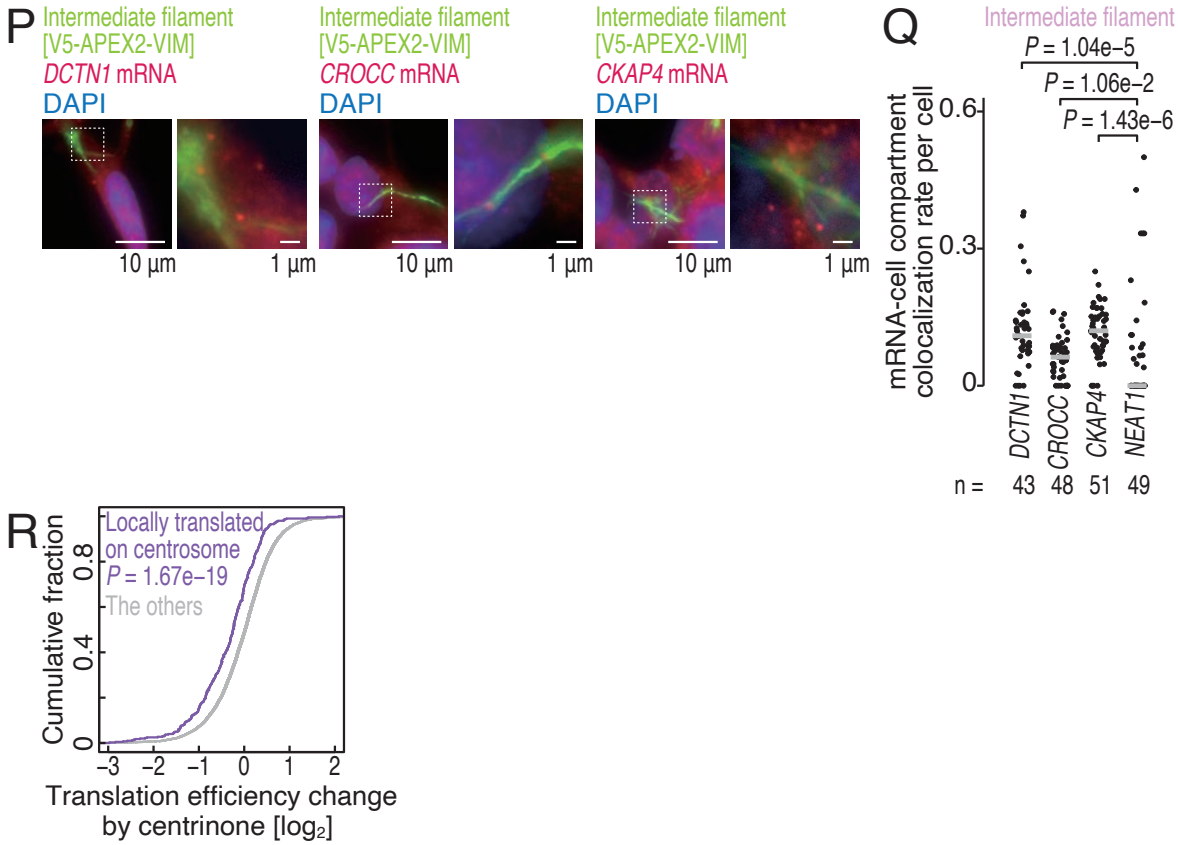

Figure S3 Tomuro *et al.* (2025)

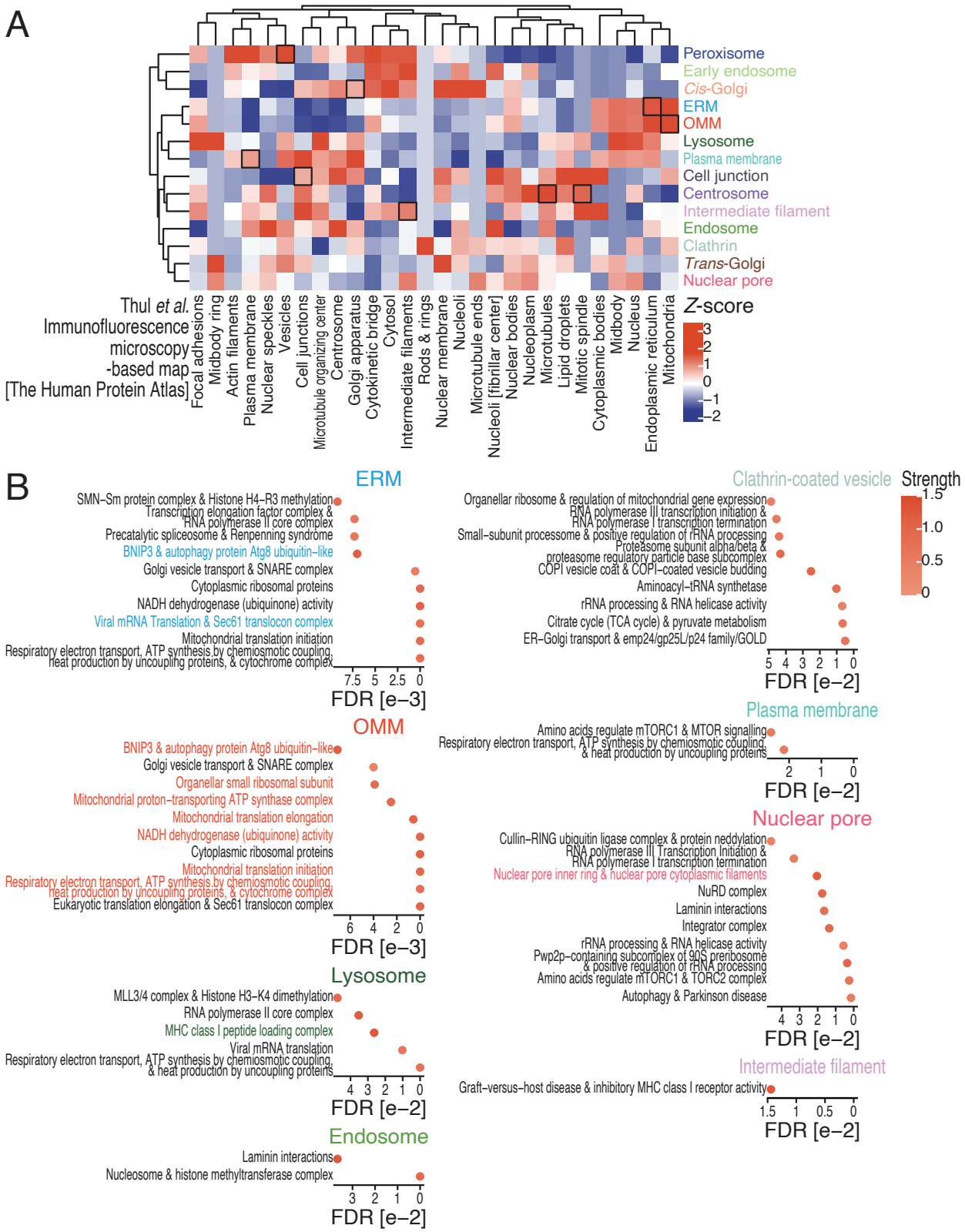

Figure S4 Tomuro *et al.* (2025)

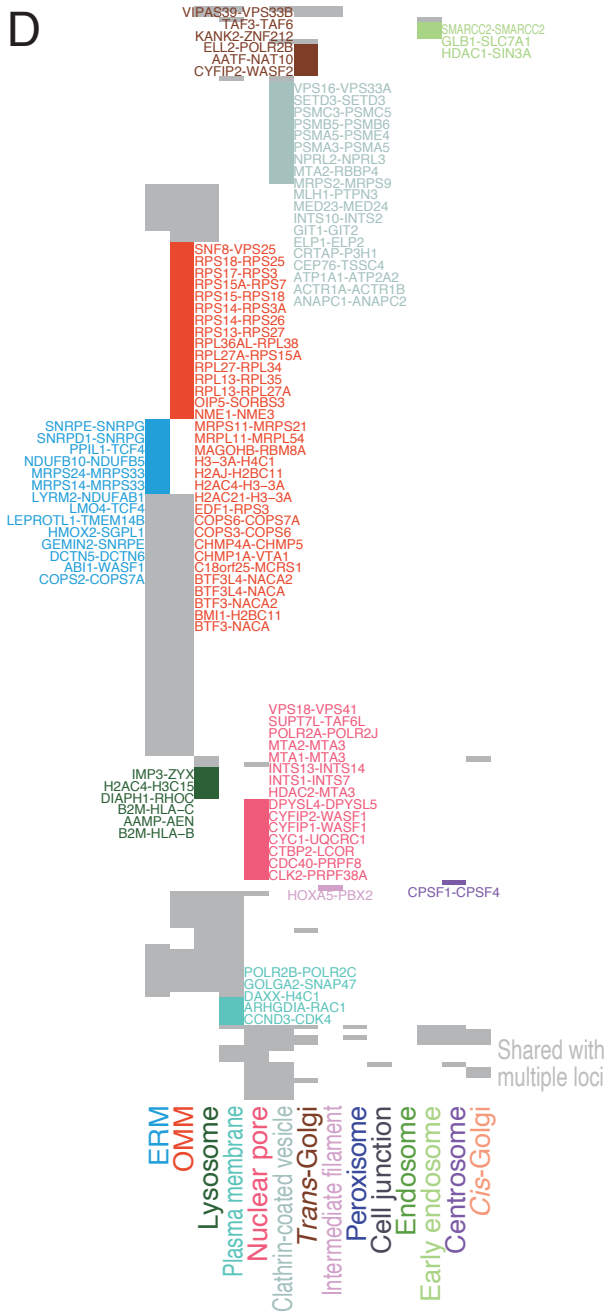

Figure S4 Tomuro *et al.* (2025)

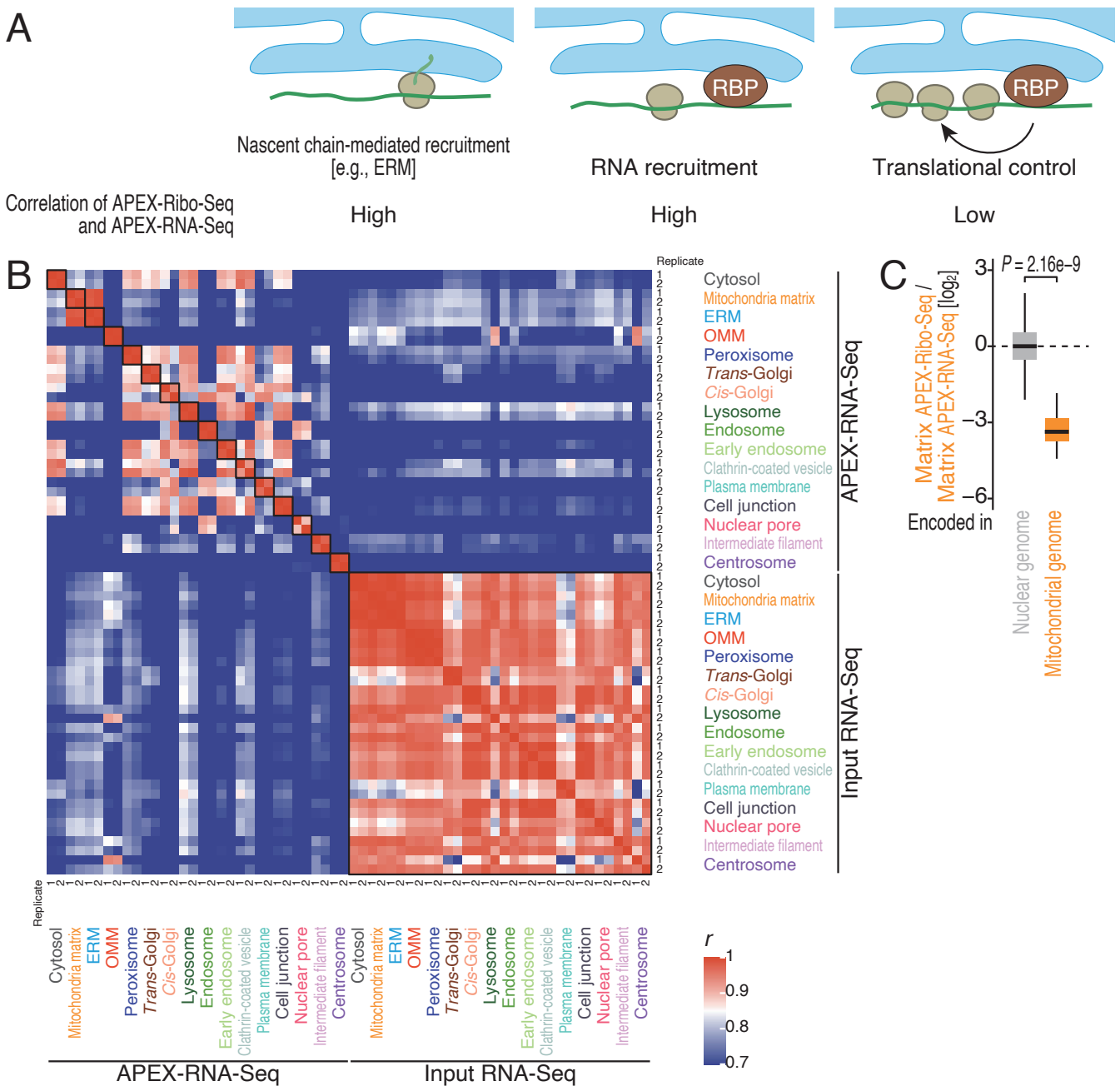

Figure S5 Tomuro *et al.* (2025)

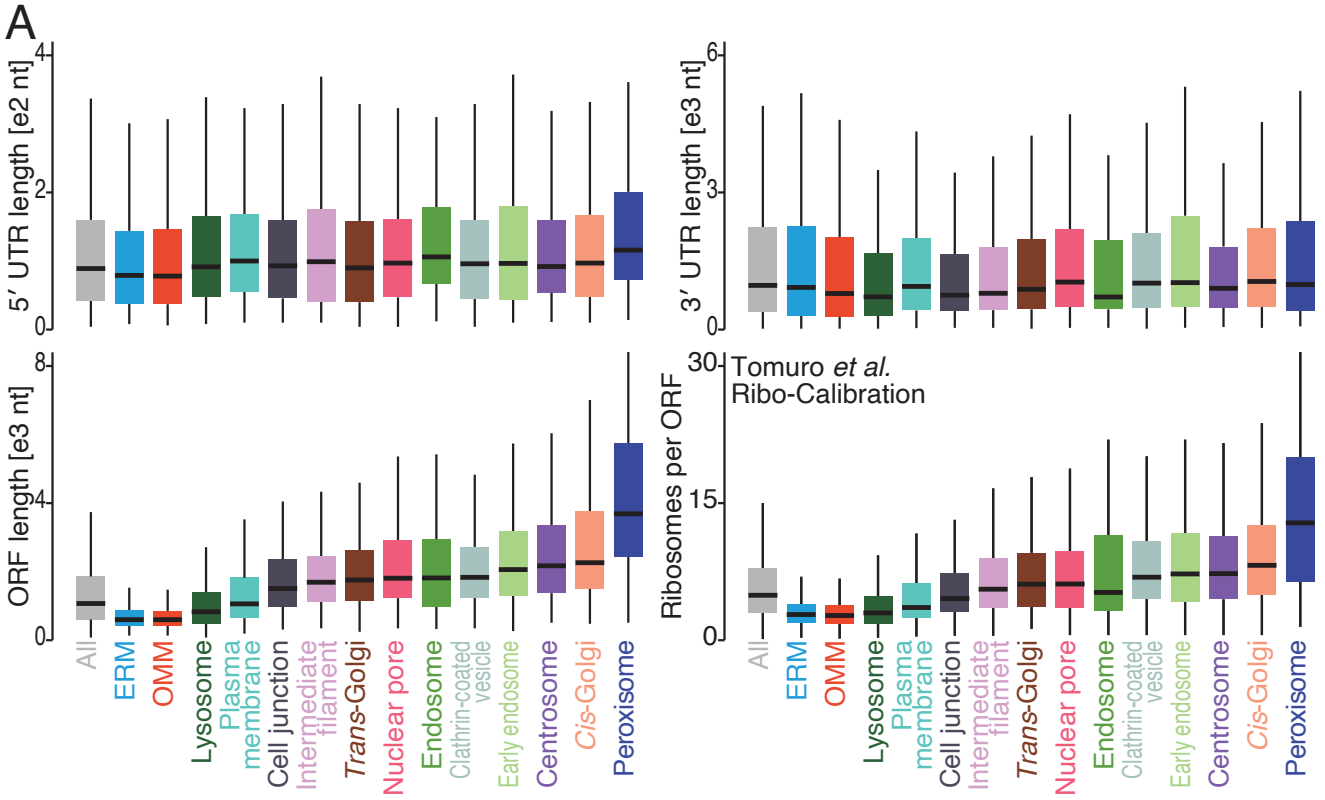

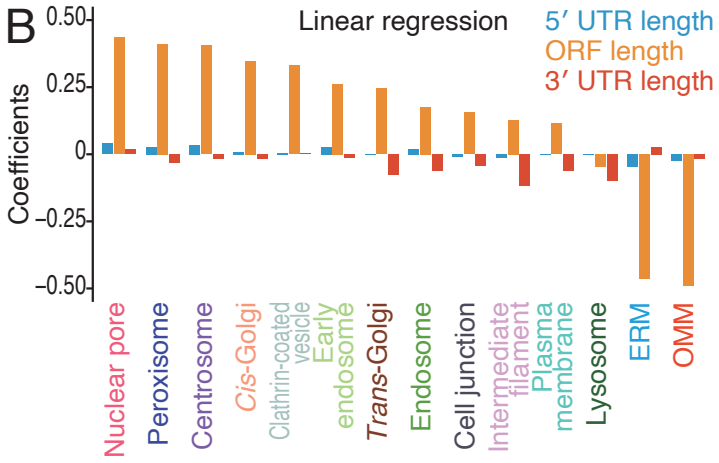

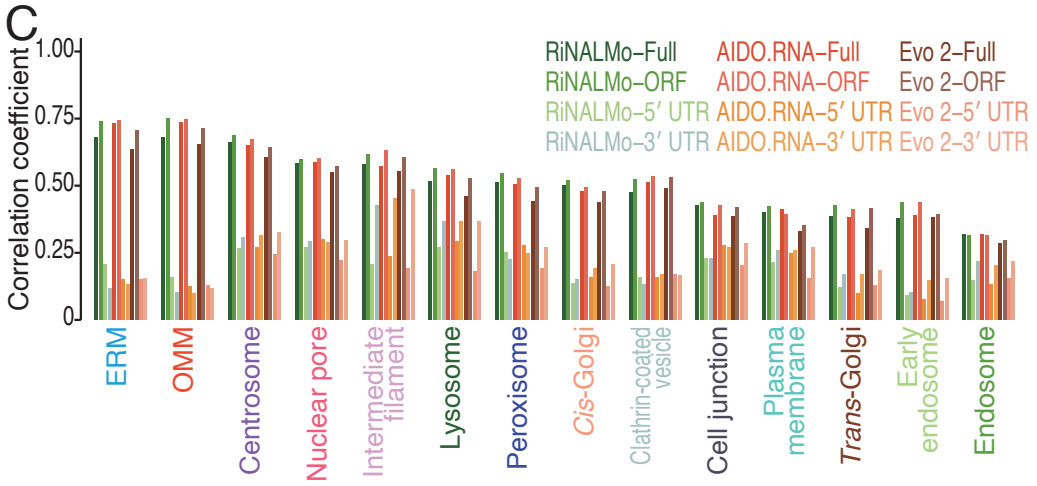

Figure S6 Tomuro *et al.* (2025)

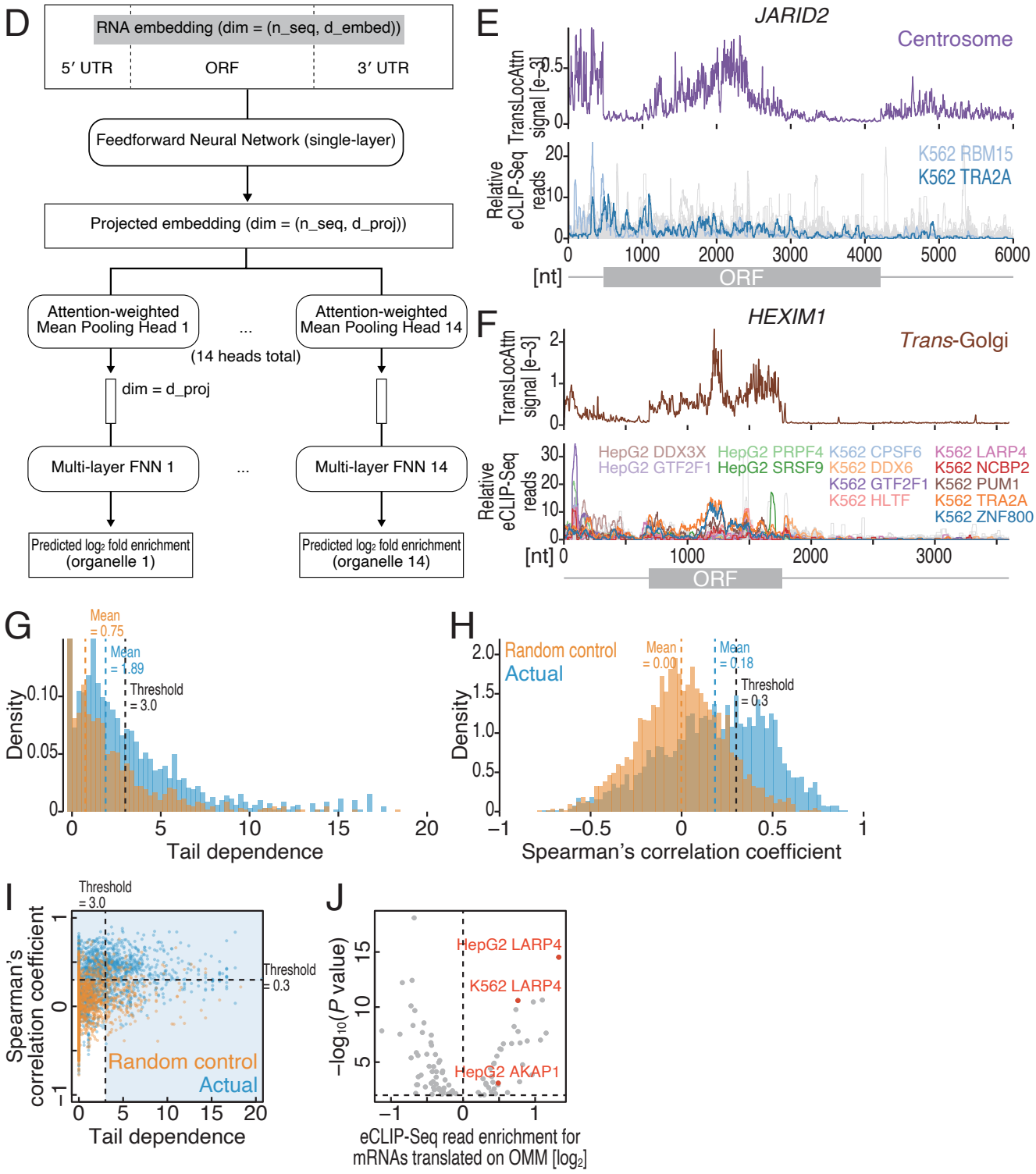

Figure S6 Tomuro *et al.* (2025)

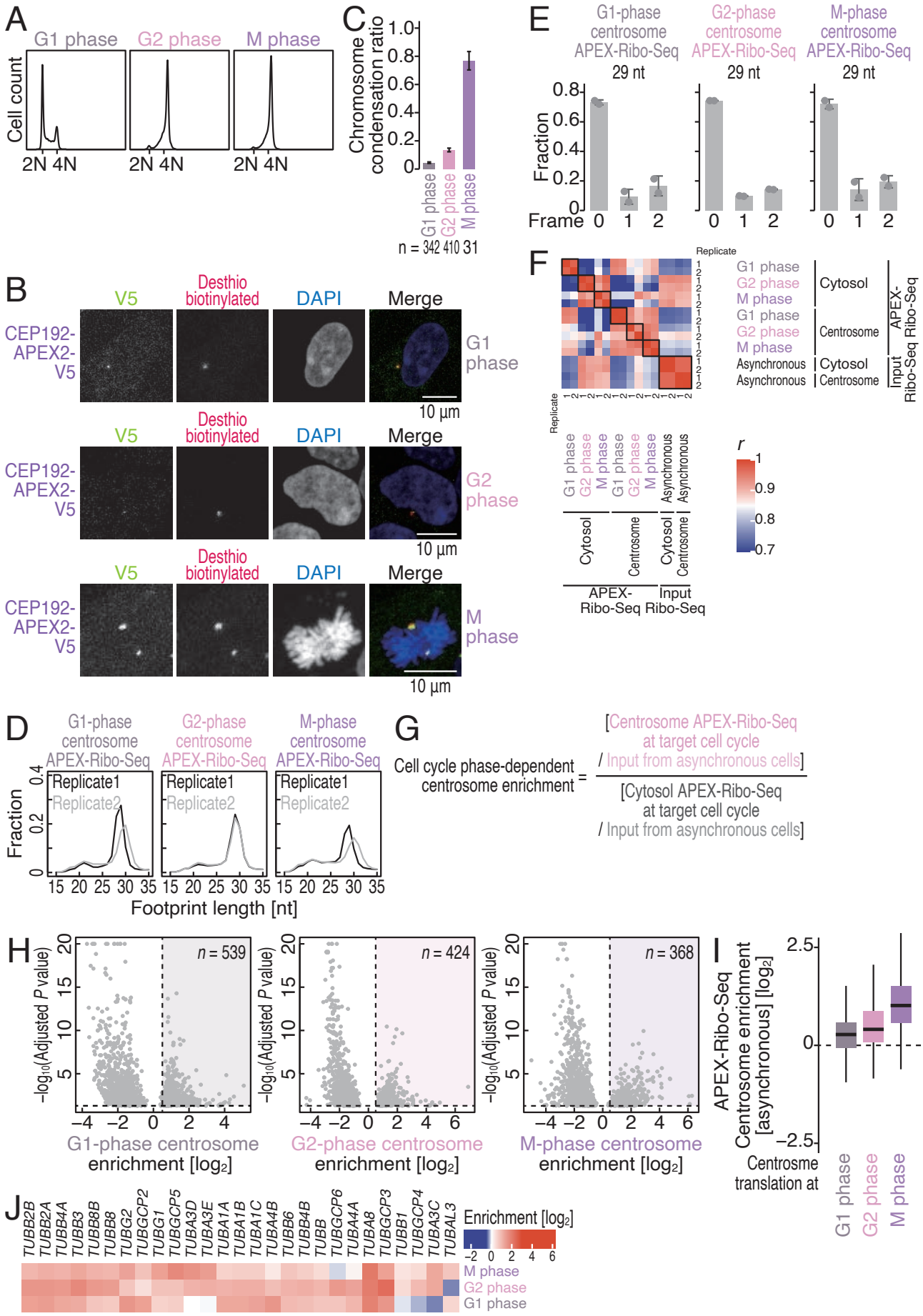

Figure S7 Tomuro *et al.* (2025)

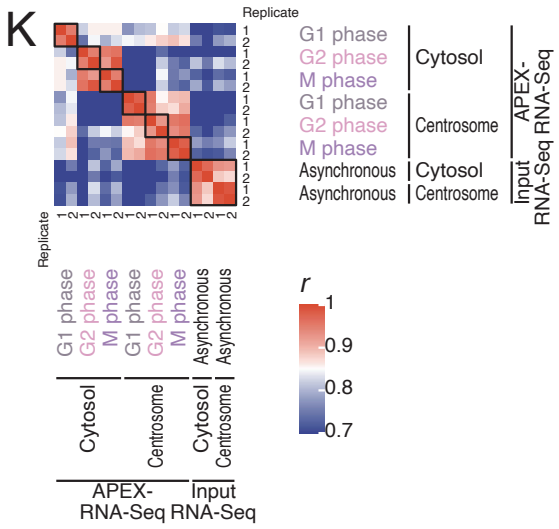

Figure S7 Tomuro *et al.* (2025)

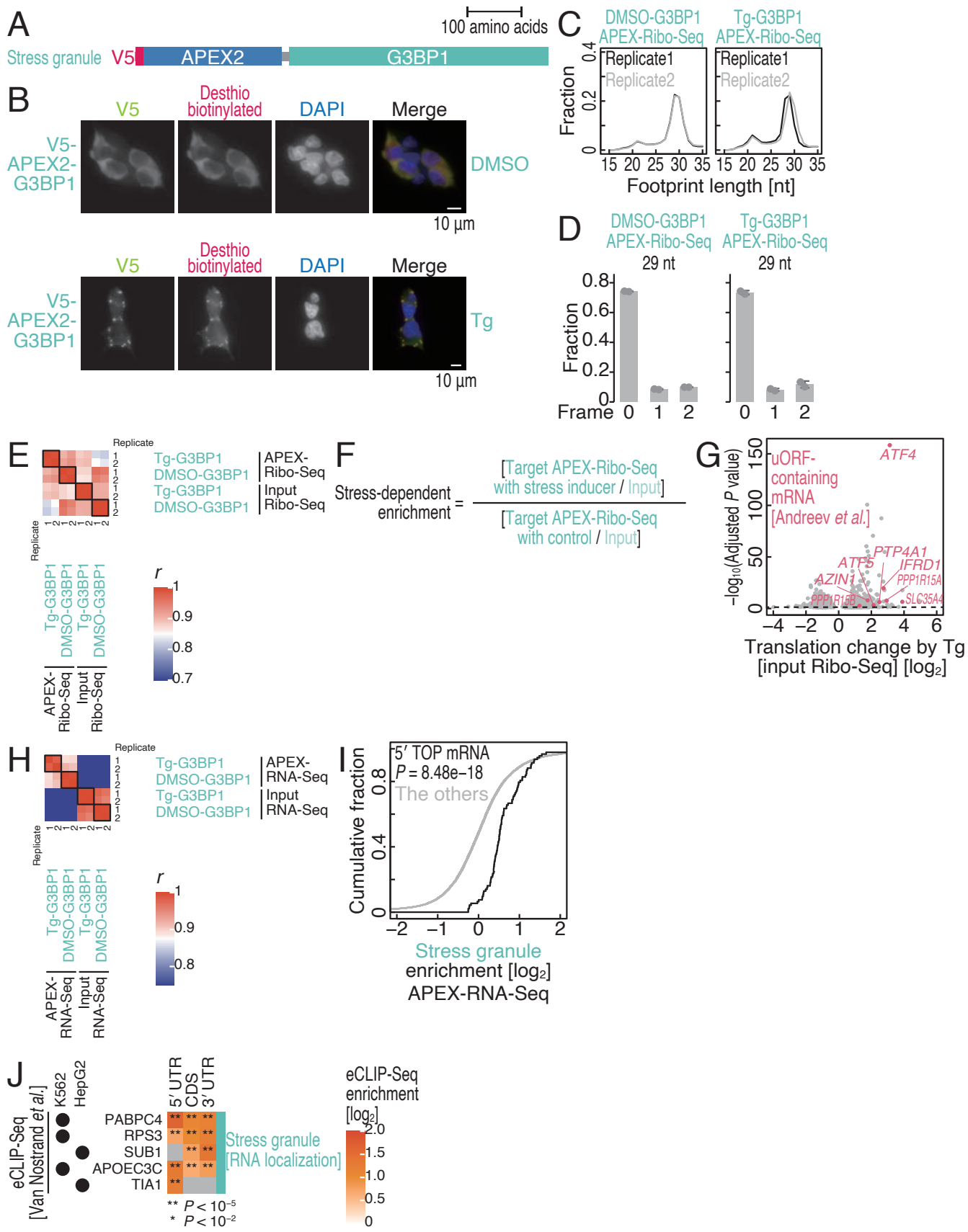

Figure S8 Tomuro *et al.* (2025)

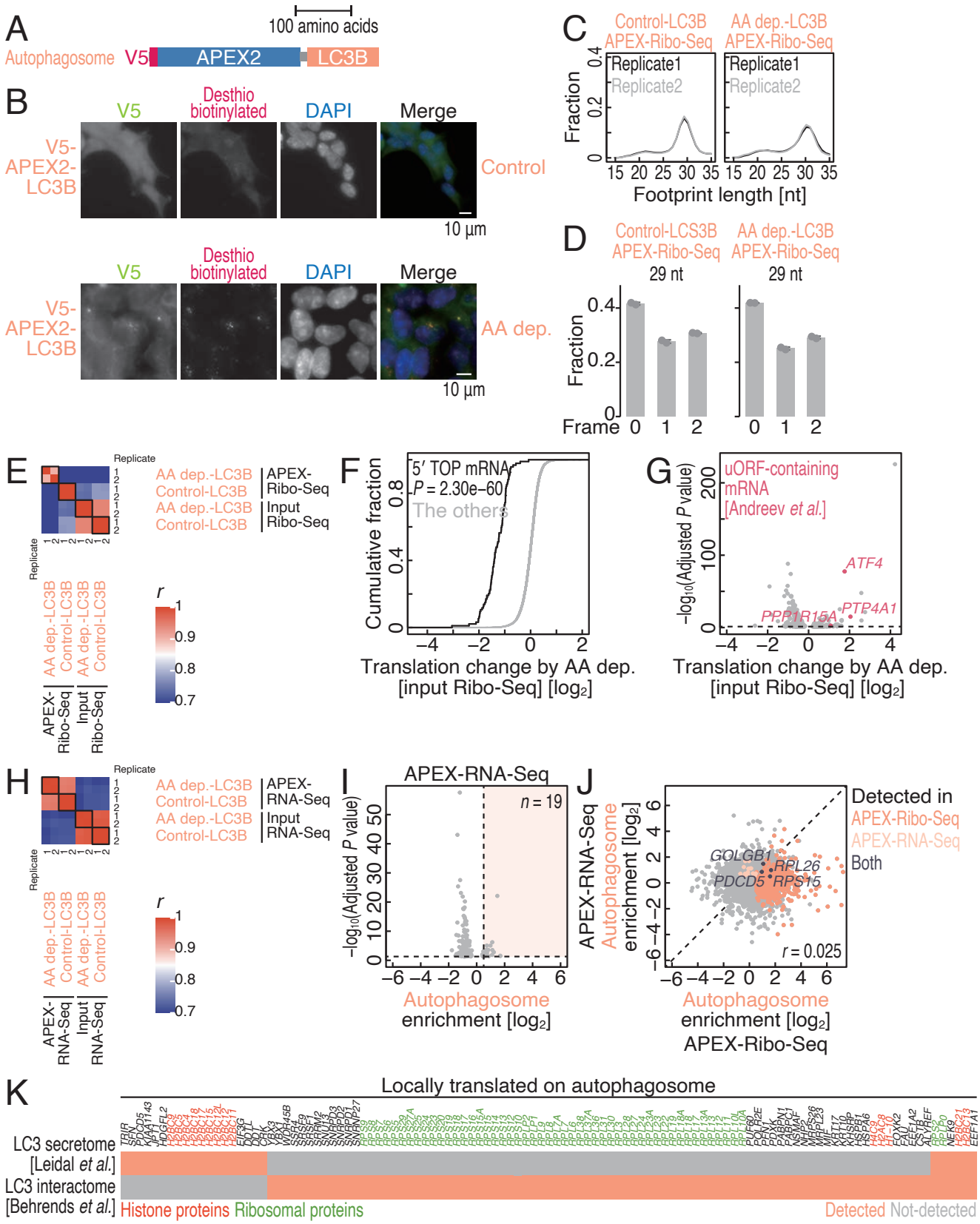

Figure S9 Tomuro *et al.* (2025)

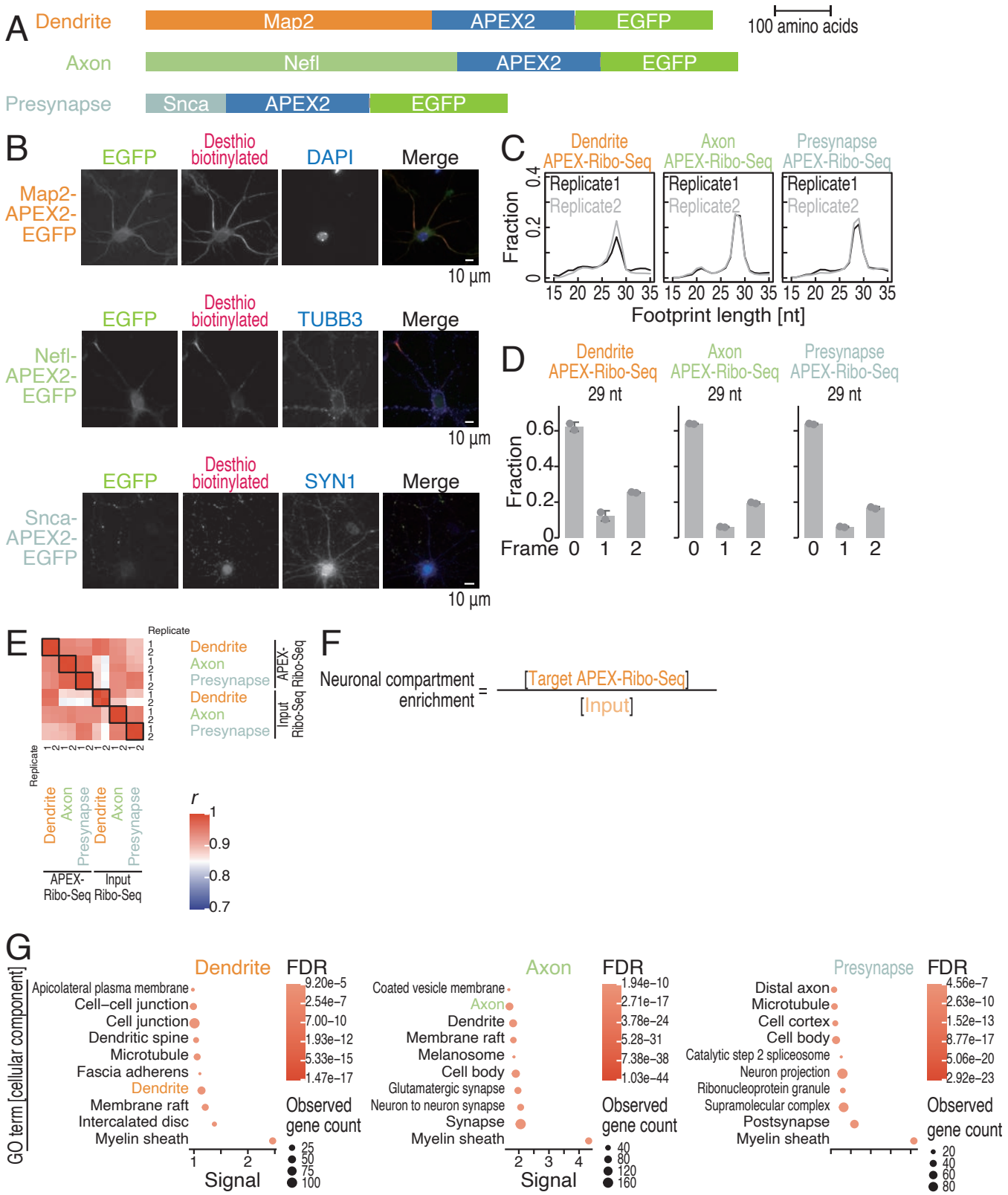

Figure S10 Tomuro *et al.* (2025)

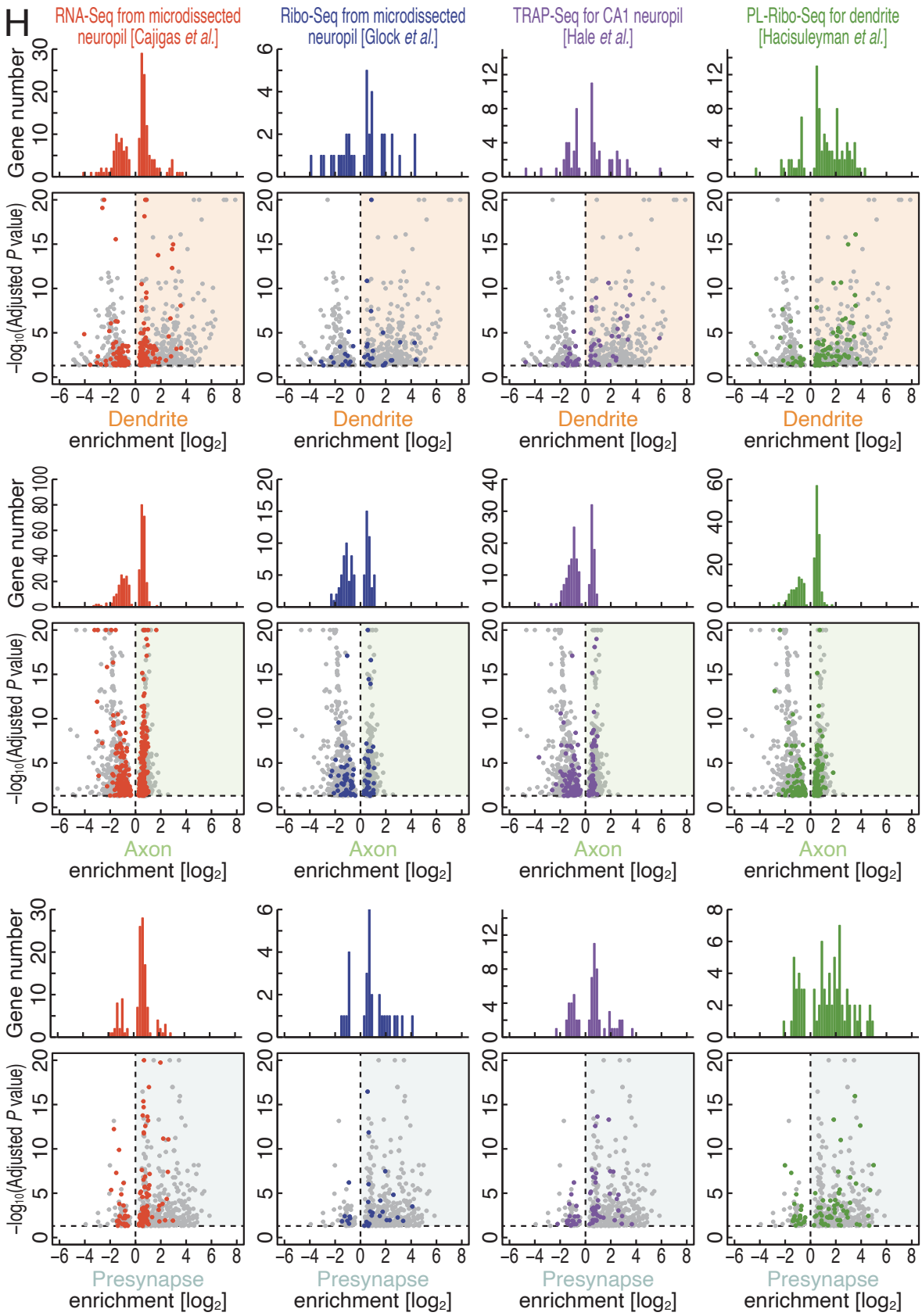

Figure S10 Tomuro *et al.* (2025)

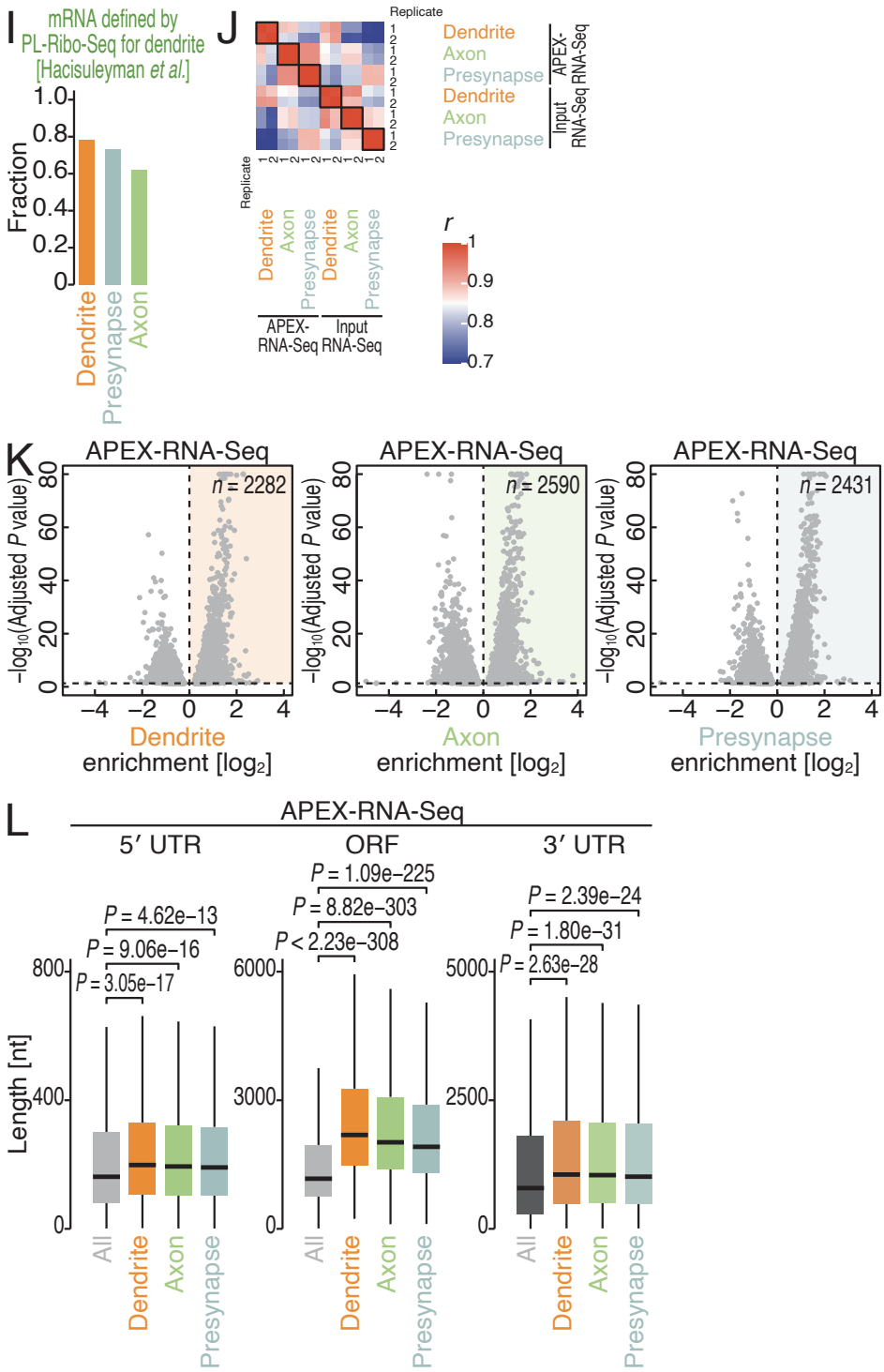

Figure S10 Tomuro *et al.* (2025)